kamUNikácie
COMMUNICATIONS

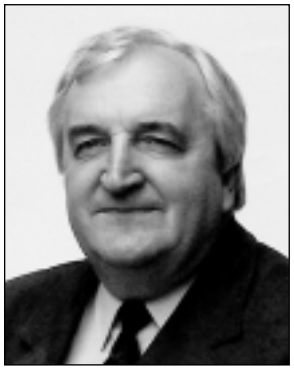

Úvodom

Efektívne navrhovanie ako aj posudzovanie aktuálnej únosnosti inžinierskych stavieb si vyžaduje aplikovať najnovšie poznatky o skutočnom pôsobení konštrukčných častí a materiálov. Najnovší vývoj v oblasti výpočtových modelov založených na metodike medzných stavov popisuje úvodná časť príspevkov.

Už druhé storočie používania betónu, ocele a dreva v stavebných konštrukciách sprevádza permanentný vývoj nových materiálov, ktoré sa stále viac presadzujú vďaka svojim prednostiam. Tieto priaznivé vlastnosti, ku ktorým patrí vyššia pevnosť pri redukovanej vlastnej tiaži a výhodnejších reologických efektoch sú témou ďalších príspevkov.

V súčasnosti sa okrem návrhu nových stavebných konštrukcií stále naliehavejšie prejavujú problémy spojené so spravovaním, údržbou a rekonštrukciou stavebných konštrukcií a mostov. Publikácie v tomto vydaní preto prezentujú tiež výsledky výskumu v tejto oblasti.

Oslovili sme známych odborníkov z naznačenej tematiky, aby vypracovali príspevky.

Výsledkom tejto výzvy sú recenzované publikácie, ktoré ponúkame čitateľom v tomto vydaní.

Foreword

The designing of civil engineering structures as well as assessment intervention demand to employ the latest knowledge of structural mechanics and material science. Recent advances in computer procedures based on limit-states philosophy as the results of research activities are presented in the first group of papers in this volume of journal.

As we enter the second century of the use of concrete, steel and wooden structures, new materials are becoming more widely understood, accepted and increasingly chosen on their own merits for constructions. An overview of developments on the advantageous properties of these materials, such as higher strength, low self-weight and rheological effects is the main subject of other papers.

Our tasks are not only to design and build new structures but also to consider the maintenance, repair and rehabilitation of the existing structures, both buildings and bridges. The journal papers present also the applications arising from the research results in this area.

Selected authors were invited to submit papers on the above topics. As a result of this call, a number of reviewed contributions are published in this volume.

Ján Bujňák

Maciej Yan Minch *

VÝPOČTOVÝ MODEL A ANALÝZA HRANIČNÝCH PRVKOV PRE ŽELEZOBETÓNOVÉ PANELY S TRHLINAMI

MODELING AND BEM ANALYSIS OF REINFORCED CONCRETE CRACKED PANELS

Príspevok uvádza postup stanovenia rozdelenia napätí v železobetónovom paneli s trhlinami. Väzko-elastický model železobetónovej dosky sa odvodil Gurtinovou variačnou metódou v priestore všeobecnej funkcie. Výsledné diferenciálne rovnice sú prezentované vo forme vektorových všeobecných funkcií. Diskontinuita všeobecného deformačného vektora, preklz po strate súdržnosti ako aj dotvarovanie betónu sú zohľadnené v popísanom výpočtovom modeli. Uvedené sú tiež numerické výsledky aproximatívneho riešenia použitím metódy hraničných prvkov.

In this paper the method of distribution solution of RC (reinforced concrete) cracked of the plane stress plates (panels) is shown. The viscoelastic RC cracked plate model has been derived by the variation method of Gurtin in the class of the general function. The total differential equations in the two-dimensional general vector functions are shown. In this model the effect of the discontinuity general deformation vector, bond slip and concrete creep are taken into account. The numerical results of approximate solutions with the method of boundary elements (BEM) are shown.

1. Introduction

The RC concrete plates are non-homogeneous. Therefore, the response of such heterogeneous structures and additional defects caused by cracks in concrete to applied actions is generally non-linear, due to nonlinear constitutive relationships of the materials, known as mechanical nonlinearity and to second order effects of normal forces, known as geometrical nonlinearity. Defects in form of cracks treated as continuous functions, which are usually based on the continuum mechanics approach, give unsatisfied solution because of summation of assumption errors and solution errors. Therefore, the proper mathematical modeling of panels is so important since the final error appears solely in a solution phase.

This paper contains a mathematical model of reinforced concrete panels formulated in terms of general functions. The physical hypothesis about the discontinuous change of the displacement vector, caused by the cracking of the extension zone in the concrete, with the assumption of rotating cracks, is included in the model. The assumptions of the distribution theory of Schwartz [1] afford possibilities for precise mathematical description of the crack discontinuity of the panels.

2. Differential equation for displacement

The arbitrary plane stress plate is considered. The plate has arbitrary homogeneous boundary conditions and is arbitrarily forced. The region of plate Ω is divided by the curve Λ which means the crack, in two zones Ω_1 and Ω_2 with bound $\partial\Omega_1$ and $\partial\Omega_2$. The curve Λ has two ends Λ_1 and Λ_2. The normal external direction cosines of the edge Λ of regions Ω_1 and Ω_2 have different signs. The considered model can be easily generalized to any number of cracks Λ. [M1]

The discontinuous variation problem of the surface integral for the displacement of the viscoelastic plane stress plate Ω was solved.

The equilibrium equations in the form: $div\ \boldsymbol{S} + \boldsymbol{b} = \mathbf{0}$ (where **b** – body forces), and geometrical relations in the form:

$E = \frac{1}{2}(\nabla u + \nabla u^T) = \widetilde{\nabla} u$ are taken.

The set of the field equations is fulfilled in the space $\Omega x < 0, \infty)$, where $< 0, \infty)$ is the time interval. The initial condition of the strain' tensor has to be added $\boldsymbol{E}(\ .\ , 0) = \boldsymbol{E}^0$, for $t = 0$.

The physical law is taken as well-known Boltzmann's rule.

The constitutive law of defect is assumed to be represented as follows:

$$[\boldsymbol{u}(\boldsymbol{x})]_{\Lambda_1\Lambda_2} = \boldsymbol{r}(\boldsymbol{x}), \text{ with conditions}$$
$$\frac{\partial r}{\partial s}(\Lambda_1) = \frac{\partial r}{\partial s}(\Lambda_2) = 0, \qquad (1)$$

where $[\ .\ ]\Lambda$ means the difference of the left and right side limit of the expression in square braces on the curve Λ.

* **Dr. Ing. Maciej Yan Minch**
Faculty of Civil Engineering, Wrocław University of Technology
Wybrzeże Wyspiańskiego 27, 50-370 Wrocław, Poland, E-mail: minch@pionier.ib.pwr.wroc.pl

Here $\boldsymbol{r}(\boldsymbol{x})$ describes the density of the defect as a continuous function for $x \in \Lambda_1\Lambda_2$ and $[\boldsymbol{u}]_\Lambda = 0$ for $x \notin \Lambda_1\Lambda_2$. To satisfy the first condition of Eq. (1), the modeling on the crack edges by the dipole normal forces for the plate is assumed.

Equation (1) satisfies the compatibility condition in the crack, where the displacement vector has a jump on a bound of crack. Here the assumption of internal crack $\Lambda_1\Lambda_2$ was taken, which can be easily demonstrated. Hence, on the remaining part of the curve Λ the condition $[\boldsymbol{u}]_\Lambda = 0$ is valid, for $x \notin \Lambda_1\Lambda_2$. Moreover, the second condition (1), in the essential way, completes the definition of the defect. Note that the constitutive law of the crack opening is expanded as a rule additionally valid in time.

The assumption of the jump of displacement vector $\boldsymbol{u}(\boldsymbol{x})$ was demonstrated in an experimental study, see [2]. The zone of plate Ω_1 is connected with another one Ω_2 by means of reinforcement bars appearing in the cracks. Hence, the edges of the cracks are not free from tensions at the points of connections. Outside the reinforcement points, on the remaining edge segments of the cracks, the boundary conditions should be equal to the conditions corresponding to the free edges. The density of defect, also known as the constitutive law of crack opening, is the function of tension vector $\boldsymbol{N}$ acting in the crack:

$$\boldsymbol{r}(\boldsymbol{x}) = \boldsymbol{r}^0(\boldsymbol{x}) - \boldsymbol{r}^1(\boldsymbol{x})\Im(\boldsymbol{N}(\boldsymbol{x}))\big|_\Lambda, \boldsymbol{x} \in \Lambda_1\Lambda_2 \tag{2}$$

Here $\boldsymbol{r}^0$ describes residual general deformations, whereas $\boldsymbol{r}^1\Im(\boldsymbol{N})$ describes the elastic general deformations. The components $\boldsymbol{r}$ of Eq. (2) are given from RC element tests, from general assumptions of crack theory, and equilibrium conditions in the crack.

The discontinuous viscoelastic variation problem of the Gurtin type was solved. The equilibrium equations, Boltzmann constitutive law, strain equations and the initial condition are assumed to be represented by the well-known theory of elasticity relations. We are looking for the extreme of the functional of strain energy with a set of permissible displacement value $\boldsymbol{u}(\boldsymbol{x})$.

The searching function $\boldsymbol{u}(\boldsymbol{x})$ is in the class of the function $\boldsymbol{u} \in C^2(\Omega/\Lambda)$ (for $\boldsymbol{x} \in \Lambda$ function $\boldsymbol{u}(\boldsymbol{x})$ has singularity).

Applying Green's transformation with material relations, field relations and the constitutive law of cracks taken from Eq. (1), additionally using a functional description with δ of Dirac's type, the resulting general differential equation of viscoelastic RC cracked plate in plane stress, appropriate boundary, compatibility and initial conditions, respectively, can be written as follows:

$$[\psi 1 * \nabla^2 + \frac{1}{2}(\psi_1 + \psi_2) * \mathit{grand\ div}]\boldsymbol{u}(\boldsymbol{x},t) + 1 *$$

$$* \boldsymbol{b}(\boldsymbol{x},t) - \mathit{div}\,\boldsymbol{F} = -\widetilde{N}(\boldsymbol{r}(\boldsymbol{x},t)\delta_\Lambda) + [1 * \widetilde{\boldsymbol{p}}(\boldsymbol{x},t) -$$

$$- \widetilde{N}(\boldsymbol{u}(\boldsymbol{x},t))]\delta_{\partial\Omega_1} + \widetilde{N}[(\widetilde{\boldsymbol{u}}(\boldsymbol{x},t) - \boldsymbol{u}(\boldsymbol{x},t))]\delta_{\partial\Omega_2}, \tag{3}$$

where:

$$\boldsymbol{F} = \psi_1 * \boldsymbol{E}^0 + \frac{1}{2}(\psi_2 - \psi_1) * \boldsymbol{1}\ tr\,\boldsymbol{E}^0. \tag{4}$$

The viscoelastic operator $\widetilde{N}$ corresponds to the analogy of surface tension from the theory of elasticity as follows:

$$\widetilde{N}(.) = -[\boldsymbol{F} - (\psi_1 \widetilde{\nabla} + \frac{1}{2}(\psi_2 - \psi_1) * \mathit{div})(.)]\boldsymbol{n}. \tag{5}$$

Here the functions ψ_1 and ψ_2 are the functions of relaxation, $\boldsymbol{n}$ represents the normal vector external to the edge $\partial\Omega$ and $f(t)$ * * $g(t)$ means the convolution rule.

Note that the final solution (3) is similar to the elastic solution achieved by Minch, see [3], where the difference occurs only for the relaxation function, with λ and μ as a time dependent function.

The solution of Eq. (3) is possible with the help of the elastic solution as a first approximation of the viscoelastic solution. It denotes the solution of the "associated" elastic problem $\boldsymbol{u}(\boldsymbol{x},t)$ from the elastic solution. This method can be used for solving the convolutions' of the viscoelastic static problem of the RC cracked plane stress as follows:

$$\boldsymbol{u}(\boldsymbol{x},t) = \int_0^t \partial\frac{\boldsymbol{u}(\boldsymbol{x},\tau)}{\partial\tau}\,\varphi(t-\tau)d\tau, \tag{6}$$

where φ is the function with the combination of relaxation and creep functions.

3. Modeling by Boundary Element Method

Deformation behaviour depends on the history of the loading as well as the non-linearity of the material properties. Hence, the equations and definitions of the boundary element method in the rate form were assumed. According to the small strain theory, the total strain rate for an inelastic problem can be divided into an elastic and inelastic part of the total strain rate tensor. Herein, the inelastic strain means any kinds of strain field that can be considered as initial strain, i.e. plastic or viscoplastic strain rate, creep strain rate, thermal strain rate and strain rate due to other causes. So, now we can write the equations of the considered problem in terms of non-linear BEM formulations for fictitious traction vector $\boldsymbol{p}$ and body forces' $\boldsymbol{b}$, finally leading to the initial stresses σ^p:

$$\boldsymbol{H}\dot{\boldsymbol{u}} = -\boldsymbol{A}\dot{\boldsymbol{p}} + \boldsymbol{B}\dot{\sigma}^p + \boldsymbol{F}\dot{\boldsymbol{x}} + \boldsymbol{Q}(\dot{\boldsymbol{x}}), \tag{7}$$

where $\boldsymbol{u}$ means displacement vector, $\boldsymbol{x}$ is the vector of unknown edge traction, $\boldsymbol{p}$ means the vector of fictitious traction, while $\sigma^{\mathbf{p}}$ is the vector of initial stresses. Here the matrices $\boldsymbol{H}$ and $\boldsymbol{A}$ are the same as for elastic analysis, matrix $\boldsymbol{B}$ due to the inelastic stress integral, matrix $\boldsymbol{F}$ refers to the fundamental function caused by the forcing traction with vector $\boldsymbol{x}$, i.e. modeling the density of the crack opening, while the matrix of bond $\boldsymbol{Q}$ includes creep, bond-slip relations and other displacements due to the aggregate interlock and dowel action of reinforcement in the crack, related to displacement $\boldsymbol{u}$.

4. Incremental computations

Equation (7) must be solved numerically with iterative and incremental techniques. Iteration results are due to the fact that

the right side of Eq. (7) depends directly on functions ***u***. In addition, function ***u*** depends indirectly on the physical law i.e. Eq. (2). The incremental computation is caused by the rate form of Eq. (7). The modified Newton-Raphson method was applied to the iteration and incremental computations.

The concrete properties should be included in the biaxial domain. The biaxial tests of Kupfer, see [4], for short time loading and proportionally increasing load, proved to be the most reliable. Link, see [5], developed an incremental formulation for the tangent stiffness of the concrete on the basis of Kupfer's tests. The concrete physical law of Link, see [5], was used in the computation of the planar structure within the presented method.

The creep of concrete was taken from the Bažant's and Panula, see [6], rheological model with the creep function as below (f_c' means the 28 days compressive strength of concrete):

$$J(t,\tau) = \frac{1}{E_o(f_c')}\,[1 + \varphi_1\,(f_c')(\tau^{-m(f_c')} + \alpha(t-\tau)^{n(f_c')}]. \quad (8)$$

The $\sigma - \varepsilon$ relation of steel bars was taken as elasto-plastic relation from uniaxial tests.

After the cracking of the concrete, the tensile forces in the cracked area are transmitted by bond to the reinforcement that consists of steel bars. Along the segments of broken adhesion the steel bar interacts with the concrete through the tangential stresses distributed on the perimeter of the bar. The slip Δ is defined as a relative displacement between the reinforcement bars and surrounding concrete. The increment of tensile stresses in the steel bar was approximated by the third-degree curve. Hence, the tangential stresses τ and bond-slip relationships, as representation of the stiffness of the bond, have been found to be in agreement with the tests of Dörr and Mehlhorn, see [7], i.e. the second-degree distribution along the segment l_f, where l_f means distance between cracks.

The programme of the BEM Analysis, named *PLATE*, for two-dimensional problems was designed. The *PLATE* analysis includes the procedures of: *Modeling System (MS)*, where the model of construction is built, the *Analysis Module (AM)* where the problem with iterative and incremental method is solved and finally using *MS* the results are obtained *(RES)*. The iterative and incremental techniques used in the *(AM)* connect all material properties with crack physical laws and edges conditions.

The time-dependence of bond in the loaded state exhibits a similar behaviour as concrete in compression, see[8]. The presupposition similar to the linear creep theory of concrete in compression is used for bond creep with bond creep coefficient φ_b. Naturally in accordance with $\tau - \Delta$ relationship of Dörr and Mehlhorn, see [7], bond creep cannot be described by linear theory. The model of Rotasy and Keep, see [8], was applied to describe the creep of the bond in the cracked concrete.

The development of "rotating cracks" is considered as single cracks treated as the boundary element where the direction of the crack has to be assumed in accordance with the previous step of the main direction of the tensile stresses.

5. Numerical example

The results of a simply supported square panel *WT3* (1.6 × × 1.6 m), tested by Leonhardt and Walther, see [9], were taken to check BEM base solution for plane stresses (the comparison of the test and calculation results is included only in Fig. 1). The panel was reinforced horizontally in a different way for the bottom and top part. The bottom zone (f_{y1}) had 2ϕ8 mm bars each 6 cm fixed in 4 rows, the top zone and vertical bars (f_{y2}) were 2ϕ5 mm each 26 cm.

Fig. 1 shows the comparison of the calculated load-midspan deflection relations with the test results of panel *WT3*. Figure 2 depicts the propagation of cracks and numerical calculated width of cracks under different loading steps and time. Fig. 3 presents the midspan crack width of *WT3* panel along the dimensionless height of the panel while Fig. 4 demonstrates the dependence of the time and loading levels on the crack width a_f.

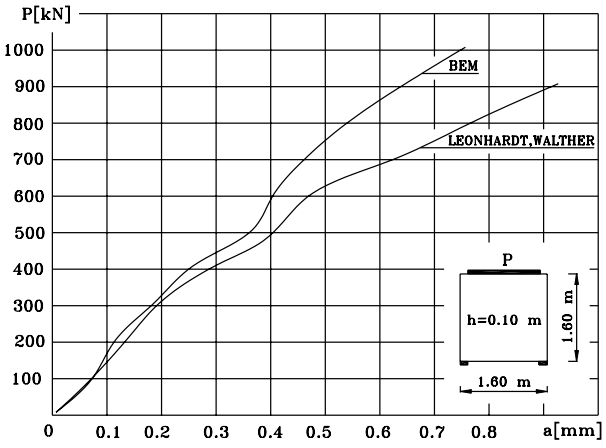

Fig. 1. Comparison of calculated load-midspan deflection relations with the test result of panel WT3 [9]

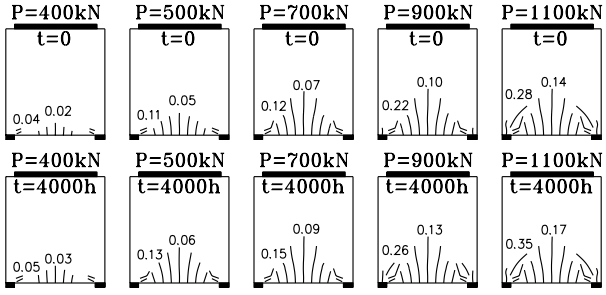

Fig. 2. The propagation of cracks and width of cracks under different loading levels and time

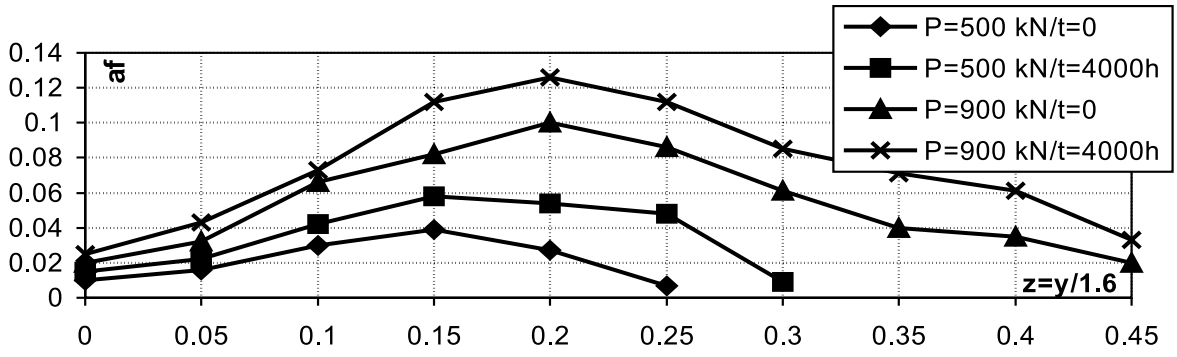

Fig. 3. The midspan crack width af of WT3 panel along the dimensionless height of the panel

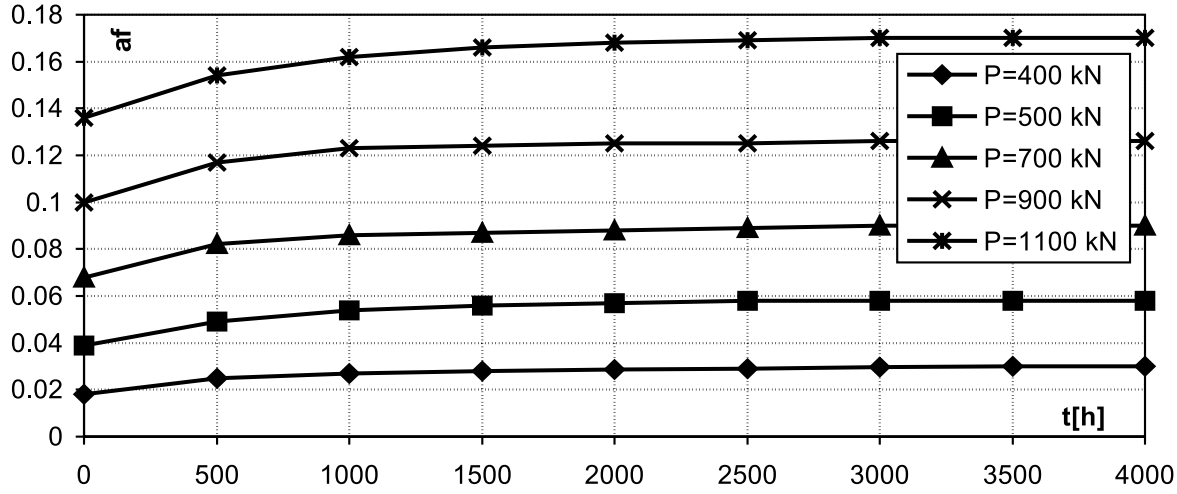

Fig. 4. The dependence of the time and loading levels on the midspan crack width af

References

[1] SCHWARTZ, L.: *Theory des distributions*. Paris, 1966.
[2] BORCZ, A.: *Podstawy teorii zarysowanych płyt żelbetowych*. TNEB, Warszawa, 1963.
[3] MINCH, M. Y.: *Boundary Element Analysis of RC Slabs and Panels.* In: Proceedings of the Twenty-Fourth Midwestern Mechanics Conference, Iowa State University, Iowa USA, ISU-ERI-Ames-95002, Developments in Mechanics, No 18, 1995, pp. 81-84.
[4] KUPFER, H.: *Das Verhalten des Betons unter mehrachsiger Kurzzeitbelastung unter besonderer Berücksichtigung der zweiachsigen Beanspruchung.* In: Deutscher Ausschuss für Stahlbeton, No 229, 1973, pp. 269-274.
[5] LINK, J.: *Eine Formulierung des zweiaxialen Verformungs- und Bruchverhaltens von Beton und deren Anwendung auf die wirklichkeitsnahe Berechnung von Stahlbetonplatten.* In: Deutscher Ausschuss für Stahlbeton, No 270, 1976.
[6] BAŽANT, Z., PANULA, L.: *Practical prediction on time-dependent deformations of concrete.* In: Mater. and Struct. Res. and Testing, No 11(65), 1978, pp. 307-329.
[7] DÖRR, K., MEHLHORN, G.: *Berechnung von Stahlbetonscheiben im Zustand II bei Annahme eines wirklichkeitsnahen Werkstoffverhaltens.* In: Forsch. aus dem Inst. f. Massivbau der Techn. Hochsch. Darmstadt, Darmstadt, No 39, 1979.
[8] ROTASY, F. S., KEEP, B.: *Untersuchung der zeit- und lastabhängigen Schlupfentwicklung von einbetonierten Bewehrungsstählen*. Institut für Baustoffe, Massivbau und Brandschutz, TU Braunschweig. 1982.
[9] LEONHARDT, F., WALTHER, R.: *Wandartige träger*. Deutscher Ausschuss für Stahlbeton, No 178, Verlag Wilhelm Ernst & Sohn, Berlin, 1966.

Jan Kubik – Zbigniew Perkowski *

POPÍSANIE KREHKÉHO POŠKODENIA BETÓNU

DESCRIPTION OF BRITTLE DAMAGE IN CONCRETE

Prezentovaný je jednoduchý model vývoja krehkého poškodenia betónu. Predpokladá sa izotropický vývoj poškodenia a úroveň poškodenia je popísaná skalárnym parametrom. Formulované sú fyzikálne rovnice problému.

A simple model of the brittle damage evolution in concrete is presented. The damage evolution is assumed as an isotropic one and the level of damages in material is described by the scalar parameter. The physical equations for this case are formulated.

1. Introduction

The processes of brittle and viscous deformations take place together especially in typical building capillary-porous materials as concrete, ceramics and gypsum [2]. An assumption, that brittle damages (microcracks) occur immediately after imposing a load on the body unlike viscous deformations which are controlled mainly by the diffusion of moisture in capillary tubes of material, is a simple way to describe this phenomenon. The global description of the considered process and its influence on the level of stresses and strains in a viscoelastic body is the aim of this paper.

2. Stress and strain transformation

The classical stress tensor transformation

$$\sigma_{ij} = O_{ik}\, O_{jl}\, \sigma_{kl}\,, \tag{1}$$

where σ_{ij} – stress tensor, O_{ik} – transformation tensor, $i, j, k, l = 1, 2, 3$, in the body with structure damages must be modified in accordance with the limitation that principal tensile stresses are the main reason of damage evolution [2, 3, 6]. That is why the stress tensor transformation must be divided into two phases (Fig. 1). First, the stress tensor must be transformed to its principal directions and next to the co-ordinate system which we want to analyse the process in [5]. We introduce here a new operation realised in the co-ordinate system compatible with the principal directions of stress tensor

$$\langle \sigma_p \rangle = \frac{1}{2}(\sigma_p + |\sigma_p|)\,, \tag{2}$$

where: σ_p – principal stresses, $p = 1, 2, 3$,

which allows us to write the transformation formula

$$\sigma^+_{ij} = O_{ik}\, O_{jl}\, [O^+_{kr}\, O^+_{ls}]\sigma_{rs} = O_{ik}\, O_{jl}\, \langle \sigma_{kl} \rangle = P^+_{ijrs}\sigma_{rs}\,, \tag{3}$$

where

$$P^+_{ijrs} = O_{ik}\, O_{jl}\, [O^+_{kr}\, O^+_{ls}]\,. \tag{4}$$

The same transformation formula is applied to the strain tensor

$$\varepsilon^+_{ij} = P^+_{ijrs}\, \varepsilon_{rs}\,, \tag{5}$$

where ε_{ij} – strain tensor.

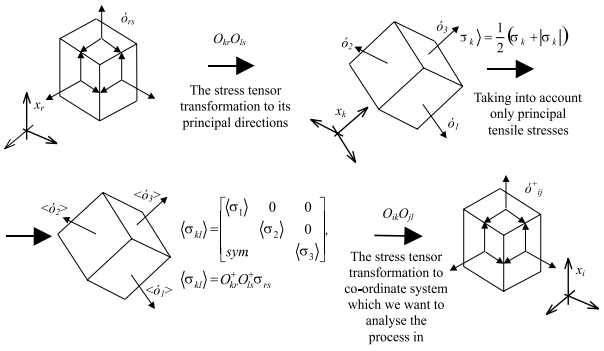

Fig. 1. Graphical interpretation of the stress tensor transformation divided into two phases.

2. Physical equations

The general form of the physical equation connecting the stress tensor with the strain tensor in an elastic material with structure damages can be formulated as follows

* [1]Prof. Dr. Eng. Jan Kubik, [2]Mgr Eng. Zbigniew Perkowski
[1] Technical University Opole, Department of Civil Engineering, Katowicka 48, 45-061 Opole,
Tel.: ++48-77-4565085, Fax: ++48-77-4565084, E-mail: kubik@po.opole.pl
[2] Technical University Opole, Department of Civil Engineering, E-mail: zbyperkow@poczta.fm

$$\sigma_{ij} = [1 - \omega]E_{ijkl}\varepsilon_{kl} = E_{ijkl}\varepsilon_{kl} - \omega E_{ijkl}\varepsilon_{kl} = \sigma^0_{ij} - \sigma^D_{ij}, \quad (6)$$

where: E_{ijkl} – tensor containing the constants which describe stiffness of undamaged material, σ^0_{ij} – total stress tensor, σ^D_{ij} – part of total stress tensor caused by damages, $\omega \in \langle 0,1)$ – dimensionless parameter describing the level of structure damages in material.

The damage parameter ω introduced in the relation (6) admits value from zero for undamaged material, to one for fully damaged material. It determines a change of unitary bearing surface as a result of microcracks growth and degeneration of material structure. The value of the damage parameter depends in the presented process on the state of stress, hence it must be determined from the kinetic equation

$$\dot{\omega} = f(\sigma), \;\; \omega(t = 0^+) = 0, \quad (7)$$

where: t – time.

The second component σ^D_{ij} in the relation (6) expresses an influence of damages on the stress distribution. Taking into account the transformation formula (3) we can get

$$\sigma^D_{ij} = \omega P^+_{ijrs}E_{rskl}\varepsilon^+_{kl} = \omega P^+_{ijrs}E_{rskl}P^+_{klmn}\varepsilon_{mn} = \omega E^+_{ijkl}\varepsilon_{kl}. \quad (8)$$

Finally, the physical equation (6) has the form

$$\sigma_{ij} = E_{ijkl}\varepsilon_{kl} - \omega E^+_{ijkl}\varepsilon_{kl}. \quad (9)$$

Based on (9) in an analogous viscoelastic problem the relation between the stress tensor and the strain tensor can be written as

$$\sigma_{ij} = [E_{ijkl}(t) - \omega E^+_{ijkl}(t)]^* d\varepsilon_{\mathrm{kl}}, \quad (10)$$

where $E_{ijkl}(t)$ – relaxation functions tensor.

The equation above describes stresses in a quasi linear viscoelastic body with structure damages. So there is need, in real problems, to take into consideration changes of stresses during the whole process of deformations. Therefore, we must use the incremental form of the relation (10)

$$\Delta\sigma_{ij} = [E_{ijkl}(t) - \omega E^+_{ijkl}(t)]^* d\Delta\varepsilon_{\mathrm{kl}}. \quad (11)$$

It is worth mentioning that the form of the equations (10) and (11), where the linear part is clearly separated from the non-linear one which contains an influence of damages, allows us to formulate stable procedures of computations and global laws (for example reciprocity principle).

4. Thermomechanics of the process

The thermomechanical description of damage evolution in material demands us to define independent fields. We will take into considerations the strain tensor, the entropy and the damage parameter ω as an internal variable. We also assume that viscoelasticity holds and the internal energy is a functional which describes our process

$$\rho U = \rho U(\varepsilon_{ij}, S; \omega), \quad (12)$$

where: U – internal energy, S – entropy, ρ – mass density.

These assumptions allow us to obtain the residual inequality [2, 6]

$$-\rho\dot{U} + \theta\rho\dot{S} + \sigma_{ij}\dot{\varepsilon}_{ij} - \frac{q_i\,\theta_{,i}}{T_0} \geq 0, \quad (13)$$

where: S – entropy, q_i – heat flux, T_0 – initial temperature, θ – temperature gain, $(\dot{})$ - local time derivative,

which is obtained from the balance of energy and the inequality of entropy increase, as a result of "typical thermomechanical considerations". It is worth mentioning that the condition (13) should be satisfied in every real process. Then we can approximate the internal energy (12) with the following polynomial

$$\rho U = \rho U_0 - \sigma^0_{ij} * d\varepsilon_{ij} + \frac{1}{2}m(\rho S)^2 + \frac{1}{2}E_{ijkl}(t) * * d\varepsilon_{kl} * d\varepsilon_{ij} - \frac{1}{2}\omega E^+_{ijkl}(t) * d\varepsilon_{kl} * d\varepsilon_{ij} + R, \quad (14)$$

where: U_0, σ^0_{ij} – initial internal energy and initial stress tensor, m – material constant, R – remainder of polynomial.

The time derivative of internal energy expressed as (14) introduced to the expression (13) will finally give the inequality

$$(\theta - m\rho S)\rho\dot{S} + (\sigma_{ij} - E_{ijkl}(t) * d\varepsilon_{kl} + \omega E^+_{ijkl}(t) * * d\varepsilon_{kl} + \sigma^0_{ij})\dot{\varepsilon}_{ij} - \frac{1}{2}\frac{\partial}{\partial t}(E_{ijkl}(t) * d\varepsilon_{kl} * d\varepsilon_{ij}) + + \frac{1}{2}\frac{\partial}{\partial t}(\omega E^+_{ijkl}(t) * d\varepsilon_{kl} * d\varepsilon_{ij}) + \frac{1}{2}\dot{\omega}E^+_{ijkl}(t) * d\varepsilon_{kl} * * d\varepsilon_{ij} - \frac{q_i\,\theta_{,i}}{T_0} \geq 0. \quad (15)$$

An assumption that the above condition holds in any real state of the strain tensor and the entropy is tantamount to the following relations

$$\theta = m\rho S,$$

$$\sigma_{ij} = E_{ijkl}(t) * d\varepsilon_{kl} - \omega E^+_{ijkl}(t) * d\varepsilon_{kl} - \sigma^0_{ij}, \quad -\frac{1}{2}\frac{\partial}{\partial t}(E_{ijkl}(t) * d\varepsilon_{kl} * d\varepsilon_{ij}) + \frac{1}{2}\frac{\partial}{\partial t}(\omega E^+_{ijkl}(t) * d\varepsilon_{kl} * * d\varepsilon_{ij}) + \frac{1}{2}\dot{\omega}E^+_{ijkl}(t) * d\varepsilon_{kl} * d\varepsilon_{ij} \geq 0, \quad (16)$$

$$\rho_i\,\theta_{,i} \geq 0.$$

Neglecting thermal influences, initial stresses and viscous power dissipation

$$\theta \cong 0,\; q_1 \cong 0,\; \sigma^0_{ij} \cong 0$$

$$-\frac{1}{2}\frac{\partial}{\partial t}(E_{ijkl}(t) * d\varepsilon_{kl} * d\varepsilon_{ij}) + \frac{1}{2}\frac{\partial}{\partial t}(\omega E^{+}_{ijkl}(t) * d\varepsilon_{kl} * * d\varepsilon_{ij}) \cong 0 \quad (17)$$

we will get the physical equation for the stress tensor

$$\sigma_{ij} = E_{ijkl}(t) * d\varepsilon_{kl} - \omega E^{+}_{ijkl}(t) * d\varepsilon_{kl}, \quad (18)$$

and the condition for the damage evolution

$$\frac{1}{2}\dot{\omega}E^{+}_{ijkl}(t) * d\varepsilon_{kl} * d\varepsilon_{ij} \geq 0. \quad (19)$$

In the principal stresses space we can obtain from (19)

$$\frac{1}{2}\dot{\omega}\langle\sigma_k\rangle * d\varepsilon_k \geq 0. \quad (20)$$

From the condition above we can conclude that the increase of damage parameter is closely connected with the work of the principal tensile stresses on the strains. Making an assumption that the damage process is an irreversible one we can postulate the damage evolution equation

$$\dot{\omega} = CE^{+}_{ijkl}(t) * d\varepsilon_{kl} * d\varepsilon_{ij}, \; C \geq 0, \quad (21)$$

where: C – material parameter.

5. Determination of the damage parameter

The damage evolution and connected with this process the strength drop are dependent on the velocity of strains and stresses. The increase of velocity of a load raises the final strength, reduces the strains at the maximal stress and the dependence stress-strain is closer to a linear one. This phenomenon is connected with the inertia of concrete on mikrocracks. Tensile stresses have more considerable influence on the change of strength than compressive ones [4] (Fig. 2). The experimental description of this process is presented in the work [1], where the tensile strength, the strain at the maximal stress for concrete are dependent on the velocity of strain

$$f_{ctm} = f_{ctm,0}\left(\frac{\dot{\varepsilon}}{\dot{\varepsilon}_0}\right)^{\delta_1}, \; \delta_1 = \frac{1{,}016}{10 + 0{,}5\, f_{ctm,0}}, \quad (22)$$

$$\varepsilon_{ct} = \varepsilon_{ct,0}\left(\frac{\dot{\varepsilon}}{\dot{\varepsilon}_0}\right)^{\delta_2}, \; \delta_2 = -0{,}020, \quad (23)$$

where: $\dot{\varepsilon}_0$ – reference velocity of strain (in the work [1] $\dot{\varepsilon}_0 = 3 \cdot 10^{-6}$ [s^{-1}]), $\dot{\varepsilon}$ – velocity of strain, $f_{ctm,0}$ – tensile strength for reference velocity of strain, $\varepsilon_{ct,0}$ – strain at tensile strength for reference velocity of strain, ε_{ct} – strain at tensile strength.

The determination of the value of damage parameter from the relation (21) can be simplified after taking into account the assumptions presented in the introduction. Damages in material appear immediately after imposing a load, in contrast to the process of creep, so the damage evolution equation can be written as

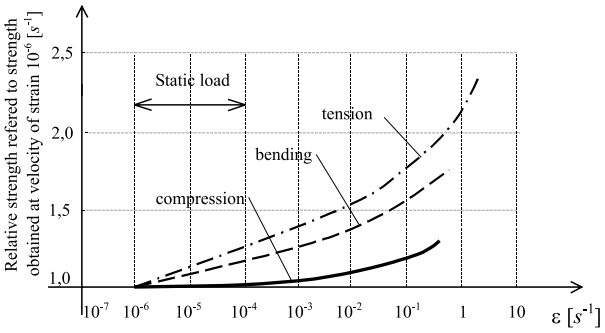

Fig. 2. Influence of velocity of strain on relative strength of concrete during tension, bending and compression.

$$\dot{\omega} = CE^{+}_{ijkl}\,\varepsilon_{kl}\,\varepsilon_{ij}, \; C \geq 0. \quad (24)$$

Hence, in the case of increase of strain at a constant velocity under uniaxial state of stress, the damage parameter is described by the following formula

$$\omega = \frac{CE_0\varepsilon^3}{3\dot{\varepsilon}}, \; \dot{\varepsilon} = const., \quad (25)$$

where: E_0 – initial Young`s modulus ε – strain in uniaxial state of stress.

A typical curve determining the relation $\sigma - \varepsilon$ in uniaxial state of tensile stress for concrete is illustrated in Fig. 3,

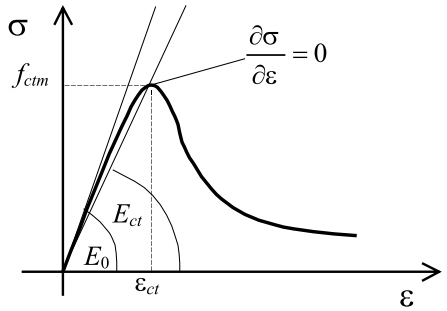

Fig. 3. Relation in uniaxial state of stress.

where: E_{ct} – secant Young`s modulus, f_{ctm} – tensile strength.

Taking into account that the tangent to the curve $\sigma - \varepsilon$ in point $(\varepsilon_{ct}, f_{ctm})$ is equal to zero we can calculate the unknown material parameter C

$$C = \frac{9\dot{\varepsilon}E^2_{ct}}{16f^3_{ctm}}, \quad (26)$$

which is a function of velocity of strain. That means we must use the incremental form of relation (25) to describe the damage parameter for changeable velocity of strain

$$\Delta\omega = \frac{C(\dot{\varepsilon})E_0\,\Delta\varepsilon^3}{3\dot{\varepsilon}}. \quad (27)$$

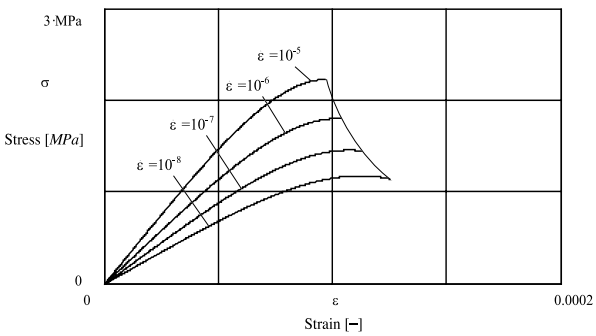

Fig. 4. Stress at tension for different velocities of strain.

Character of the physical relation (9) in the uniaxial state of stress with taking into account relations (25) and (26) is shown in Fig. 4. (for example, parameters of concrete $\dot{\varepsilon}_0 = 3 \cdot 10^{-6}[s^{-1}]$, $f_{ctm,0} = 2$ [MPa], $\varepsilon_{ct.0} = 10^{-4}$ [-]).

6. Conclusions

1. The physical equations including the influence of principal tensile stresses on destruction of concrete are formulated.
2. The limitation for the process of damage evolution is obtained from the thermomechanical considerations.
3. Presented formulas describing the damage evolution can be helpful for the estimation of exploitation time of concrete.

Referencec

[1] EIBL J., *Concrete Structures under Impact and Impulsive Loading*, Bulletin d`Information No. 187, Contribution à la 26 Session Plénière CEB, Dubrownik, 1988
[2] KUBIK J., PERKOWSKI Z.: *Description of the damage growth in concrete,* 3rd Scientific – Technical Conference Matbud `2000, 208-215, Kraków, 2000 (in Polish)
[3] LITEWKA A., DĘBIŃSKI J.: *The anisotropic model of the deformability of concrete under multiaxial state of stress,* XLIII Scientific Conference KILiW PAN and KN PZITB, Poznań-Krynica, 1997 (in Polish)
[4] McHENRY D., SHIDELER J. J.: *Review of data on effect of speed in mechanical testing of concrete,* ASTM Sp. Tech. Publ. Nr 185, 72-78, 1956
[5] ORTIZ M.: *A constitutive theory for the inelastic behaviour of concrete,* Mech. of Mat. 4, 67-93, 1985.
[6] PERKOWSKI Z.: *Description of the deformability of concrete with damages,* ZN 89 Politechniki Śląskiej, S. Civil Engineering, 163-170, Gliwice, 2000 (in Polish).

Ján Bujňák – Kazimierz Furtak – Jaroslav Odrobiňák *

NAVRH ŠMYKOVEHO SPOJENIA V SPRIAHNUTÝCH TRÁMOCH

ON SHEAR CONNECTION DESIGN IN COMPOSITE BEAMS

Článok sa zaoberá spôsobom určenia pevnosti betónu v tlaku pre výpočet únosnosti oceľovej perforovanej lišty. Tento typ prvkov spriahnutia sa začal používať pri kompozitných spriahnutých mostoch len nedávno a doteraz neexistuje presná metóda ich posúdenia. Ako výsledok výskumu článok ďalej prezentuje analýzu vplyvu osových síl na únosnosť klasického typu prvkov spriahnutia, ktorými sú tŕne.

The paper deals with a way of determining concrete pressure strength when calculating load carrying capacity of steel perfobond strip connectors. This type of strip connectors has been used in composite bridges only recently and no precise methods of calculating them have been worked out so far. The effect of axial forces on bearing capacity of classical stud shear connectors is also given in the paper as a result of research.

1. Introduction

There is no explicit definition of concrete pressure strength $\bar{f}_{cud}$ because there are no standard principles of defining this strength. This is why it may be difficult to adopt design values for particular classes of concrete in actual engineering practice. Moreover, the experimental investigations in this field are done on different samples for different areas of pressure. Hence, significant discrepancies exist in the propositions by various authors, and even norm values.

The stud connector's behaviour depends not only on their bearing and shear resistance. The axial forces may modify importantly the ultimate load bearing capacity. The effect of this action is also given in the paper as a result of research.

2. Test elements and research methodology

In case of perfobond strip connectors, there are special conditions of concrete pressure. It is a pressure of two cylindrical surfaces of small dimensions. The strips thickness range can be from $t = 12$ mm to 20 mm, and the diameter of holes is from $\Phi = 30$ mm to 40 mm.

Moreover, the distribution of pressure stress on the concrete-strip contact area differs in comparison to classical cases. It can be assumed to be close to the one adopted by Hertz's formulae. However, these formulae cannot be adopted for calculating $\bar{f}_{cud}$ because of significant non-homogeneity of concrete and big differences between mechanical characteristics of aggregate and cement set. Moreover, the relatively thin steel strip acts on concrete like a wedge.

Due to the specific character of problems of concrete pressure in perforated strips, the only solution seems to be experimental investigations. They are recommendable also because of the limited range of values of the essential parameters, i.e. strip thickness, hole diameters and concrete class.

The sizes of the elements used in tests are shown in Fig. 1. The elements were cubes of a side $a = 150$ mm, with an additional bulge in the shape of a half-round of diameter matching the diameter of the holes in the perforated strips used in steel-concrete composite structures. The pressure force has been transferred by a steel element with a half-round of the same diameter as the bulge on the concrete cube and the thickness corresponding to the thickness of the strip.

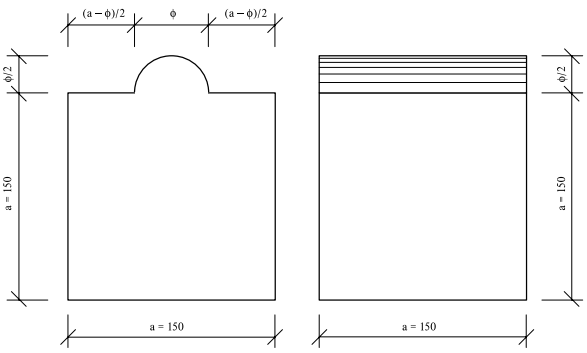

Fig. 1. Shape and dimensions of test samples

* [1]Prof. Ing Ján Bujňák, CSc., [2]Prof. Kazimierz Furtak, D.Sc., PhD., [1]Ing. Jaroslav Odrobiňák
[1] Faculty of Civil Engineering, University of Žilina. Komenského 52, 010 26 Žilina, Slovakia. Tel: ++421-41-7635651,
E-mail: bujnak@fstav.utc.sk, odrobin@fstav.utc.sk
2 Department of Bridges and Tunnels Building, Faculty of Civil Engineering, Cracow University of Technology. Warszawska 24, 31155 Cracow, Poland, Tel/fax : ++48-012-6282024

For the adopted shape of the test elements, concrete ultimate pressure strength was obtained, which can be used directly in calculating perfobonds load carrying capacity. To this aim, the following test parameters were adopted: thickness of perfobonds, diameters of holes and concrete class.

Three classes of concrete were used: B30, B40 and B50 with three diameters of holes: $\Phi = 20$, 30 and 40 mm and three thicknesses of the strips: $t = 12$, 16 and 20 mm. The basic parameters used were: the concrete class B40, the hole diameter $\Phi = 30$ mm and the strip thickness $t = 16$ mm. As a total, the 114 elements have been examined.

The tests were run on a standard testing machine. The rate of loading was 0.4 MPa.s^{-1}, the given stress was calculated by dividing the pressure force by the product of strip thickness and hole diameter. The tests elements were stored in normal (laboratory) conditions.

3. Test results and their analysis

The tests of strength characteristics of the concrete from which the test elements were made had provided the following values of concrete mean compressive strength and tensile strength:

- concrete class B30: $\bar{f}_c = 34.80$ MPa, $\bar{f}_t = 2.36$ MPa,
- concrete class B40: $\bar{f}_c = 45.96$ MPa, $\bar{f}_t = 3.08$ MPa,
- concrete class B50: $\bar{f}_c = 61.10$ MPa, $\bar{f}_t = 4.10$ MPa.

The concrete compressive and tensile strength for splitting were determined on cubes of sides of 150 mm. For strength characteristics tests ($\bar{f}_c$, $\bar{f}_t$), each series have contained six elements. The tests were done in a standard way. The cubes for $\bar{f}_c$ and $\bar{f}_t$ were stored in natural conditions, similarly as samples for compressive tests.

The results of the compressive tests are shown in Figs 2 to 5. Fig. 2 illustrates the effect of strip thickness for different concrete classes, while Fig. 3 the effect of hole diameter. As it can be clearly seen, there is a strong decreasing tendency of compressive strength $\bar{f}_{cud}$ with the increase of strip thickness and hole diameters. The approximately linear change of concrete strength $\bar{f}_{cud}$ dependence on t and Φ is worth to underline.

For design purpose, it is much more useful to have concrete compressive strength $\bar{f}_{cud}$ as a function of the pressure area $A_p = t \cdot \Phi$. This pressure can be defined as a product of the strip thickness t and the hole diameter Φ. This is a simplification due to adopted assumption of the mean values of stresses. In reality, the distribution of stresses on the pressure semi-perimeter is quite variable, especially in the case of homogeneous materials.

The effect of pressure area A_p on concrete strength $\bar{f}_{cud}$ is illustrated in Fig. 4. The dependence is clearly non-linear and may be well approximated by a logarithmic function. Generally, with the larger pressure area the lower $\bar{f}_{cud}$ strength results. However, it should be noted, that the decrease of pressure strength in real practical ranges of pressure area is even doubled.

Fig. 5 shows the dependence of the concrete pressure strength $\bar{f}_{cud}$ on its class (represented by compressive strength $\bar{f}_c$) and pressure area A_p.

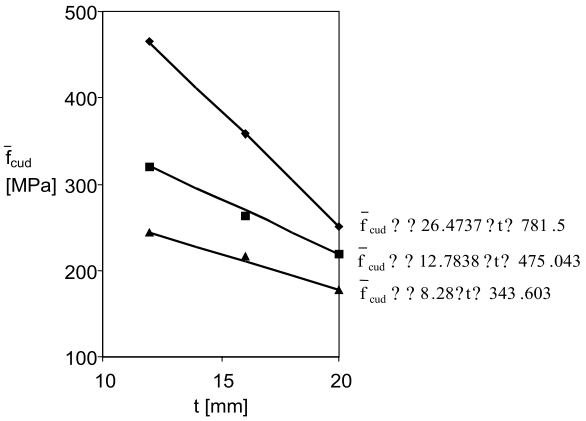

Fig. 2. Effect of strip thickness on pressure strength of concrete class B40

The results of experimental investigations illustrated in Fig. 2 to 5 are an arithmetic mean obtained from the whole series of 3 to 6 elements. The figures show approximation curves, which can be used for determining concrete pressure strength when designing perforated strips in composite structures.

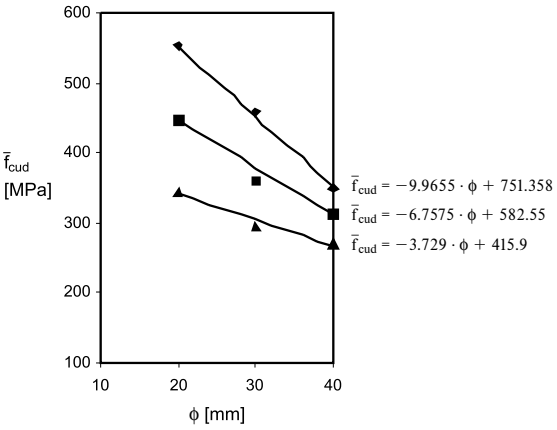

Fig. 3. Effect of hole diameter on pressure strength of concrete class B40

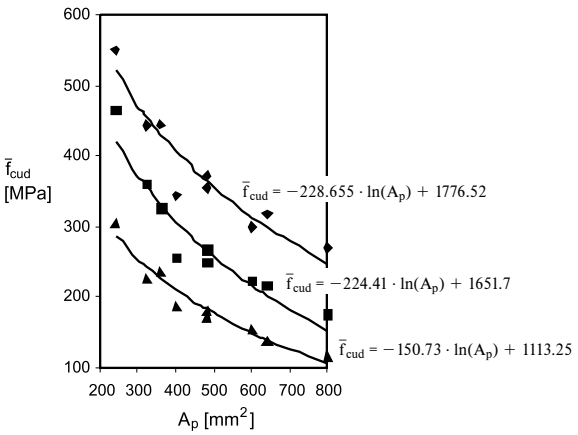

Fig. 4. Effect of pressure area on pressure strength of concrete

For design purposes, it can be preferable to have a simultaneous dependence of concrete pressure strength $\bar{f}_{cud}$ on compressive strength $\bar{f}_c$ and pressure area A_p. Dependence $\bar{f}_{cud} = \bar{f}_{cud}(\bar{f}_c, A_p)$ can be written as:

$$\bar{f}_{cud} = (8.30 \cdot \bar{f}_c - 56.70) \cdot \kappa \tag{1}$$

$$\kappa = 1.46 \cdot \lambda^{0.4} + 2.46 \tag{2}$$

$$\lambda = \frac{A_p}{360} \tag{3}$$

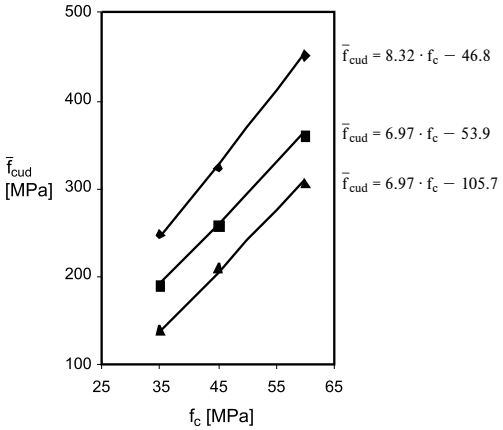

Fig. 5. Dependence of pressure strength on concrete class and pressure area

In the formulae above $\bar{f}_c$ and $\bar{f}_{cud}$ are expressed in [MPa] and the pressure area $A_p = t \cdot \Phi$ in [mm^2]. Formula (1) is valid for 360 mm^2 $\leq A_p \leq$ 600 mm^2. It gives the mean strength. The characteristic strength and design one can be determined using the same calculations as for concrete compressive strength.

4. Influence of axial forces on shear strength

The normal forces across the concrete and steel interface in the direction of the axis of the stud connector shank apply concentrated local loads. The axial compressive forces are resisted by bearing of the slab onto the steel beam flange and they rarely pose a problem. In contrast, the axial tensile actions can cause a separation between the composite elements or more often embedment concrete slab cracking. The shear strength of stud connectors is strongly influenced by the axial force across the steel and concrete interface. This resulting strength of push-test in which the base is free to slide [4] is substantially less than in the case of the fixed base. This reduction in shear strength is due to the change of the resultant axial force at the interface from compression when the base is fixed to tension for the studs in the case of sliding base. The shear strength of headed studs can be degraded up to a third when the base is free to slide. The value of embedment forces in composite beams is generally considerably less than in the push-tests because of the difference between the boundary restraint conditions in the two systems.

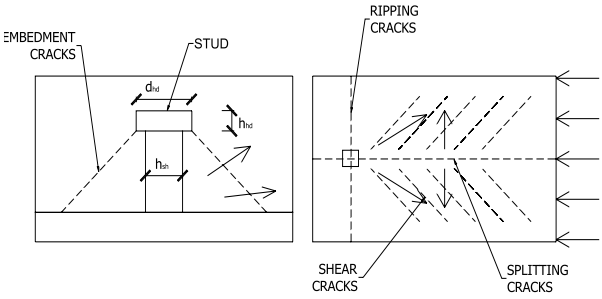

Fig. 6. Conical failure plane, dimensions of the stud connector

The axial load can cause failure of the stud shank at the axial tensile strength

$$N_d = A_{sh} \cdot f_u, \tag{4}$$

where A_{sh} is the cross-sectional area of the stud shank and f_u its design tensile strength.

Alternatively, the connector can be pulled out of the slab forming a concrete cone around it (Fig. 6). The surface area of this conical failure plane is used for deriving the following axial embedment strength

$$N_d = 1.5 \cdot \sqrt{f_{ck}} \cdot h_{sh}(h_{sh} + d_{hd}), \tag{5}$$

in which f_{ck} is the compressive cylinder strength of the concrete and the remaining dimensions are defined in Fig. 6.

The shear dowel strength of stud connectors is given by a standard equation

$$P_d = 0.8 \cdot f_u \cdot \frac{\pi \cdot d_{sh}^{\,2}}{4}, \tag{6}$$

the other equation should control shear connector steel shank strength

$$P_d = 0.29 \cdot \alpha \cdot d_{sh}^{\,2} \cdot \sqrt{f_{ck} \cdot E_{cm}}\,. \tag{7}$$

5. Interaction between shear and axial forces

The axial forces on the shear connection can produce the elements separation. As a result, the tensile force at the stud head increases and the probability of embedment failure becomes greater. The critical tensile failure in the weld collar zone is in the same time more likely to fail when the axial tensile forces are applied. It is therefore necessary to determine the interaction between shear and axial effect.

The elliptical interaction curve proposed in [5] is

$$\left(\frac{P_{Sd}}{P_d}\right)^{\frac{2}{3}} + \left(\frac{N_{Sd}}{N_d}\right)^{\frac{2}{3}} = 1.0\,. \tag{8}$$

This failure envelope is represented in Fig. 7.

The alternative method of considering effect of axial forces on the shear strength of connectors is based on changing the tensile strength of the connector [6]. If the axial tensile stress $\sigma_{Sd} = N_{Sd}/A_{sh}$ is applied, the equivalent design tensile strength of a connector is reduced by relationship

$$R_{d,ekv} = \left(1 - \frac{\sigma_{Sd}}{f_u}\right) \cdot R_d . \qquad (9)$$

It can be seen in Fig. 7 that the expression for quantifying the effects of axial forces on the shear strength of stud connector is a lower bound to the previous failure envelope.

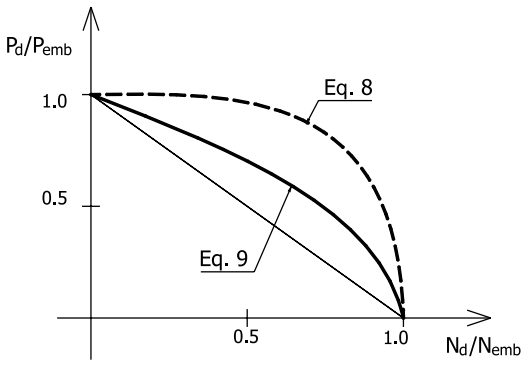

Fig. 7 Shear-axial failure envelope

6. Conclusions

The paper deals with concrete pressure strength $\bar{f}_{cud}$ in strip connectors of composite structures. The propositions of determining $\bar{f}_{cud}$ have been based on the results of the experimental investigations, which were done within the framework of the grant of the Committee for Scientific Research.

The formulae quoted are valid for the parameters of strip thickness, hole diameters and concrete class adopted in the research. They cannot be extrapolated beyond the extreme values of Φ (20 ÷ ÷ 40 mm), t (12 ÷ 20 mm) and A_p (360 ÷ 600 mm^2). Interpolation is possible in the range of the given maximum values.

In design of a composite concrete slab with a steel girder using perforated strips, it can be considered as minimum value of pressure strength $f_{cp} = \omega \cdot f_c = 4 \cdot f_c$ with pressure area not larger than 600 mm^2 and concrete class at least B30. With pressure area not exceeding 360 mm^2 and concrete class at least B30 even $\omega = 5$ can be adopted.

Mechanical connectors impose very high concentrated load onto the concrete element. The load is transferred from the steel beam to the concrete through the dowel action of the connectors. The tensile cracks caused by shear and splitting actions can be avoided by design procedures in paper [7]. The embedment cracks caused by tension, resisting separation at the steel and concrete interface of composite beam can be assessed according to the described procedure.

References

[1] PN-B-03264: 1999: *Konstrukcje betonowe, żelbetowe i sprężone.* Obliczenia statycznei projektowanie.
[2] PN-84/B-03264: *Konstrukcje betonowe, żelbetowe i sprężone.* Obliczenia statyczne i projektowanie.
[3] PN-91/S-10042: *Objekty mostowe.* Konstrukcje betonowe, żelbetowe i sprężone. Projektowanie.
[4] BUJŇÁK, J., ŠIMALOVÁ, M.: *On Determination of Shear Connection Behaviour by PushTest.* Proceedings of "Transcom '97", Žilina, 1997, pp. 270-230.
[5] OLLGAARD, J. O., SLUTTER, R. G., FISHER, J. W.: *Shear Strength of Stud Connectors on Light Weight and Normal Weight Concrete.* Engineering Journal AISC, April 1971.
[6] BUJŇÁK, J.: *Navrhovanie oceľobetónových trámov.* Vydavateľstvo ŽU v Žiline, 1997.
[7] BUJŇÁK, J.: *Shear connection in composite beam structure,* Proceedings "Mosty zespolone - Konferencja naukowo-techniczna", Kraków, 1998, pp. 21-28.

Jaroslav Odrobiňák – Aarne Jutila *

POZDĹŽNY ŠMYKOVÝ TOK V PODPEROVEJ OBLASTI TRÁMU S PREVISLÝM KONCOM

LONGITUDINAL SHEAR FLOW AT THE SUPPORT AREA OF BEAM WITH AN OVERHANGING CANTILEVER

Príspevok sa zaoberá šmykovým tokom v tráme pri jeho podpere. Skúma najmä konzolovú časť, ktorú v skutočnosti majú všetky typy trámov bez ohľadu na materiál a rozpätie. Parametrická štúdia rozdelenia šmykových napätí po výške prierezu sa realizovala metódou konečných prvkov. Uvádza výsledky najmä pre konzolovú časť. Vyúsťuje do formulácie záverov pre prax.

The paper deals with longitudinal shear flow of beams near the support area. Special interest is focused on the overhanging part, which exists in all kinds of beams irrespective of material and span. A parametric study on shear stress distribution at several horizontal height levels by using FEM is presented. Special emphasis is paid to the cantilever length. Finally, conclusions for practical applications are summarized.

1. Introduction

In practical design of bridge girders, knowledge of shear stress distribution at a certain horizontal height level of a beam is often needed. As example, the design of shear connectors of the commonly used steel-concrete, wood-concrete or concrete-concrete composite girders can be mentioned. This knowledge is also required when designing fillet welds of welded steel plate girders.

For simple calculations, the beam theory is obviously used. Thus, when the girder width is not taken into account, the shear flow is represented by the well-known formula

$$n_\tau(x, z) = \frac{V(x) \cdot S'(z)}{I}, \qquad (1)$$

where $V(x)$ is the internal shear force, $S'(z)$ is the static moment of partial area with respect to the vertical level considered and I represents moment of inertia, respectively.

However, in some cases this theory produces wrong prediction of stress distribution. This can be clearly seen above support areas because of two main reasons. Firstly, the beam is not a line but has indispensable height and is supported and loaded not on its axis but at the horizontal and bottom surfaces, respectively. Secondly, the support reaction forces do not act at the corner points of the girder, which means that additional cantilever parts always exist. Thus, the longitudinal shear stresses are affected by local stresses caused by reaction, which can be considered as local force. The disc (wall) effect in this area is usually significant and therefore this area should be considered as a two-dimensional problem at least.

2. Theoretical background

Stresses at the support area can be described by the disc (plane) theory according to the basic equation of theoretical mechanics, namely

$$\nabla^4 \phi(x, z) = 0, \qquad (2)$$

where $\phi(x, z)$ is Airy's stress function. The solution of this problem is complicated. An improvement of the beam theory, based on several simplifications and solutions of partial differential equation (2), can be found. When the reaction force is placed at the corner point, the solution consists of superposition of stresses caused by external load, reaction force and stresses due to boundary conditions. No detailed comments are presented hereby since such procedure can be found in mathematical form e.g. in [1]. A similar method based on several steps may be developed for the case of "infinite" long cantilever behind the support. Anyway, in practical cases the cantilever has a finite length. In such conditions, it is very difficult to find a practically applicable analytical solution and that is why a numerical approach based on FEM seems to be needed. Although no analytical rules for shear stress distribution can be obtained from FEM, it is important to realize, that this approach offers a possibility to investigate the influence of various parameters. One of those parametric studies is presented here.

* [1]Ing. Jaroslav Odrobiňák, [2]Dr Tech. Aarne Jutila
[1]Faculty of Civil Engineering, University of Žilina. Komenského 52, 010 26 Žilina, Slovakia. Tel: ++421-41-7635651, E-mail: odrobin@fstav.utc.sk
[2]Professor of Bridge Engineering, Helsinki University of Technology. P.O. Box 2100, 02015 HUT, Espoo, Finland.
Tel: ++358-9-4513700 E-mail: aarne.jutila@hut.fi

3. Parametric study

In this study, the effect of the size of a cantilever located beyond the support line is discussed. A one-meter high and 10 meters span simply supported beam with rectangular cross-section is considered (Fig. 1).

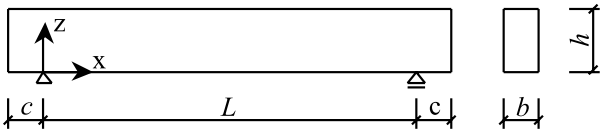

Fig. 1. Scheme of the beam. L = 10 m, h = 1 m, b equals to unit width and c is variable.

Because all stresses are supposed to depend linearly on the width, this dimension can be taken equal to unity and thereinafter its further consideration is not needed. The cantilever length, *c*, is varied from zero to the height of the beam, i.e. from $0 \cdot h$ to $1.0 \cdot h$. Two load cases are considered. The first case consists of one unit force in the middle of the span. The uniformly distributed unit load between the supports is considered in the other load case. The longitudinal shear flow is investigated at the horizontal levels ("z" coordinate according to Fig. 1) with *z/h* ratio equal to 0.5, 0.6, 0.7, 0.8 and 0.9, respectively. These positions correspond to the S'/I ratios 1.5, 1.44, 1.26, 0.96 and 0.54, respectively. The ratio S'/I reflects the value required in equation (1).

A combined mesh of quadrangle and triangle finite elements in FEM program was chosen. The support was considered as a point constraint. In reality, certain length over which is reaction distributed always exist. However, when very fine mesh of FE is used (Fig. 2) and only further horizontal levels are studied, the point reaction can be used with sufficient accuracy as well.

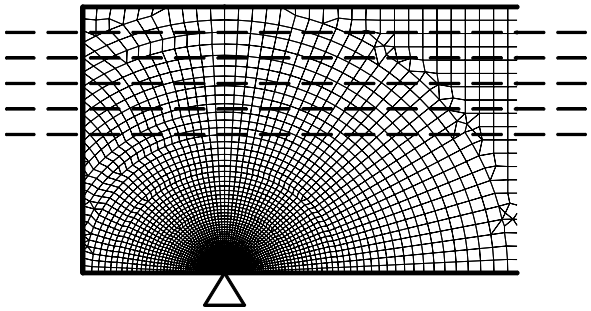

Fig. 2. Part of FEM model with studied horizontal levels

For example, in Fig. 3, results obtained by using six different cantilever lengths with S'/I ratio equal to 1.44 are presented. Only the cantilever part and a length corresponding to one fifth of the span are shown. In Fig. 4 is shown the same relationship but in the case of S'/I ratio equal to 0.96.

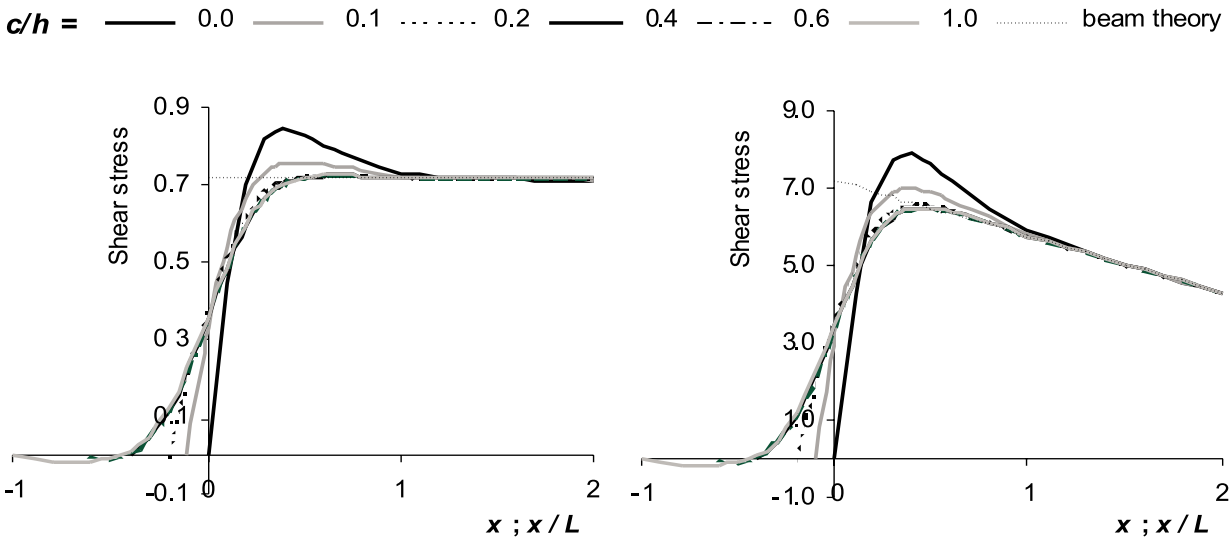

Fig. 3. Longitudinal shear stresses at support area, when $S'/I = 1.44$ and the load consists of a) a single force in the middle and b) uniformly distributed load over the span.

In Fig. 5, a detailed view on the cantilever part is presented when S'/I ratio is equal to 0.96. From the graphs and other results not presented here, it is evident that a shear stress peak can occur in front of the support within an area whose length is approximately equal to the height of the beam. The length of cantilever has influence on distribution of this peak behind the support, however, the overhang longer than $0.4 \cdot h$ is found to be useless.

From the next picture, Fig. 6, it is also obvious that in the support cross-section, around 50 % of the shear flow can remain at each considered horizontal level, if the cantilever is longer than $0.2 \cdot h$.

The percentage increase of longitudinal shear flow in the peaks mentioned before is expressed in Fig. 7. It is visible that when the cantilever length is more than $0.3 \cdot h \sim 0.4 \cdot h$, the stress peak is less

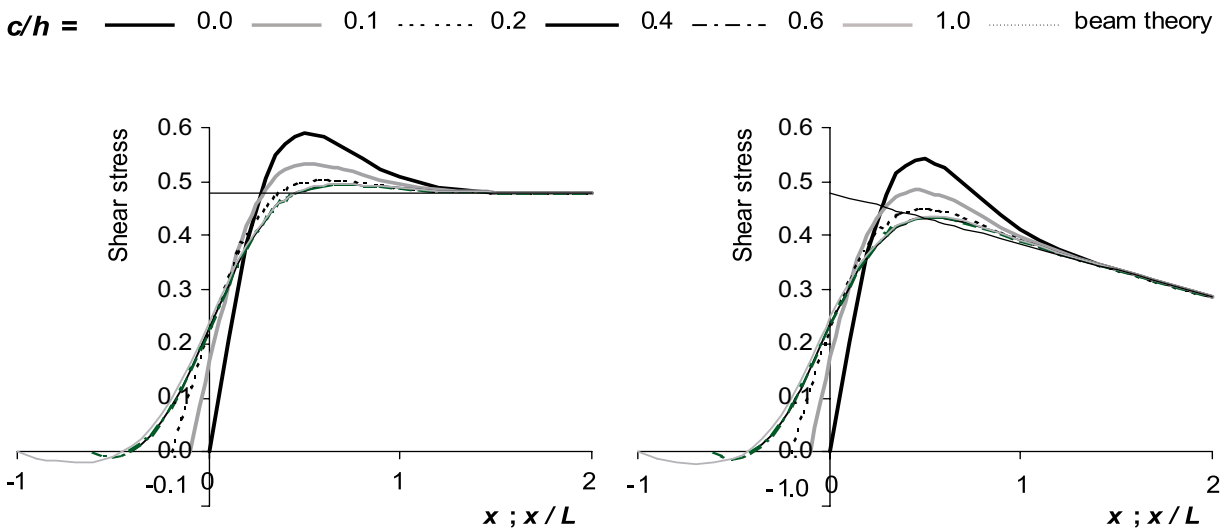

Fig. 4. Longitudinal shear stresses at support area, when $S'/I = 0.96$ and the load consists of a) a single force in the middle and b) uniformly distributed load over the span.

than 5 % at all considered levels and probably can be neglected. When the cantilever becomes shorter, local stresses can cause a significant stress peak compared to that obtained through the beam theory and especially at the higher horizontal levels of the girder.

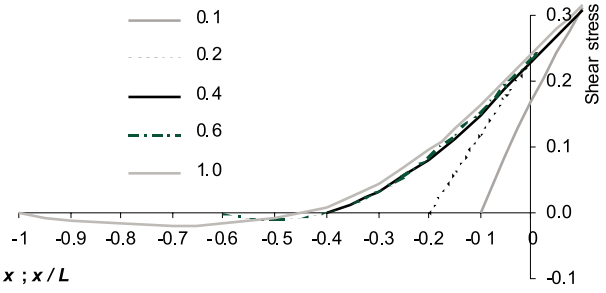

Fig. 5. Longitudinal shear stresses at cantilever area for S'/I ratio equal to 0.96 when a single force is situated in the middle of the span

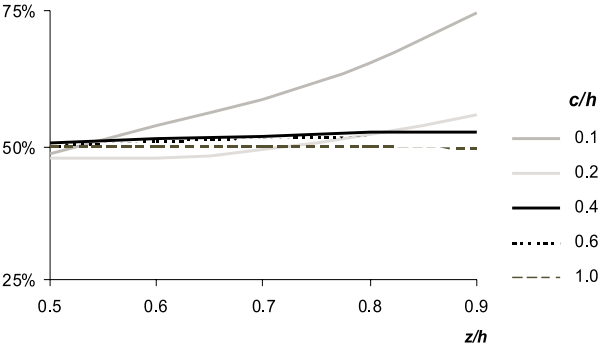

Fig. 6. Percentage remains of longitudinal shear stresses in the support cross-section compared to the beam theory.

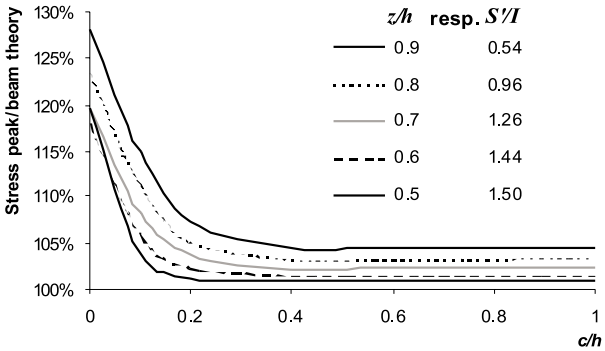

Fig. 7. Percentage increase of longitudinal shear flow in the stress peak compared to the result obtained by the beam theory.

4 Conclusions

The main aim of the article was not to solve the problem theoretically, but to show the impact of cantilever length on horizontal shear flow at support area.

All of the results presented above refer to the beam with span of 10 m. In the parametric study also beam length of 15, 20 and 30 m were considered, therefore some general summary could be formulated.

As conclusions for composite girders it can be stated that, in the case of non-ductile shear connectors, the most affected connectors are those located about $0.5 \cdot h$ from the support. This conclusion suits quite well with the conclusions presented in [2] and [3]. The shear force, which has to be carried, is higher than the one computed according to the beam theory. The increase of this shear flow is dependant on the length of cantilever and S'/I ratio mentioned before (Fig. 7). The cantilever length of $0.3 \cdot h$ seems to be the most suitable one, because no additional lengthening leads to greater reduction of the shear peak. Therefore, shear connectors placed in the cantilever further away than $0{,}3 \cdot h \sim 0.4 \cdot h$ from the

support line seem to be ineffective. In addition, when the overhang is longer than this value, the stress peak discussed above can be neglected as well. Consequently, in the case of non-ductile connectors, the longitudinal shear force can be considered according to Fig. 8.

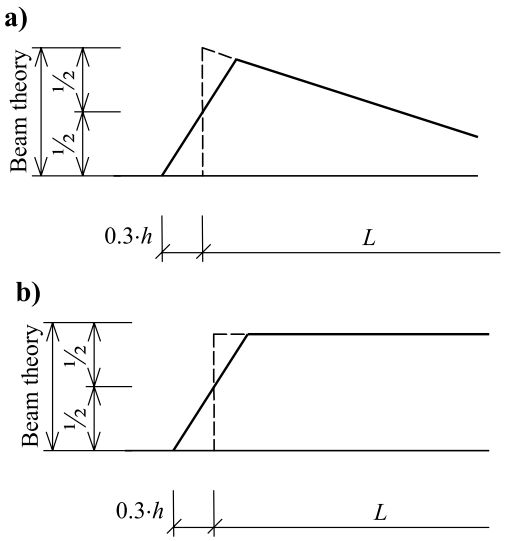

Fig. 8. Simplified shear flow distribution in support region for a beam loaded by a) the uniformly distributed load between supports and b) a force in the middle of the span

Therefore, for girders with cantilevers longer than $0.3 \cdot h$, the approach based on beam theory should be modified as follows:

- shear flow continues behind the support line and linearly decreases towards zero at a distance of $0.3 \cdot h \sim 0.35 \cdot h$;
- in the support cross-section, 50 % of the shear computed according to the simple beam theory can be considered;
- in the case of a long overhang, the shear peak can be ignored.

This simplified distribution shown in Fig. 8 can be used when determining the number and location of shear connectors in composite girders assuming that the length of overhanging cantilever is big enough. In the case when uniformly distributed load is placed not only between supports but also on cantilevers, similar distribution as in Fig. 8-a) can be adopted. If the cantilever length is not much different from the value $0.3 \cdot h$, this simplification is sufficiently accurate.

Finally, it has to be noticed that the conclusions presented above may not be valid when plastic or deformable behaviour of shear connectors is considered or expected. In this case, the shear flow is better redistributed along the girder length and behind the support, which means that a longer cantilever can be effective as well. In addition, all shear flows or connector forces discussed above were calculated without considering the effect of shrinkage in the concrete part of a composite cross-section, which means that significant forces can escape attention.

References

[1] LLOYD, H. D.: *Beams, Plates and Shells.* New York McGraw-Hill 1976. Pp. 78 – 158 .

[2] SZABÓ, B.: *Shear Force Distribution of Headed Studs of Composite Simply Supported Beams Subjected to Temperature Difference.* Proceedings of Conference "Eurosteel 99", Praha 1999. Pp. 557 – 560.

[3] SZABÓ, B. – JUTILA, A.: *Behaviour of Shear Connectors in Wood-Based Composite Girders.* Report from IABSE Conference "Innovative Wooden Structures and Bridges", Lahti 2001. Pp. 143 – 148.

Petr Štěpánek – Ivana Švaříčková *

NÁVRH KOTVENIA CFRP LAMIEL

DESIGN OF ANCHORAGE OF CFRP STRIPS

Kotvenie externe lepenej výstuže je hlavným problémom pri zosilňovaní betónových konštrukcií pomocou CFRP lamiel (Štěpánek – Šustalová 2000, 2001). Tento článok popisuje spôsob skúšok a niektoré výsledky vyplývajúce z rôznych vlastností kotevných prvkov. Výsledky skúšok sú porovnávané s hodnotami získanými matematickou analýzou správania sa kotevnej oblasti a rozdelenia napätí pozdĺž kotevnej dĺžky.

Anchorage of externally bonded reinforcement is the main problem for strengthening concrete structures with CFRP strips (Štěpánek & Šustalová 2000, 2001). This paper describes a form of the tests and some results implicating from different properties of anchorage elements. The test results are compared with values obtained from mathematical analysis of anchorage zones behavior and normal stress distribution along the anchorage length.

Keywords

Anchorage of CFRP strip, bonded reinforcement, strengthening of concrete beam, analytical solution, experimental results

1. Theoretical basis of anchorage

Brosens & Van Gemert (1999) [1] published derivation of the fundamental equations for anchoring bonded non-prestressed CFRP strips at flexural stress specimen. The main assumptions in their derivation were:

- elastic behaviour of all materials used (concrete, steel, adhesive and CFRP);
- full composite action between a bonded strip and concrete;
- strains and stresses are uniformly distributed over the entire width of a cross section of the anchorage area.

Derivation of the fundamental equations for anchoring bonded non-prestressed CFRP strips on anchorage elements (Fig. 1) was published by Štěpánek & Šustalová [2].

Static equations of equilibrium and the elementary equations of elasticity were derived based on the fundamental equations of a concrete cross section strengthened with CFRP strips as follows

$$\frac{d^2\sigma_p(x)}{dx^2} - \frac{G_a\sigma_p(x)}{t_a t_p E_p} = \frac{G_a\sigma_c(x)}{t_a t_p E_c}, \qquad (1)$$

$$\tau_p(x) = \frac{d\sigma_p(x)}{dx}\, t_a, \qquad (2)$$

where: $\sigma_p(x)$ is normal stress in CFRP strip (N/mm^2),
$\sigma_c(x)$ is normal stress in the bottom of a concrete beam (N/mm^2),
$\tau_p(x)$ is shear stress in direction of axis x in adhesive (N/mm^2),
t_a is thickness of adhesive (mm),
t_p is thickness of CFRP plate (mm),
E_p is Young's modulus of CFRP plate (N/mm^2),
E_c is Young's modulus of concrete (N/mm^2),
G_a is shear modulus of adhesive (N/mm^2).

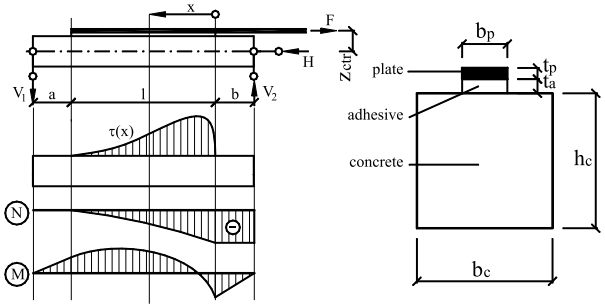

Fig. 1. Geometry details, distribution of internal forces

If we assume that

- the influence of the normal stress acting perpendicular to the concrete surface can be neglected,
- the distribution of internal forces of the tested specimen is known,

it is possible to write

$$M(x) = -F\, z_{ctr}\, \frac{x + a}{l + a + b} + b_p t_p \sigma_p(x)\, z_{ctr},$$
$$N(x) = b_p t_p \sigma_p(x). \qquad (3)$$

* **Prof. RNDr. Ing. Petr Štěpánek, CSc., Ing. Ivana Švaříčková**
Brno University of Technology, Faculty of Civil Engineering, Údolní 53, 602 00 Brno, Czech Republic,
Tel. ++420-5-41146205, 41146290, E-mail: stepanek.p@fce.vutbr.cz, svarickova.i@fce.vutbr.cz

where $M(x)$ is the bending moment and $N(x)$ is the normal force (Fig. 1).

The normal stress distribution over the concrete section is given according to Navier's law

$$\sigma_c(x) = -\frac{b_p t_p}{A_{tr}}\,\sigma_p(x)\left[z_{ctr}^2\frac{A_{tr}}{J_{tr}} - 1\right] - F\frac{z_{ctr}^2}{J_{tr}}\frac{l - x + a}{l + a + b}, \quad (4)$$

where: A_{tr} is area (mm^2) of transformed cross section (transformed factor $m_a = \frac{E_a}{E_c}$ and $m_p = \frac{E_p}{E_c}$),

I_{tr} is moment of inertia of the transformed cross section (mm^4),

z_{ctr} is the distance of the loaded concrete fibres from to the centroid of the transformed cross section (mm).

The solution of non-homogeneous differential equations (1) and (2) can be found as follows

$$\sigma_p(x) = C_1 e^{Ax} + C_2 e^{-Ax} - \frac{A_c B_2}{A^2}(l - x + a), \quad (5)$$

$$\tau(x) = t_p\left[C_1 A e^{Ax} - C_2 A e^{-Ax} - \frac{A_c B_2}{A^2}\right], \quad (6)$$

with $A^2 = A_p + A_c B_1$, $A_p = \frac{G_a}{t_a t_p E_p}$, $A_c = \frac{G_a}{t_a t_p E_c}$,

$$B_1 = -\frac{b_p t_p}{A_{tr}}\left(\frac{z_{ctr}^2}{i_{tr}^2} - 1\right),\ B_2 = F\frac{z_{ctr}^2}{J_{tr}}\frac{1}{l + a + b}$$

The constants C_1 and C_2 are found out by using appropriate boundary conditions

$$\sigma_p|_{x=0} \text{ and } \sigma_p|_{x=1} = \frac{F}{A_p} \Rightarrow$$

$$C_1 = \frac{C_2 e^{-Al} + \frac{A_c B_2}{A^2} l - \frac{A_c B_2}{A^2}(l + a)}{e^{Al}}, \quad (7)$$

$$C_2 = \frac{-\left(\frac{F}{b_p t_p} - \frac{A_c B_2}{A^2}(a + l)\right)\cdot e^{Al} - \frac{A_c B_2}{A^2}(a + l)}{e^{Al} - e^{-Al}}.$$

The maximum shear stress is at the end of the plate

$$\tau_{max} = t_p\left(AC_1 - AC_2 - \frac{A_c B_2}{A}\right). \quad (8)$$

Fig. 2a shows the distribution of the normal stresses $\sigma_p(x)$, $\sigma_c(x)$ and the shear stress $\tau_p(x)$ along the x axis. In this solved example, the influence of anchorage by a distance of 35 mm from the end of plate can be neglected. The design details and material characteristics are: a beam 150 × 150 × 600 mm, strip SIKA CarboDur S512, E_c = 27 GPa, E_p = 155 GPa, G_a = 5,33 GPa. The scheme of loading is shown in Figure 1. Figure 2b shows the internal forces (normal force $N(x)$ and bending moment $M(x)$) in the concrete block along the x-axis.

The differential equation describing normal stress $\sigma_n(x)$ in the perpendicular direction to the lower surface of a concrete beam is given by

$$\frac{d^4\sigma_n(x)}{dx^4} + \frac{E_a b_p}{t_a E_p t_p}\sigma_n(x) = 0. \quad (9)$$

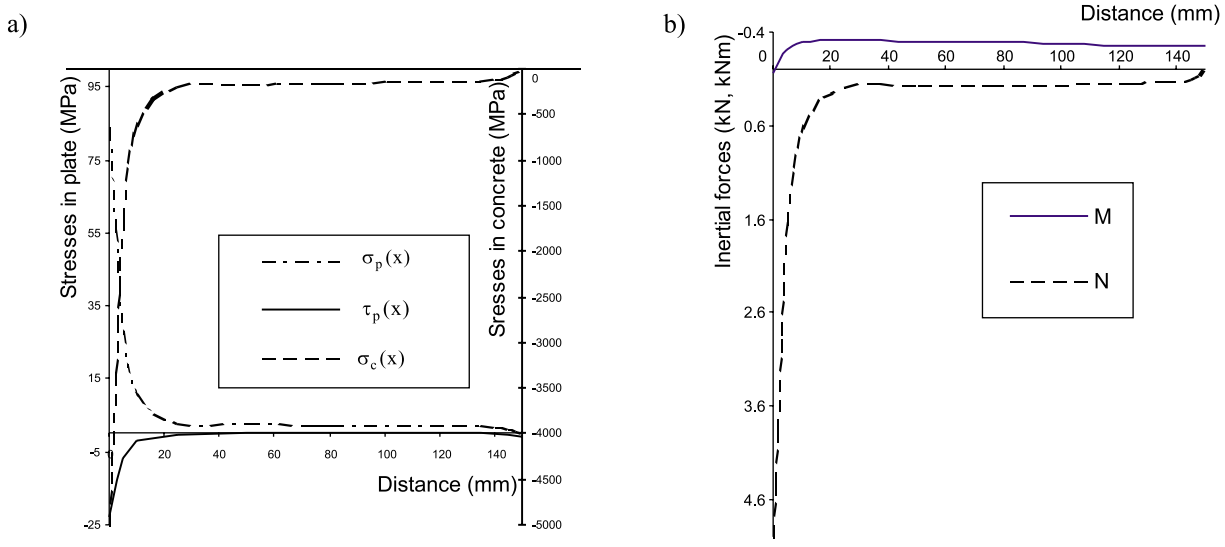

Fig. 2 Results of analytical solution of anchorage problem a) Stresses distribution along the anchorage zone $\sigma_p(x)$, $\tau_p(x)$, $\sigma_c(x)$ b) Dependence of internal forces in the concrete specimen on distance x

The solution of eq. (9) can be found as follows

$$\sigma_n(x) = e^{-\beta x}[D_1\cos(\beta x) + D_2\sin(\beta x)] \qquad (10)$$

with $\beta = \sqrt[4]{\dfrac{E_a b_p}{4 t_a E_p I_p}}$.

The constants D_1, D_2 can be determined by using the proper boundary conditions:

$$\frac{d^2\sigma_n(x)}{dx^2} = \frac{E_a M_p(x)}{t_a E_p I_p} - \frac{E_a M_c(x)}{t_a E_c I_c}. \qquad (11)$$

Then D_1 and D_2 can be calculated

$$D1 = \frac{\left[\dfrac{E_a}{t_a 2\beta^2 e^{-\beta l}}\left(\dfrac{M_p}{E_p I_p} - \dfrac{M_c}{E_c I_c}\right) + D_2\cos(\beta l)\right]}{\sin(\beta l)}, \qquad (12)$$

$$D_2 = -\frac{E_a V_1 a}{t_a 2\beta^2 E_c I_c}. \qquad (13)$$

The distribution of the normal stress $\sigma_n(x)$ along the x-axis obtained from analytical solution for the identical example solved before is shown in Fig. 3.

2. Tests of anchorage blocks

Anchorage blocks of dimension 150/150/600 mm were prepared from concrete of class B15-B25 according to the Czech standard ČSN 73 1201 (1986). The producer and sponsor of the research work were Prefa Topos Tovačov and SIKA CZ.

The physical and mechanical properties of concrete specimens (Young modulus, tensile and stress strength) were determined by non-destructive methods before the beginning of the tests. The CFRP strips of a cross-sectional dimension 50/1.2 mm and Young's modulus 155 GPa was bonded to the prepared surface of different anchorage lengths – 150, 225 to 300 mm (see Fig. 4).

The aim of the tests was to determine the influence of anchorage length and size of the cross force (acting on the anchorage zone) on the ultimate axis force of the strip. The resistance tensionmeters were glued to the strips, the deformation along the length of anchorage was measured with a videoextensionmeter. The scheme

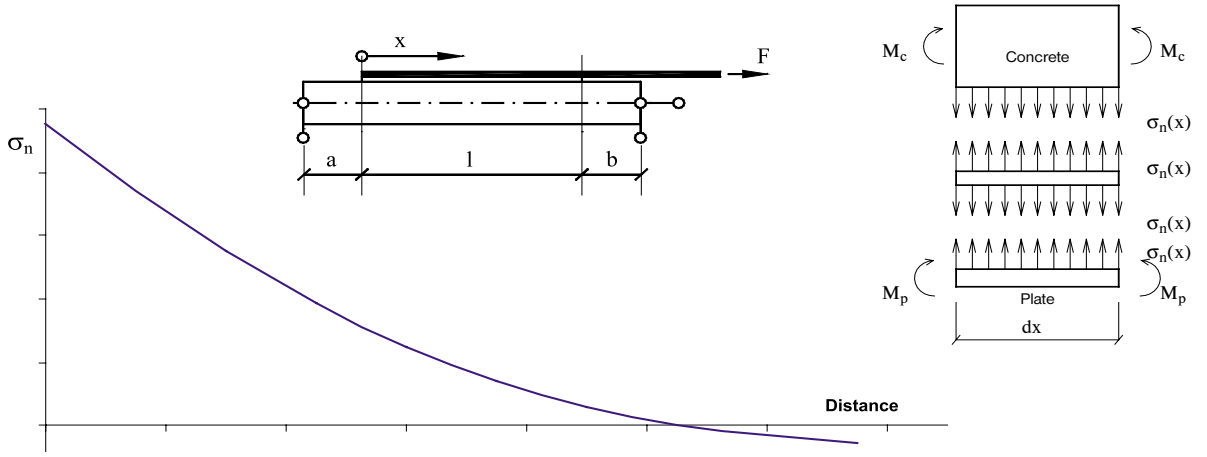

Fig. 3 Stress distribution along the anchorage zone $\sigma_n(x)$

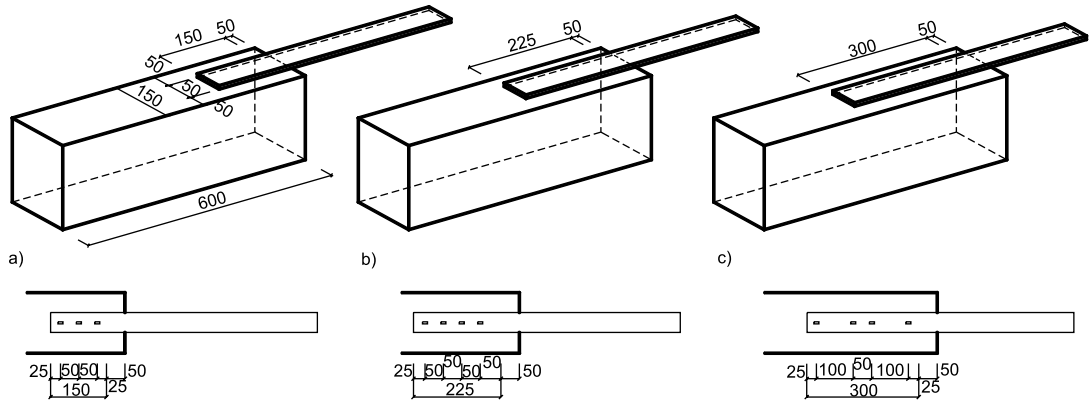

Fig. 4. The elevation of the anchorage zones of the specimen with strain gauges

of the anchorage zones and position of the measuring points are shown in Fig. 4.

Arrangement of the test (the test set-up and applied apparatus) is shown in Fig. 5. Fig. 5a represents anchoring without stirrup (without acting cross force on the anchorage area), Fig. 5b demonstrates anchoring with stirrup without prestressing and Fig. 5c illustrates anchoring with prestressed stirrups.

The results of the test without cross force acting on the bonded strip (alternative according Fig. 5a anchoring without stirrup) and with variable cross force acting of the glued length 150 mm (anchoring with stirrup – see Fig. 5b,c) is shown in Fig. 6.

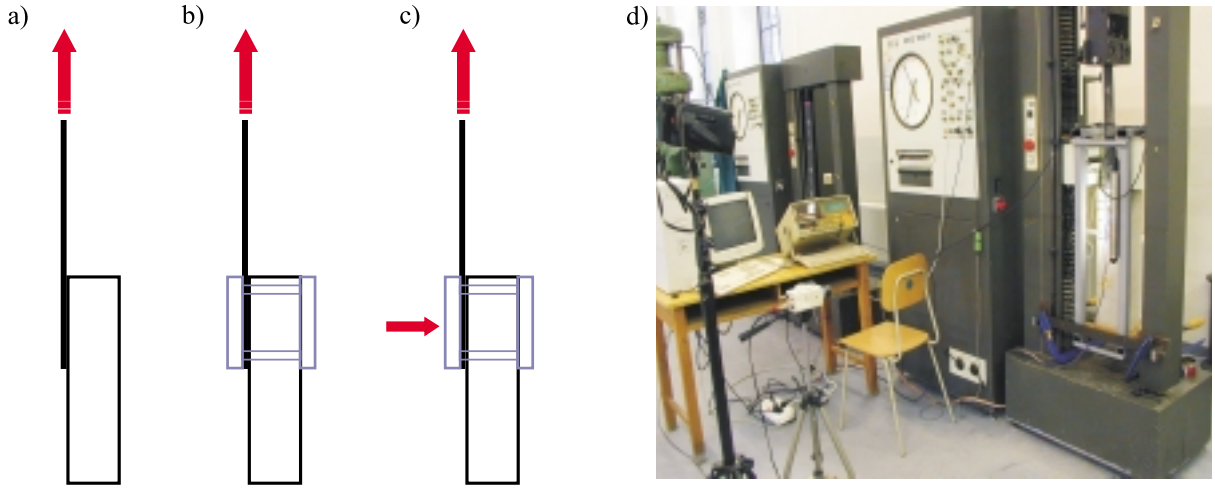

Fig. 5. The loading process and testing equipment
a, b, c) Scheme of tested alternatives of anchoring, d) Arrangement of test

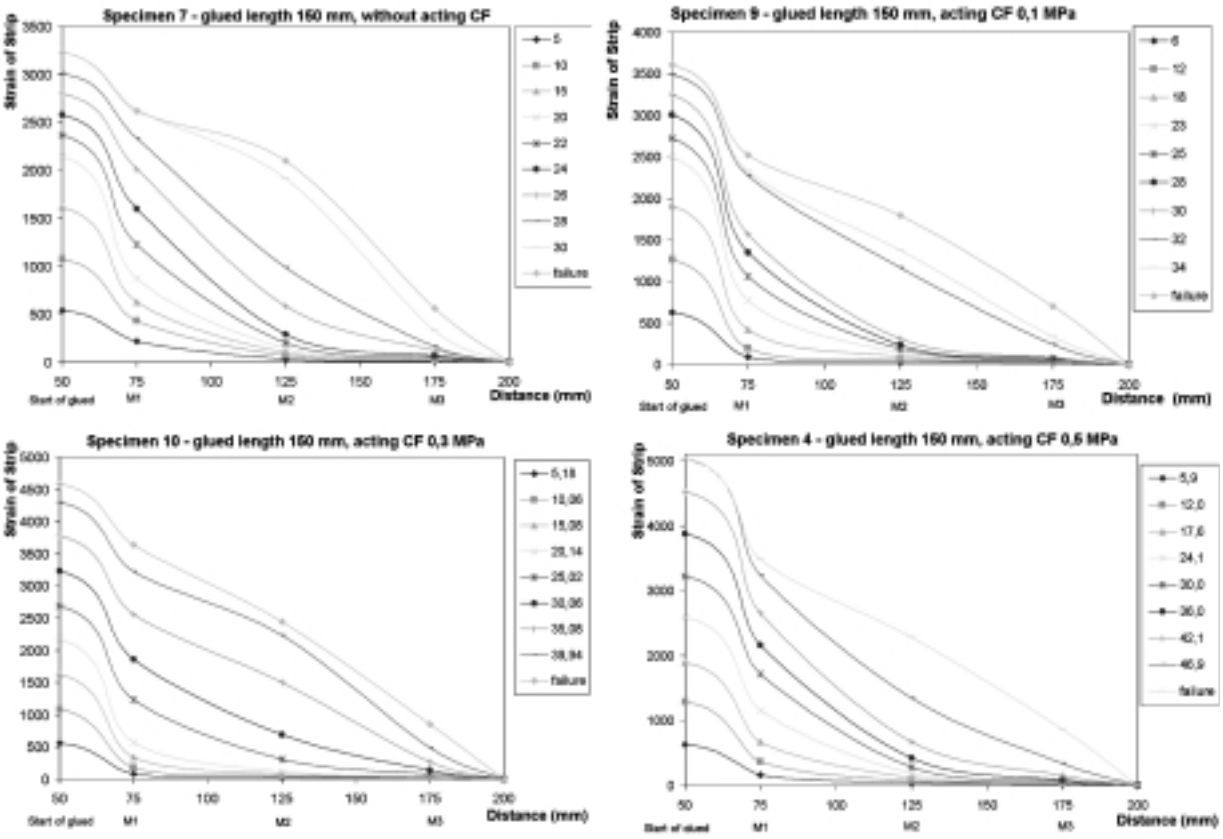

Fig. 6. Strain of CFRP strip with anchorage length 150 mm

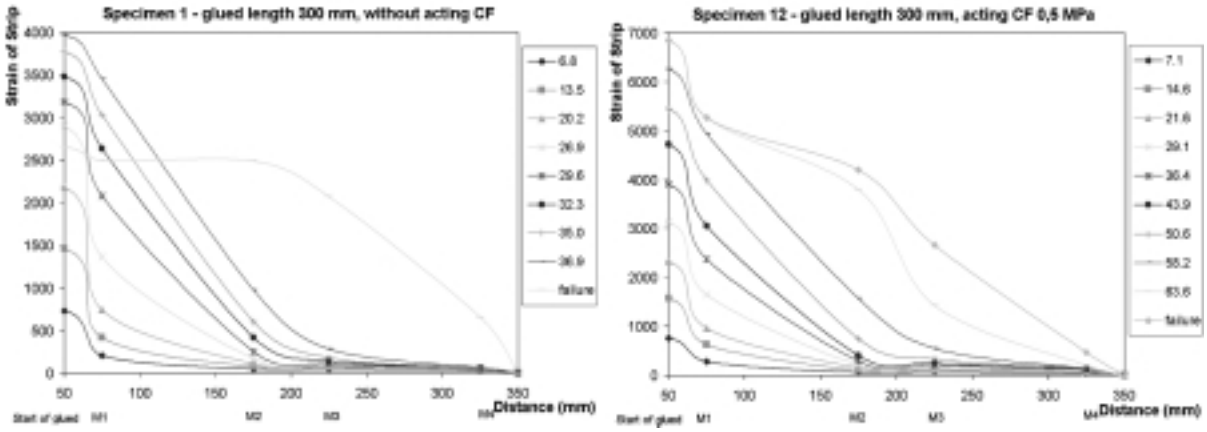

Fig. 7. Strain of CFRP strip with anchorage length 300 mm

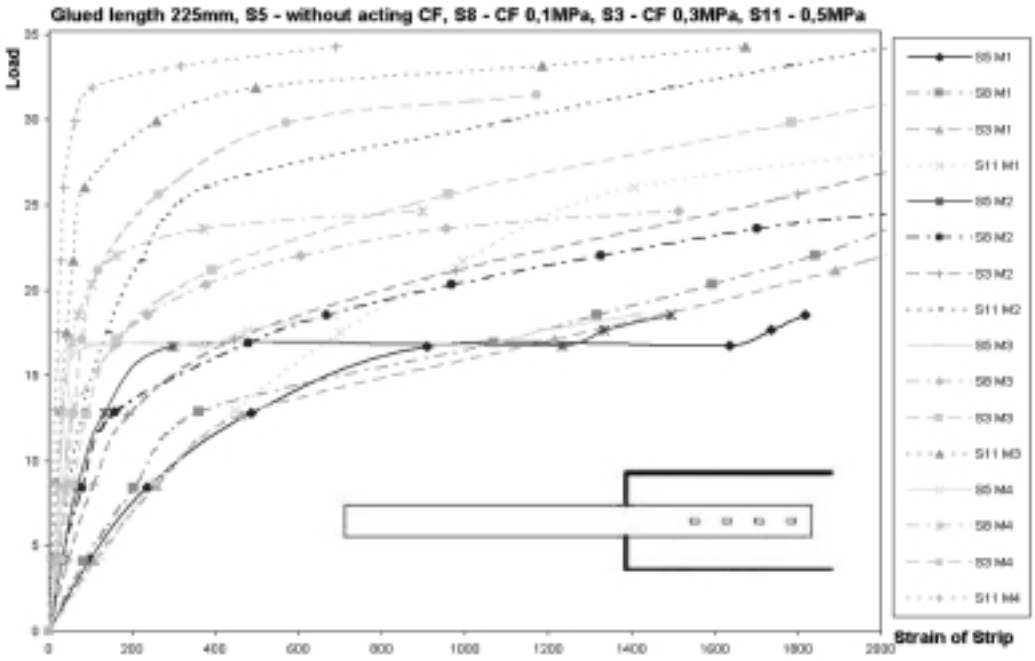

Fig. 8. Strain measured through resistance tensionmeter (M1, M2, M3, M4)

The actual length of the anchorage is in this case smaller than the necessary anchorage length. With a higher length of the anchorage it is possible to achieve a higher axial force in the strip (see Fig. 7).

Fig. 8 shows strain rise of CFRP strip at measuring points throughout the whole course loading on the specimens with glued length of 225 mm.

Comparison of the strip strain between analytical results and experimental tests at small tension normal force of the strip for the bonded length 150 mm is shown in Fig. 9.

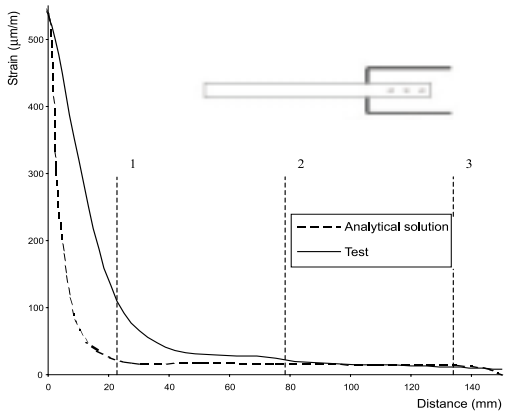

Fig. 9. Strain of CFRP strip along the x axis

3. Conclusions

The comparison of the theoretical and measured results of stress and strain at the anchorage areas demonstrates a good accordance at the linear area of behaviour. The theoretically derived design equations can be used for anchorage of non-prestressed and prestressed CFRP strips.

Acknowledgement

This contribution was prepared within the scientific-research work of the Project FAST VUT in Brno, CEZ 322/98 "Theory, Reliability and Damage of Statically and Dynamically Loaded Structures" and Czech Grant Agency GAČR 103/02/0749 "Modern Methods of Strengthening Concrete and Masonry Structures and Optimization of Design".

References

[1] BROSENS, K., VAN GEMERT, D.: (1999). *Anchoring stresses in the end zones of externally bonded bending reinforcement.* 5. Internationales Kolloquium Freiburg, MSR '99, ISBN 1163-1174, 1029 – 1035

[2] ŠTĚPÁNEK, P. and ŠUSTALOVÁ, I.: (2001). *Problematika chování kotevních oblastí železobetonových prvků zesílených CFRP lamelami.* Stavebné materiály a skúšobnictvo, Štrbské pleso, Slovenská republika, září 2001, ISBN 80-7099-677-3

[3] ŠTĚPÁNEK, P. and ŠUSTALOVÁ, I.: (2001). *Anchoring of non-prestressed and prestressed CFRP Strips at Strengthening of concrete beams.* Proccedings of the international conference Composites in Material and Structural Engineering. Klokner Institute, Prague, Czech Republic, June 2001

Jacek Śliwiński – Witold Brylicki *

NÁVRH TUHÝCH BETÓNOVÝCH ZMESÍ ZHUTNENÝCH VIBROLISOVANÍM

MIX DESIGN OF STIFF CONCRETE MIXTURES COMPACTED BY VIBRATION UNDER A SURCHARGE LOAD

V technológii výroby produktov zhutnených vibrolisovaním, ako dlažobné tvarovky, je potrebné použiť betónové zmesi s konzistenciou mimo rozsahu navrhnutého pre obyčajný betón. Aby došlo k súčasnému účinku vibrácie a statického zaťaženia, betónová zmes musí splniť špeciálne požiadavky na konzistenciu a spracovateľnosť. Článok uvádza dve metódy návrhu betónovej zmesi, ktoré sa ukázali ako čiastočne použiteľné pre zmesi zhutnené vibrolisovaním. Jedna z nich je založená na vyplnení medzier medzi zrnami kameniva cementovým tmelom, druhá na obalení zŕn plniva cementovým tmelom.

In the manufacture technology of products compacted by vibration under a surcharge load, such as paving blocks, it is necessary to use concrete mixtures of consistency outside the range designed for ordinary concrete. Due to the simultaneous effect of vibration and static load the concrete mixture must meet special requirements of consistency and workability. The paper presents two methods of concrete mix design which proved particularly useful for mixtures compacted by vibration under a surcharge load. The former is based on heaping up the aggregate void spaces with cement paste, the latter on coating the aggregate grains with paste.

1. Introduction

In the last decade the interest in concrete products manufactured by vibration under a surcharge load, such as paving blocks, kerbs, etc, has increased significantly. In the compaction by vibration under a surcharge load the mixture is subjected to the dynamic effect of vibration and static surcharge load. This combined effect Z must overcome the internal resistance of the mixture W, which is made up of frictional, viscosity and cohesion resistance. As a result the mixture volume V decreases and its apparent density ρ increases.

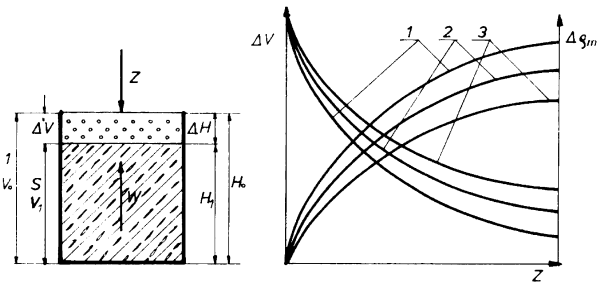

Fig. 1. Changes of volume ΔV and apparent density $\Delta\rho$ of mixture under loads Z

The method of vibration under a surcharge load is a combined method which does not cause a change of the W/C ratio during compaction. The frictional and viscosity resistance is overcome mainly by the effect of vibration, that is applying a multiplied force of gravity. Due to vibration the concrete mixture behaves like a dense, tixotropic fluid and the internal friction decreases. The effect of pressure exerted on the mixture enhances the process of compaction. What is important in this technology is the proportion of the two effects. The most favourable proportion of contribution of the two effects differs for different mix composition (different aggregate grading, different cement paste content, different W/C ratio, different consistency).

The technology of vibration under a surcharge load, described briefly below, requires a particularly careful selection of mix composition which ensures both the concrete assumed strength and proper consistency and workability.

2. Description of two useful methods of concrete mix compacted by vibration under a surcharge load

The methods that have recently proved very useful in concrete mix design for the technology of surcharge vibration are: the method of heaping up the aggregate void spaces with cement paste and the method of coating the aggregate grains. In Poland these methods have been known for years as the Kopyciński method and the Paszkowski method [2].

* [1]Prof. Jacek Śliwiński D.Sc. Ph.D., [2]Witold Brylicki D.Sc.
[1]Cracow University of Technology, Faculty of Civil Engineering, Warszawska 24, 31-155 Kraków, Poland, E-mail: jsliwins@imikb.wil.pk.edu.pl
[2]University of Mining and Metallurgy, Faculty of Materials Science and Ceramics, Mickiewicza 30, 30-059 Kraków, Poland

In Germany the method based on heaping up the aggregate void spaces with paste was proposed by Zipelius [3] in the 1960s. The method was later used to construct the so-called Econom apparatus [4], due to which it is possible to empirically define the most economical paste content in concrete mix. The empirical design of concrete mix by means of the Econom apparatus takes into account the real conditions of compacting by surcharge vibration, that is, the characteristics of vibration and surcharge pressure are taken into account.

The other method is based on the determination of indispensable quantity of cement paste as a function of aggregate surface area and thickness of paste layer coating its grains.

2.1 Method of heaping up aggregate void spaces with cement paste Econom apparatus method [4]

The method is based on the assumption that in order to make a concrete mixture from the adopted aggregate, the void spaces between the grains have to be heaped up, to some indispensable degree, with cement paste (Fig. 3).

Before we start the empirical design it is obviously necessary to select both the type and class of cement and W/C ratio as well. The value of W/C ratio can be defined from any dependence between concrete strength and its composition, for example from Bolomey's formula. It is also necessary to decide on the aggregate type and design its grading such that the grading curve was within the regions shown in Fig. 2 [5].

Initially we determine the volume of a set portion of aggregate $V_{aggr.}$ [dm^3] (in the Econom apparatus method portion of 10 kg is used) compacted in conditions similar to those of the mixture to be compacted (vibration under surcharge load). The next step is to determine the volume of voids in the aggregate. It can be done easily by infusion of water in the amount of V_{water} [dm^3] to the aggregate compacted in proper conditions so that the water fills all the void spaces between the aggregate grains. Thus the infused water volume V_{water} is equal to the volume of the voids in the tested portion of aggregate V_{av} (Fig. 3a).

The next step is to prepare the cement paste of a certain W/C ratio, its volume V_{paste} equal to water volume V_{water} (equal to the volume of voids V_{av}) is mixed with 10 kg of aggregate identical as before. The concrete mix obtained in this way is compacted in identical conditions as the dry aggregate was compacted initially. Its volume after compaction $V_{concrete\ mix}$ [dm^3] is determined. This volume will be slightly larger than the volume of compacted dry aggregate $V_{aggr.}$ because the aggregate grains will be coated with a thin layer of the paste and will be separated (Fig. 3b). The difference between the volume of the mix composed in this way and the volume of the dry aggregate itself ($\Delta V = V_{concrete\ mix} - V_{aggr.}$) is the volume of void spaces in the prepared mix. It is this value by which the volume of cement paste should be enlarged to obtain a mix with no pores. The final indispensable volume of paste is thus $V_{paste\ def.} = V_{paste} + \Delta V$ (Fig. 3c).

Next, knowing the $W/C = \omega$ characterising the paste, we can calculate its density ρ_{paste} which is:

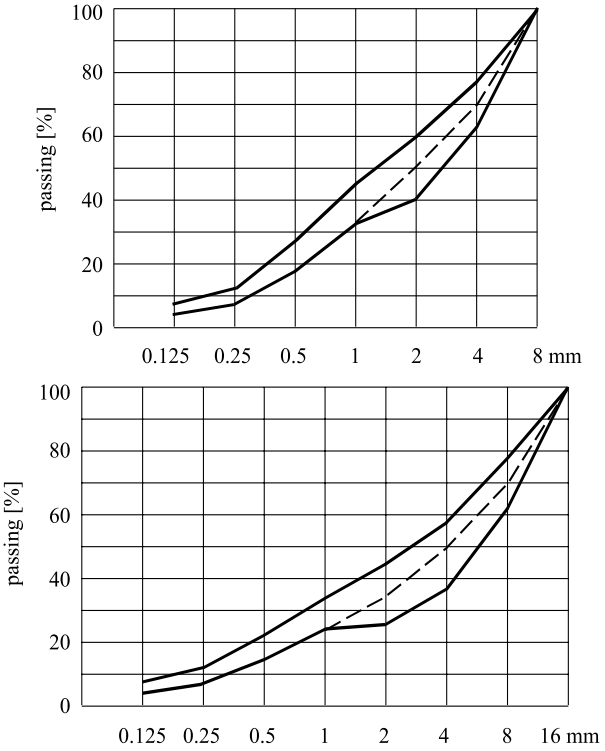

Fig. 2. Approximate areas of good grading of aggregates 0/8 mm and 0/16 mm for concretes compacted by vibration under a surcharge load [5] (the area between upper and lower broken curve - for rounded aggregate, the area between the upper and lower solid curve - for crushed aggregate).

$$\rho_{paste} = \frac{\omega + 1}{\omega + \frac{1}{\rho_c}} \quad [\text{kg/dm}^3] \tag{1}$$

where: ρ_c - cement density, commonly adopted as 3.1 [kg/dm^3]

Knowing that the mass of paste of volume $V_{paste\ def.}$ is:

$$m_{paste\ def.} = V_{paste\ def.}\ \rho_{paste} \quad [\text{kg}] \tag{2}$$

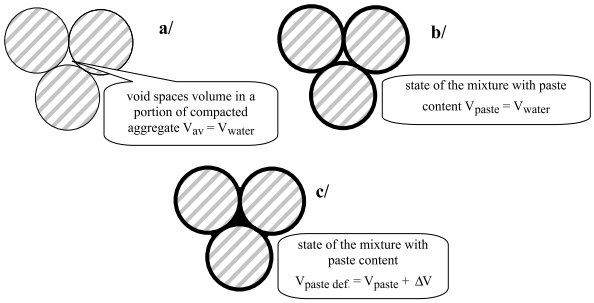

Fig. 3. The idea of heaping up the aggregate with paste; the Econom apparatus version (description in the text)

the content of cement C' and water W' in concrete mix containing aggregate quantity A = 10 kg can be calculated from formulae:

$$C = \frac{m_{paste\ def.}}{1 + \omega} \quad [\text{kg}] \tag{3}$$

$$W = m_{paste\ def.} - C \quad [\text{kg}] \tag{4}$$

Since from the quantities of components given above we have obtained the compacted concrete mix of the volume $V_{concrete\ mix}$, the composition of 1 m^3 of the mix is:

$$C = \frac{C'}{Vconcrete\ mix}\,1000 \quad [\text{kg/m}^3] \tag{5}$$

$$W = \frac{W'}{Vconcrete\ mix}\,1000 \quad [\text{kg/m}^3] \tag{6}$$

$$A = \frac{10}{Vconcrete\ mix}\,1000 \quad [\text{kg/m}^3] \tag{7}$$

Despite the fact that the mix composition was designed empirically, it is necessary to verify it additionally in production conditions. This refers to both the correct consistency and workability in the compacting conditions on a real surcharge vibration machine.

2.2 Method of coating aggregate grains with paste

As in any design method, also in our case it is necessary to start with the assumptions as to the quantitative selection of ingredients, i.e. type and class of cement and aggregate grading as well as the value of W/C ratio that ensures the proper strength of concrete.

In the presented method the calculations are based on the aggregate surface area $F_{aggr.}$, i.e. the total surface of aggregate grains of 1 kg mass. Since aggregate is a mixture of grains of various sieve size f_i, its surface area can be calculated as a weighted average of the surfaces F_{ai} of all the sieve sizes found in it:

$$F_{aggr.} = \frac{\sum_{i=1}^{i=n} F_{ai} f_i}{100} \quad [\text{dm}^2/\text{kg}] \tag{8}$$

where: F_{ai} – the surface of i-th sieve size [dm^2/kg],
f_i – the content of i-th sieve size [% mass]

The values of surface areas of particular size of grains of rounded aggregate nearly spherical in shape and density $\rho_a = 2.65$ kg/dm^3 have been presented in Table 1.

When crushed aggregate is used, the values in Table 1 should be multiplied by 1.15. For aggregate from material of density $\rho_a \neq 2.65$ kg/dm^3 the values in Table 1 should be additionally multiplied by quotient $\rho_a/2.65$.

When the surface area of the aggregate used $F_{aggr.}$ is known, it is possible to calculate the paste demand for 1 kg of aggregate $v_{paste/1\ kg}$:

$$v_{paste/1\ kg} = F_a\, t \quad [\text{dm3/kg}] \tag{9}$$

Specific surface of grains of various sieve size of rounded aggregate with density $\rho_a = 2.65$ kg/dm^3 — Table 1

Sieve size f_i [mm]	Specific surface F_{ai} [dm^2/kg]	Sieve size f_i [mm]	Specific surface F_{ai} [dm^2/kg]
0/0.125	≈ 4000	2/4	100
0.125/0.25	1600	4/8	50
0,25/0.5	800	8/16	35
0.5/1	400	16/31.5	12.5
1/2	200	31.5/63	6.2

where: t – required thickness of paste layer coating the aggregate grains [dm], after [3] to obtain the consistency proper for compacting by vibration under a surcharge load the values of t are:

for $W/C = 0.8 \rightarrow t = 0.0004$ dm (0.04 mm),
$W/C = 0.6 \rightarrow t = 0.0005$ dm,
$W/C = 0.4 \rightarrow t = 0.0006$ dm

The thickness values of the paste layer coating the grains have been selected in such a way that the necessity of heaping up the voids between the grains has been taken into account.

The total volume of 1 kg of aggregate and quantity of paste necessary for its grain coating is:

$$v_1 = \frac{1}{\rho_a} + v_{paste/1\ kg} \quad [\text{dm}^3] \tag{10}$$

while the necessary paste volume in 1 m^3 of the mix is:

$$V_{paste} = \frac{1000}{v_1}\, v_{paste/1\ kg} \quad [\text{dm}^3/\text{m}^3] \tag{11}$$

It should be noted that the $1000/v_1$ quotient gives the necessary quantity of aggregate A in 1 m^3 of concrete mix.

In the following sequence of a set of equations:

$$\frac{W}{C} = \omega \tag{12}$$

$$W + \frac{C}{\rho_c} = V_{paste} \tag{13}$$

cement and water content in 1 m^3 of the mix can be calculated:

$$C = \frac{V_{paste}\rho_c}{\rho_c\,\omega + 1} \quad [\text{kg/m}^3] \tag{14}$$

$$W = \omega C \quad [\text{kg/m}^3] \tag{15}$$

The aggregate content, as mentioned above, is calculated as:

$$A = \frac{1000}{v_1} \quad [\text{kg/m}^3] \tag{16}$$

or from the volume balance:

$$A = (1000 - V_{paste})\rho_a \quad [\text{kg/m}^3] \tag{17}$$

Similarly as in the first method, the final step is empirical verification of the designed concrete mix in which the compaction process and properties of hardened concrete in product are checked.

3. Additional remarks

The technology of concrete products manufacture by vibration under a surcharge load makes the designer of concrete mix face many specific requirements. Besides the obvious necessity to obtain concrete of assumed technical properties, these requirements include proper consistency and workability of concrete mixture. Even minor changes in mix composition can make it useless in product manufacture by this method. The two presented methods of concrete mix design, used for ordinary concretes for a long time, have proved very useful also in the design of concretes vibrated under a surcharge load.

References

[1] MIKOŚ, J.: *Wybrane zagadnienia prefabrykacji,* PWN, Warszawa 1987.
[2] ŚLIWIŃSKI, J.: *Beton zwykły, projektowanie i podstawowe właściwości,* wyd. Polski Cement Kraków, 1999.
[3] ZIPELIUS, R.: *Zementleimermittlung fűr beliebige Zuschlagstoffgemische;* Empirische Methode fűr hochfesten Beton grősster Wirtchaftlichkeit; Betonsteinzeitung 33, 1967, H.5; Bauverlag GmbH, Wiesbaden.
[4] DRINKGERN, G.: *Abweichungen von der "klassischen" Mischungsberechnung fűr Beton,* Betonwerk+Fertigteil-Technik, H.11/1994, 45-57
[5] BRYLICKI, W.: *Zasady kształtowania jakości betonów wibroprasowanych,* Materiały Sympozjum Naukowo-Technicznego, Technologia produkcji i badania właściwości betonowej kostki brukowej, kwiecień 1999, 39-61.

Stefania Grzeszczyk – Grzegorz Lipowski *

VPLYV DRUHU POPOLČEKA A CEMENTU NA REOLÓGIU CEMENTOVEJ KAŠE

EFFECT OF THE FLY ASH AND CEMENT TYPE UPON THE CEMENT PASTE RHEOLOGY

V článku je uvedená analýza vplyvu dvoch druhov popolčeka na reologické vlastnosti cementovo-popolčekových zmesí za použitia cementov s rozličným množstvom C_3A. Bol zistený významný vplyv druhu popolčeka a cementu na reologické vlastnosti cementovo-popolčekových zmesí.

In the paper an analysis of the the influence two types of fly ashes on rheological properties of cement pastes with cements containing different amount of C_3A is presented. It was stated that a type of fly ash and content of C_3A in cement have significant influence upon rhelogical behaviour of cement pastes.

1. Introduction

Fly ashes (pulverised fuel ashes – pfa) are waste materials produced as a result of coal combustion. In this process the pulverised coal is fed to the combustion chamber and burnt at high temperature. The incombustible mineral substances are then subjected to the phase and chemical transformations. Over 80 wt. % of this material is transported with the flue gas and collected in electrical or mechanical precipitators. The residue is deposited as a bottom ash in a furnace.

Fly ashes are composed mainly of glass with some amount of crystalline phases. An unburned coal residue can be also present. The type and properties of fly ash are affected by the following factors [1], [2]:
- type of coal (anthracitic, black, bituminous, subbituminous, brown),
- fineness of coal before combustion,
- type of furnace, temperature and other conditions of the process,
- method of flue gas de-dusting,
- transport and storage of fly ash.

There are many of fly ash classification systems. According to the ASTM C 618 89 [3] the high calcium class C fly ashes and low calcium class F ones can be distinguished. This classification is based on the total $SiO_2 + Al_2O_3 + Fe_2O_3$ as well as CaO content.

It is generally known that the fly ashes from the black coal combustion exhibit low CaO content while those originating from the brown coal are the high calcium materials, with CaO content attaining 40 wt. % [4].

The fly ash particles are composed of glass and crystalline phases. The glass content is usually about 80 % by mass, in some cases attains 90 %. In the high calcium fly ash it is low, about 60 % by mass. In the low calcium fly ash the following crystalline phases can be present: quartz (SiO_2), mullite ($3Al_2O_3 \cdot 2SiO_2$), magnetite Fe_3O_4) and haematite (Fe_2O_3). On the surface of low calcium fly ashes, a film of metallic iron is often observed on the magnetite or haematite crystals.

In the high-calcium fly ash, apart from the phases mentioned above, the following ones can be found: calcium silicates and aluminates ($2CaO \cdot SiO_2$, $CaO \cdot Al_2O_3$, $5CaO \cdot Al_2O_3$), calcium aluminosilicates ($2CaO \cdot Al_2O3 \cdot SiO_2$) and calcium sulphates ($CaSO_4$, $CaSO_4 \cdot 2H_2O$), calcium ferrites ($2CaO \cdot Fe_2O_3$), calcium oxide (CaO and periclase (MgO)).

The hydration of fly ash should be considered separately for the low and high-calcium materials, because of the substantial difference in chemical and mineral composition [5], [6], [7]. Reactions occurring between cement and fly ashes in an early stage of hydration influence the rheological properties of cement pastes. The hydration of cement with fly ashes is a complex process because of the mutual interactions between the hydrating cement and fly ash components. Introduction to cement higher amounts of the fly ashes (also high-calcium fly ashes) require investigation of their impacts on the rheological properties of cement pastes dependent on their type and type of cement [8], [9], [10].

* **Prof. Stefania Grzeszczyk, Dr. Ing. Grzegorz Lipowski**
Department of Building Materials Engineering, Faculty of Civil Engineering, Technical University of Opole, ul. Katowicka 48, 45-061 Opole, Poland,
Tel. ++48-77-4536645, E-mail stf@po.opole.pl

2. Experimental

2.1. Materials

The portland cements with differed content of C_3A (7,6 and 3,8 % wt.) and similar Blain's specific surface ~ 340 m^2/kg were used. The high-calcium fly ashes from the brown coal combustion and low-calcium fly ashes also with similar Blain's specific surface ~ 320 m^2/kg were taken. The chemical composition of the cements and fly ashes used in experiments is given in Table 1 phase composition of cement is presented in Table 2.

Chemical composition of cements and fly ashes. Table 1

Component composition	Cement I	Cement II	Fly ash I Low-calcium	Fly ash II High-calcium
	Content in % wt.			
Loss on ignition	0.8	0.6	1.0	1.9
SiO_2	22.7	20.1	50.4	30.0
Fe_2O_3	3.0	5.0	8.6	6.0
Al_2O_3	4.6	2.8	26.8	18.0
CaO	66.5	69.2	4.3	30.1
MgO	1.4	1.0	2.6	2.1
SO_3	0.6	0.5	1.2	10.8
Na_2O	0.2	0.1	1.6	0.2
K_2O	0.7	0.2	1.4	0.2
CaO free	0.8	0.5	0.2	3.0

Mineralogical composition of cements. Table 2

Phase composition	Cement I	Cement II
	Content in % wt.	
C_3S	64.7	73.2
C_2S	17.0	12.0
C_3A	7.6	3.8
C_4AF	7.8	11.0

The phase composition of fly ashes was characterized by XRD. The following crystalline phases have been detected: quartz, mulite in fly ash I and in fly ash II together also free CaO, anhydrite, calcium sulphate dihydrate – gypsum, hematite and gehlenite in fly ash II.

The cement - fly ash mixtures used in the rheological investigations were prepared and homogenised in a laboratory mill. The fly ash content in cement was 20%, 40%, 60% and 80% wt.

2.2. Rheological measurements

The rheological measurements were carried out using the rotative viscosimeter type Rheotest RV – 2.1, with the modified surfaces of both cylinders. The rheological properties of pastes with fly ashes were determined from the flow curves, at growing and reduced rates of shearing in the range from 0 to 146 s^{-1}. The yield value and plastic viscosity were determined from the descending part of the flow curve, according to the Bingham's model.

3. Results and discussion

Figures 1 and 2 show examples of the obtained flow curves for cement-fly ashpastes with low content of C_3A in cement, Table 3 presents calculated yield values τ_0 and plastic viscosities η_{pl} cement-fly ash pastes.

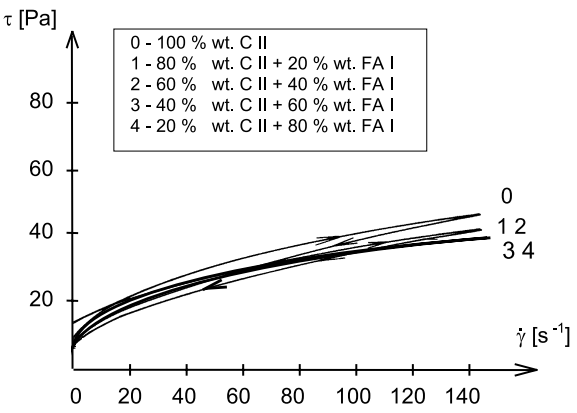

Fig. 1. Flow curves of cement pastes with cement (C II) containing 3.8 % wt. C_3A and addition of low-calcium fly ashes (FA I).

The results obtained shown that the addition of low-calcium fly ashes (FA I) to high content C_3A cement (C I), demonstrated by big yield values and plastic viscosity, resulted in significant

Rheological parameters τ_0 [Pa] and μ_{pl} [Pa · s]. Table 3

No.	Sample composition in % wt.	C I FA I		C II FA I		C I FA II		C II FA II	
		τ_0	η_{pl}	τ_0	η_{pl}	τ_0	η_{pl}	τ_0	η_{pl}
0	100%C+0%FA	69.1	0.83	9.9	0.28	69.1	0.83	9.9	0.28
1	80%C+20%FA	30.0	0.45	8.9	0.28	65.5	0.92	9.9	0.34
2	60%C+40%FA	25.1	0.43	9.7	0.29	68.4	0.99	14.5	0.52
3	40%C+60%FA	16.3	0.39	8.6	0.29	–	–	20.8	0.96
4	20%C+80%FA	13.1	0.33	9.1	0.27	–	–	–	–

improvement of rheological properties of cement pastes. A decrease of yield values and plastic viscosities with increasing fly ash content in cement is illustrated in Tab 3. The biggest improvement occurred (two times slope in plastic viscosity and yield value) with addition of 20 % of fly ashes in cement. A further growth of percentage of fly ashes in cement doesn't result in fluidity of cement pastes.

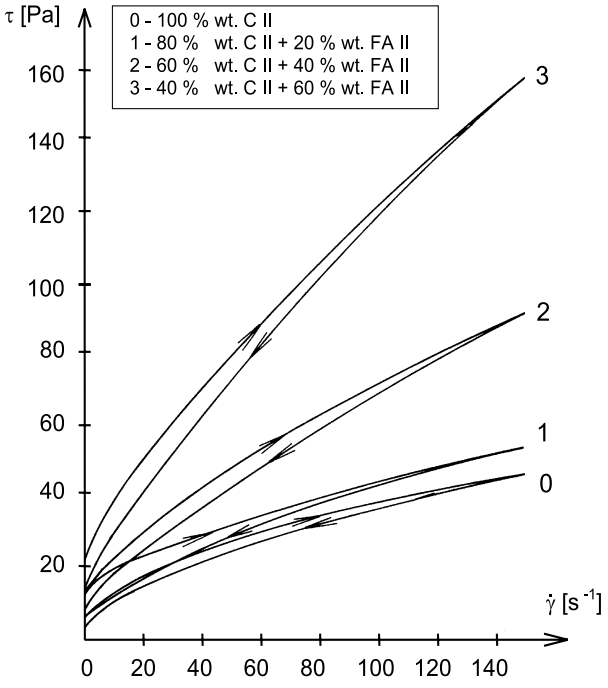

Fig. 2. Flow curves of cement pastes with cement (C II) containing 3.8 % wt. C_3A and addition of high-calcium fly ashes (FA II).

The addition of low-calcium fly ashes (FA I) in the mixtures with low amount of C_3A phase (C II), good fluidizated by calcium sulphur, results in insignificant changes of rheological properties Fig 1. Cement II paste with low amount C_3A phase (3,8 % wt.) is better fluidited than cement I pastes (C I) 7.6 % wt. of C_3A. The yield value of pure cement paste with cement (C II) is a few times lower compared to the pure cement paste with cement (C I), this is also observed for plastic viscosity.

In case of high-calcium fly ashe from lignite coal combustion its unfavourable influence on rheological properties is significantly lower for cement (C II) with lower content of C_3A phase (Fig. 2). It was stated that rhelogical measurement is impossible to carry out when the addition of fly ashes exceeds 40 % wt. in cement (C II), but for cement (C I) measurements were possible with 60 % wt. fly ashes content in cement.

4. Conclusions

- Generally, content of low-calcium fly ash in cement-fly ash mixture results in an increase of the cement paste fluidity, on the contrary to the high-calcium ash when the addition results in decrease of the fluidity for both type of cement.
- An increase fluidity cement paste effect developed by the addition of low-calcium fly ash depends on C_3A phase content in cement. In case of cement paste with low C_3A amount good fluidizated by calcium sulphur, influence of fly ashes on rheological properties is insignificant. A considerable increase of fluidity is observed in cement pastes reaches in C_3A which are characterized in low fluidity comparing to cement pastes poor in C_3A.
- Unfavourable impact of high-calcium fly ash in cement pastes on rheological properties of cement pastes occurs in a lower degree for cement pastes with low content of C_3A.

References

[1] ALONSO, J. L., WESCHE, K.: *Characterization of Fly Ash, w Fly Ash in Concrete*, Ed.: K. Wesche, E & FN SPON, London, 1991, pp. 3-23.
[2] BASTIAN, S.: *Construction Concretes with Addition of Fly Ashes,* (in Polish). Arkady, Warsow, 1980.
[3] AIMIN, X., SARKAR, S. L.: *Hydration and Properties of Fly Ash Concrete, w Mineral Admixtures in Cement and Concrete,* Ed.: Ghosh S. N., ABI Books Pvt. Ltd., New Delhi, 1995, pp. 175-225.

[4] JOSHI, R. C., LOHTIA, R. P.: *Types and Properties of Fly Ash, w Mineral Admixtures in Cement and Concrete,* Ed.: S. N. Ghosh, ABI Books Pvt. Ltd., New Delhi, 1995, pp. 119–157.
[5] UCHIKAWA, H., UCHIDA, S., OGAWA K.: *Influence of Fly Ash Characteristics on the Rheological Properties of Fresh Fly Ash Cement Paste.* Proceedings Annual Meeting of Material Research Society, M4.4, Boston 1982, Concrete Rheology, pp. 203-214.
[6] KURDOWSKI, W.: *Chemistry of Cement*, (in polish). PWN, Warsow, 1991.
[7] UCHIKAWA, H.: *Effect of blending component on hydratation and structure formation.* Journal of Research of the Onoda Cement Company, 1986, vol. XXXVIII, no. 115, pp. 77.
[8] GRZESZCZYK, S., LIPOWSKI, G.: *Rheological Properties of Cement Pastes Containing Fly Ash.* International Conference on Engineering Rheology ICER '99. Zielona Góra 1999, Applied Mechanics and Engineering, vol. 4., pp. 215–220.
[9] GRZESZCZYK, S., LIPOWSKI, G.: *Effects of Low-Calcium Fly Ash on The Rheology of Fresh Cement Pastes.* Applied Mechanics and Engineering, vol. 3, no. 4, 1998, pp. 589-600.
[10] GRZESZCZYK, S.: *Rheology of cement pastes,* Monograph no. 47, KILiW Polish Science Academy, Warsow, 1999.

Janusz Szwabowski – Jacek Gołaszewski *

NÁVRH SPRACOVATEĽNOSTI VYSOKOHODNOTNÉHO BETÓNU PRI POUŽITÍ REOMETRICKÉHO TESTU

DESIGNING WORKABILITY OF HIGH PERFORMANCE CONCRETE USING RHEOMETRICAL WORKABILITY TEST

Článok uvádza a dáva na diskusiu výsledky skúmania vzájomnej kompatibility medzi cementom a superplastifikátorom za prítomnosti prevzdušňovacieho prostriedku a kremičitého úletu. Prešetrovanie sa urobilo na štandardných typoch mált pri použití reometrického testu spracovateľnosti (RTS). Výskum bol prvým krokom k návrhu vysokohodnotného betónu určeného pre použitie v mostnej konštrukcii. Výsledky plne potvrdili použiteľnosť reometrického testu spracovateľnosti (RTS) na odhad systému kompatibility medzi cementom a superplastikátorom, ako aj pre skúšky vplyvu prímesí na reologické vlastnosti čerstvého betónu.

In the paper the results of investigation on cement/superplasticizer compatibility in presence of air entraining agent and silica fume are presented and discussed. Investigation was carried out on standard mortars using rheometrical workability test (RWT). The research was a first step in designing HPC to be used in bridge construction. The research fully proves usefulness of RWT for estimation of compatibility of cement/SP systems and for testing of admixtures influence on rheological properties of fresh concrete.

1. Introduction

High performance concrete (HPC) is widely used in civil engineering as a structural material assuring high strength, durability and reliability of concrete structures. [1] Although, from a material point of view, HPC is nothing more than ordinary concrete with a very low porosity, its production causes technological problems. Low W/C, high dosage of superplasticizer (SP) and implementation of supplementary cementitious materials (usually silica fume (CSF)) [1], characteristic of HPC, cause problems mainly concerning workability. Thus, crucial for fresh HPC properties is to select an efficient SP which shows good rheological compatibility with cement. [1, 2] Compatible SP and cement should be defined as the very first step in HPC designing, and carrying it out of the presence of other admixtures and additives and condition of concreting should be taken into account.

At the present time it is impossible to know by looking at data of a particular cement and particular SP what rheological behaviour of fresh concrete can be obtained. [1, 2, 3,] Thus, it is necessary to perform a number of check tests to see how SP and cement work together. As performing concrete trial batches is time and material consuming, other methods, involving smaller amount of material and easier to implement and repeat, have been developed. These methods generally base on studying the rheological behaviour of grouts. [1, 2, 3]. Because of essential differences between rheology of grouts and fresh concretes the usability of these methods for concrete designing is very limited. [1, 4, 5] More complex and reliable information on rheological properties of fresh concrete can be obtained by testing rheological properties of modified standard mortars according to PN-EN 196-1 using rheometrical workability test (RWT). [4, 5] Because of similar behaviour of fresh mortar and fresh concrete, this method makes possible to define not only cement/SP compatibility but also gives a number of significant data about influence of SP on rheological properties of fresh concrete in presence of other admixtures and in different technological conditions. Because of qualitative nature of this data, optimal SP dosage should be defined using fresh concrete in the next steps of designing.

In the paper the results of investigation on cement/SP compatibility in presence of air entraining agent (AE) and silica fume (CSF) using RWT and standard mortars are presented and discussed. The research was the first step in designing of HPC to be used in a bridge construction. Rheological compatibility of cement and SP was assessed taking into consideration reduction of shear resistance of fresh mortars and changes of rheological properties in time. Because SP and admixtures can reveal significant secondary effects, their influence on setting time and compressive strength was also tested.

2. Experimental

Rheological compatibility was tested for two different CEM I 42.5 R cements and two SPs – of PC and SNF type. (Tables 1 &

* **Prof. dr. hab. inż. Janusz Szwabowski, Dr. inż. Jacek Gołaszewski**
Silesian University of Technology, Department of Building Processes, ul. Akademicka 5, 44-100 Gliwice, Poland,
Tel.: ++48-32-2372294, Fax: ++48-32-2372737, E-mail jski@polsl.gliwice.pl, jgolasz@polsl.gliwice.pl

2) In spite of higher effectiveness of PC than SNF type SP [for ex. 6], SNF usage was considered due to economical reason. Due to durability reason, AE and CSF were applied, and thus effect of these admixtures on rheological properties of mortars was also investigated. Mortars proportioning is presented in Table 3. Mortars were prepared according to PN EN 480-1:1999, mixing sequence is presented in Table 4.

Rheometrical workability test was performed using Viskomat PC viscometer (Fig. 1). Principles and methodology of RWT and characteristics of Viskomat PC are presented in detail in [5]. The measuring procedure used in the research, roughly simulating process of transport in truck concrete mixer, is presented on Fig. 1. Both rheological parameters were determined using the following equation:

$$T = N * h + g \quad (1)$$

where T – torque registered by rheometer
N – rotation speed
h – value of parameter related to plastic viscosity
g – value of parameter related to yield value

In rheology the yield value and plastic viscosity are normally expressed in the conventional units as g and h respectively. These parameters can be transferred into the proper yield value and plastic viscosity terms by multiplying with certain viscometer – dependent factors. In the present work the conventional units are used. The final results of each test consist of: the yield value g and plastic viscosity h results, the correlation coefficient R, representing the degree of linearity (R gives the best fit of the Bingham rheological model to the practical behaviour of material, any non typical behaviour during the test is usually apparent by an outstandingly low value of R) and estimation of the experimental errors of the yield value g and plastic viscosity h from correlation coefficients and linear regression.

Rheological properties were tested at 30 °C, only cement A and PC type SP mortars were tested at 20 °C to point out influence of the temperature. Setting times were defined on mortars according to PN EN – 480-3:1999 at the temperature of 20 and 30 °C. Compressive strength was tested according to PN EN 196-1:1996.

Properties of tested superplasticizers. Table 2

Admixture	Chemical base	Density [g/cm^3]	Concentration [%]
PC	polycarboxylate ester	1.09	36 %
SNF	naphthalene sulphonate acid	1.20	26 %

Procedure of mixing (modified procedure according to PN EN 480-1:1999). Table 4

Action	Mixing speed	Time [s]
Addition of cement, CSF and sand		
Mixing	low	30 ± 2
Addition of water (90 %) and SP		
Mixing	low	30 ± 2
Mixing	high	30 ± 2
Break		90 ± 5
Addition of water (10 %) and AE		
Mixing	high	60 ± 5

3. Test results and discussion

Rheological properties of cement A mortars with PC SP and AE and CSF at 20 °C and 30 °C are presented in Figs. 2 & 3. At the temperature of 30 °C the yield value and plastic viscosity of mortars, and thus shear resistance are clearly higher than at 20 °C. Mortars containing only addition of SP show the highest shear resistance – the yield value and plastic viscosity for these mortars are also highest. Mortars with CSF show the lower yield value and plastic viscosity – as an effect of a higher paste volume because

Chemical and mineralogical composition of tested cements. Table 1

Cement	Ingredients [%]											Specific surface
	SiO_2	CaO	Al_2O_3	Fe_2O_3	MgO	Na_2O_e	SO_3	C_3S	C_2S	C_3A	C_4AF	[cm^2/g]
A	19.7	62.3	6.3	2.5	2.2	0.74	3.1	49.1	19.7	12.5	7.6	3600
B	19.3	64.1	5.7	2.8	1.4	0.83	2.8	64.1	7.0	10.3	8.6	3602

Mix compositions. Table 3

Additives	W/(C+CSF)	Ingredients [g/batch]					
		Cement	Sand	SP PC	SP SNF	AE (0,5%) mC	CSF (10% mC)
SP	0.40	450	1350	10.13	18	–	–
SP + AE	0.40	450	1350	10.13	18	2.25	–
SP + CSF	0.40	450	1305	10.13	18	–	45
SP + CSF + AE	0.40	450	1305	10.13	18	2.25	45

CSF was used as replacement of part of sand. However, it is important to remember that addition of CSF as cement replacement increases the yield value and thus significantly decreases workability of mortars. [7] An addition of AE significantly decreases the yield value and plastic viscosity and, consequently, the shear resistance – this effect is independent on CSF. At 20 °C changes in time of mortars workability are insignificant – only plastic viscosity slightly increases in time.

An increase of temperature clearly increases workability changes in time of mortar without AE addition – the yield value distinctly increases, and shear resistance shows tendency to increase in spite of the decrease of plastic viscosity. In the case of AE mortars, due to an additional fluidising effect of such admixtures, workability changes in time are negligible.

For mortars with cement A and SNF SP to obtain the same yield value as for mortars with PC SP, two times higher dosage of admixture is necessary. (Fig. 4) In the same time, the plastic viscosity of SNF mortars is three times lower and thus shear resistance of these mortars is, in the beginning, clearly lower. However, in opposite to PC SP mortars, mortars with SNF SP, show a high workability loss during 60 min. This time the yield value rapidly increases, while the plastic viscosity significantly decreases – such

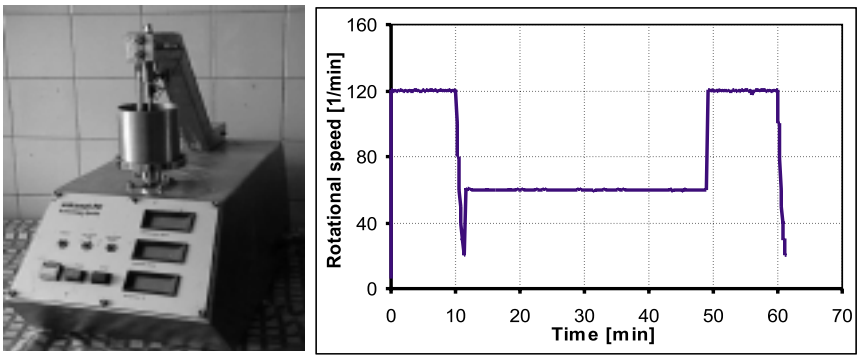

Fig. 1. Viskomat PC viscometer and measuring procedure used in tests

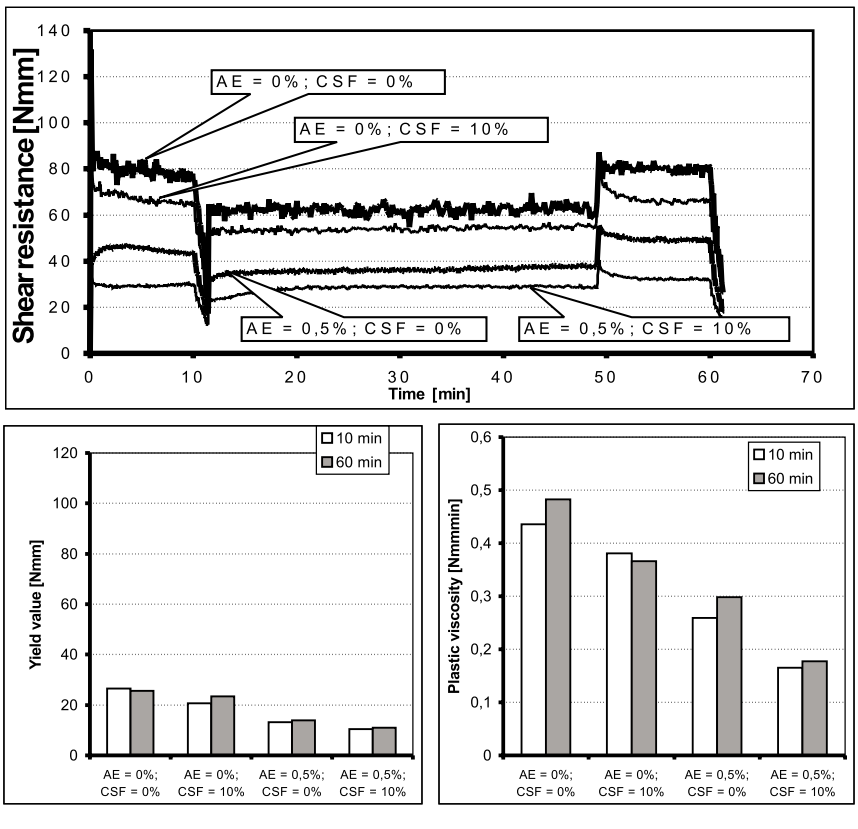

Fig. 2. Rheological properties of cement A mortars with PC SP (2.25 % C by weight), air entraining admixture (AE) and silica fume (CSF) at temperature of 20 °C; W/C = 0.40

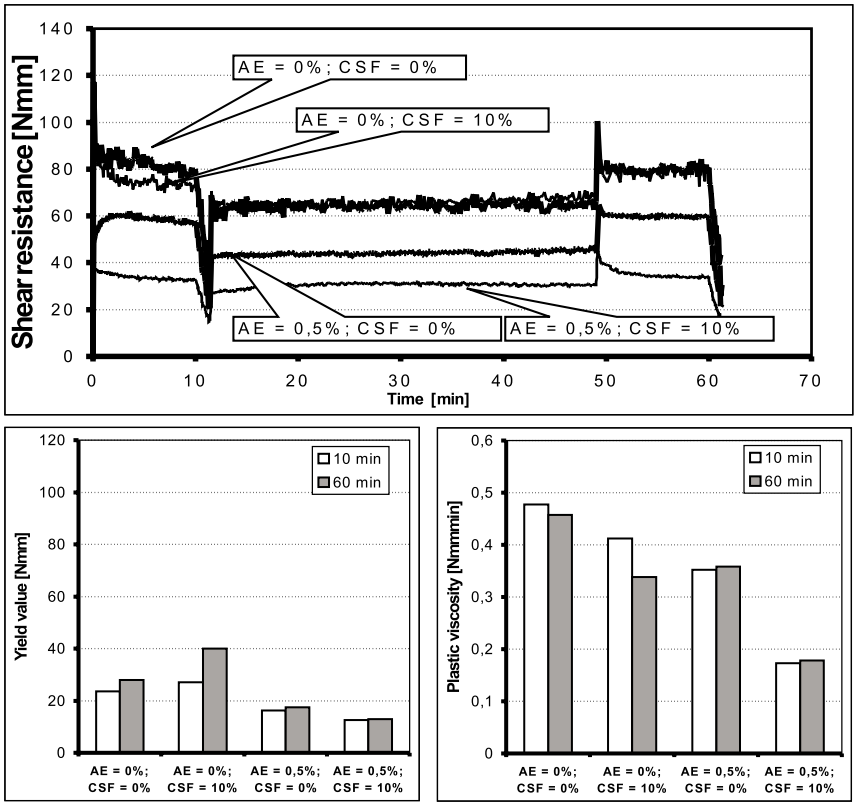

Fig. 3. Rheological properties of cement A mortars with PC SP (2.25 % C by weight), air entraining admixture (AE) and silica fume (CSF) at temperature of 30 °C; W/C = 0.40

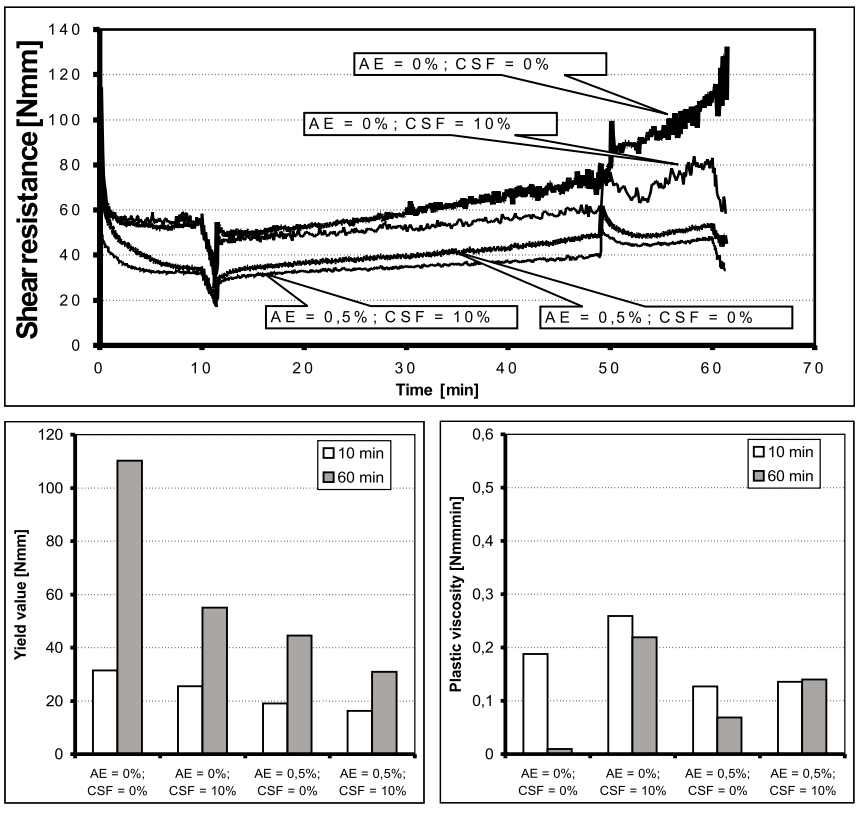

Fig. 4. Rheological properties of cement A mortars with SNF SP (4.0 % C by weight), air entraining admixture (AE) and silica fume (CSF) at temperature of 30 °C; W/C = 0.40

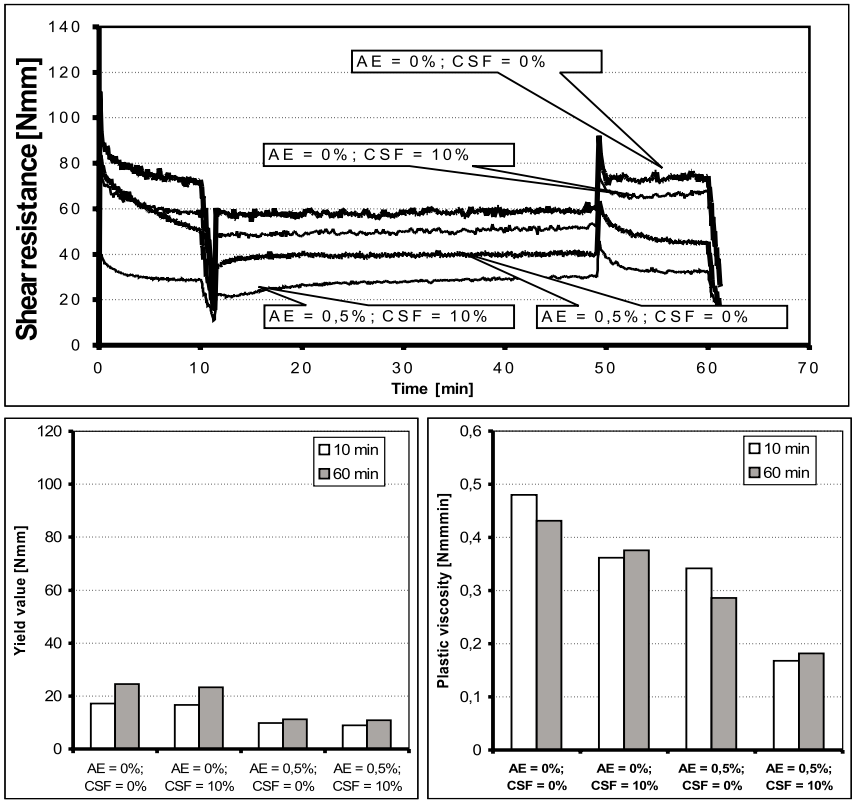

Fig. 5. Rheological properties of cement B mortars with PC SP (2.25 % C by weight), air entraining admixture (AE) and silica fume (CSF) at temperature of 30 °C; W/C = 0.40

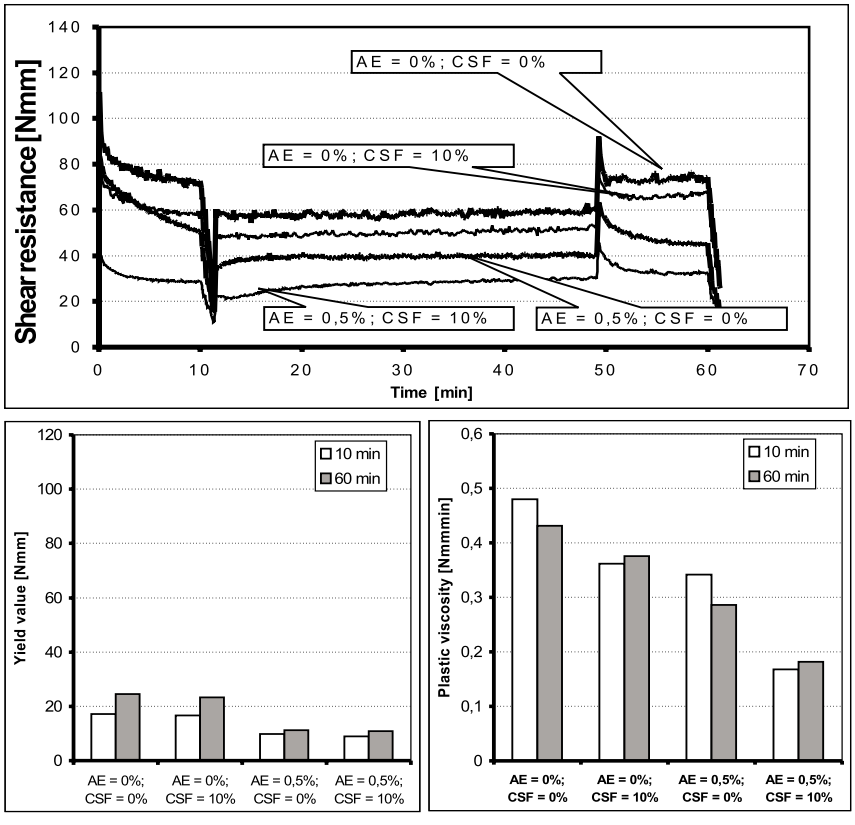

Fig. 6. Setting times of cement A & B mortars with PC SP (2.25 % of C by weight) and CSF (10 % of C by weight) and AE (0.5 % C by weight)

Compressive strength after 28 days of tested mortars [MPa]. Table 5

Cement	SP type	Temperature	SP	SP + AE	SP + CSF	SP + AE + CSF
A	PC	20 °C	51.7	30.5	68.1	34.5
A	PC	30 °C	52.9	34.3	70.0	40.6
A	SNF	30 °C	55.5	49.7	66.6	64.6
B	PC	30 °C	61.7	52,2	82.7	55.6

a meaningful changes in rheological properties of fresh concrete may be a result of technological problems during concreting and determine low usability of SNF SPs to HPC.

In Fig. 5 the effect of PC SP, AE and CSF on rheological properties of cement B mortars at the temperature of 30 °C is presented. These mortars show clearly a lower yield value and plastic viscosity than mortars with cement A at the same temperature (35 % and 10 % respectively). Mortars with cement B show also low changes of rheological properties in time – thus the workability is also very stable.

Effect of admixtures on cement A and B mortars setting at 20 and 30 °C is presented in Fig. 6. The increase of temperature significantly accelerates the setting of the mortars, but leaves enough time for safe concrete processing. Addition of SP retards the setting of mortars with cement A. In the case of cement B a disadvantageous effect of SP addition can be observed – an accelerated initial setting and, in the same time, a retarded end of the setting. Addition of AE and CSF retards the setting and covers a negative effect of SP on cement B mortars setting. At 30 °C the setting of cement B mortar with SP, AE and CSF is close to the control sample.

Compressive strengths of tested mortars are presented in Table 5. It is worth noticing that: mortars with cement B show clearly higher compressive strength than mortars with cement A. The addition of CSF causes a significant increase of compressive strength but the addition of AE substantially decreases the compressive strength.

4. Conclusions

The presented investigation makes possible to select cement B and PC SP as a rheologically compatible system suitable for designed HPC. Decisive for this choice are:

- a higher effectiveness of PC than SNF SP action – PC SP effectiveness can guarantee stable maintenance of high workability in time;
- a clearly better workability of cement B than cement A mortars at the same SP dosage – this make possible a higher reduction of water or reduction of SP dosage.
- satisfactory setting and strength properties of cement B mortars.

The obtained results also confirm that:

- the addition of AE improves workability of fresh concrete, which makes possible a reduction of SP dosage or W/C ratio;
- the temperature is an important factor influencing rheological properties of fresh concrete; effect of temperature is presented in detail and discussed in [7];
- a rheometrical workability test on modified standard mortars is a very effective method of the testing of cement/SP compatibility. RWT makes also possible a complex investigation of rheological properties of fresh HPC.

References

[1] AITCIN, P. C.: *High Performance Concrete.* EF&N SPON 1998.
[2] KUCHARSKA, L.: *Tradycyjne i współczesne domieszki do betonu zmniejszające ilość wody zarobowej.* Cement, Wapno, Beton. 2/2000
[3] *Proceedings of the Sixth CANMET/ACI Internationale Conference „Superplasticizers and Other Admixtures"* Edited by V. M. Malhorta, Nice, France, 2000.
[4] BANFILL, P. F. G: *The rheology of fresh mortar.* Mag. of Concrete Research, Vol. 43, 1991
[5] SZWABOWSKI, J.: *Reologia mieszanek na spoiwach cementowych.* Wydawnictwo Politechniki Śląskiej, Gliwice, 1999
[6] SZWABOWSKI, J., GOŁASZEWSKI, J.: *Metodyka badania efektywności działania domieszek uplastyczniających i upłynniających.* Kraków-Mogilany, III KNT MATBUD 2000
[7] SZWABOWSKI, J., GOŁASZEWSKI, J.: *Wpływ superplastyfikatora i pyłu krzemionkowego na urabialność betonu wysokowartościowego.* Cement Wapno Beton. 6/1996

Robert Černý – Michaela Totová – Jan Toman – Jaroslava Drchalová – Pavla Rovnaníková – Patrik Bayer *

ZMENY VLHKOSTNÝCH A TEPELNÝCH VLASTNOSTÍ CEMENTOVÝCH KOMPOZITOV VYSTUŽENÝCH SKLENENÝM VLÁKNOM V ZÁVISLOSTI OD TEPLOTNÉHO ZAŤAŽENIA

THERMAL LOAD INDUCED CHANGES OF HYGRIC AND THERMAL PROPERTIES OF GLASS FIBER REINFORCED CEMENT COMPOSITES

V príspevku je analyzovaný vplyv tepelného zaťaženia na základné teplotné a vlhkostné vlastnosti dvoch typov cementových kompozitov so sklenenými vláknami. Tepelná vodivosť, špecifické teplo a vlhkostná difuzivita sú určené po vystavení vysokej teplote od 600 do 800 °C. Zníženie tepelnej vodivosti o 50 % a zvýšenie vlhkostnej difuzivity v rozsahu jedného až dvoch rádov sú pozorované pri všetkých typoch testovaných materiálov po zahriatí na 800 °C. Na druhej strane špecifické teplo a hustota sú za tých istých podmienok znížené len o 10 %. Na analýzu príčin meraných rozdielov medzi vlhkostnými a tepelnými parametrami, spôsobenými teplotným zaťažením a nezaťažením vzoriek, sú použité výsledky meraného rozloženia pórov, snímania elektrónovým mikroskopom a teplotnou analýzou.

The effect of thermal load on the basic thermal and hygric properties of two types of glass fiber reinforced cement composites (GFRCC) is analyzed in the paper. Thermal conductivity, specific heat and moisture diffusivity are determined after high temperature exposure to 600 and 800 °C. A decrease of thermal conductivity as high as 50 % and an increase of moisture diffusivity in the range of one to two orders of magnitude are observed for all types of the studied materials after heating to 800 °C. On the other hand, specific heat and density in the same situation decrease by only about 10 %. In the analysis of the reasons for the measured differences between hygric and thermal parameters of thermally loaded and unloaded samples, pore distribution measurements, scanning electron microscopy and thermal analysis are employed.

1. Introduction

Glass-fiber reinforced cement composites (GFRCC) are produced by incorporating a small amount of alkali-resistant glass fiber in cement mortar to overcome the traditional weakness of inorganic cements, namely poor tensile strength and brittleness (see, e.g., [1]). The length and content of the glass fiber reinforcement can be chosen to meet the strength and toughness requirements of the product. Also, the type of aggregates can be varied in order to manage thermal properties. GFRCC are often employed in severe conditions. These might be exposed, for instance, to high temperatures and/or high mechanical loads. However, their thermal and hygric properties are mostly measured in laboratory conditions only, so that designers cannot take into account the changes in their material parameters after loading. In this paper, basic hygric and thermal properties of selected glass fiber reinforced cement composites are determined as functions of thermal load.

2. Methods for measuring thermal and hygric parameters

The measurements of thermal conductivity and specific heat were performed at room temperature using the microprocessor controlled portable device ISOMET 104 (Applied Precision). The measurement is based on an analysis of the temperature response of the analyzed material to heat flow impulses. The heat flow is excited by electrical heating of a resistive heater mounted into the probe having direct thermal contact with the samples. The temperature is sampled and as a function of time is on-line evaluated by means of polynomial regression. The coefficients of the evaluated regression polynomials are then used to calculate the measured quantities.

Moisture diffusivity κ was determined using a simple method based on the assumption that κ can be considered as piecewise constant with respect to the moisture content u (PCK method in

* [1]Prof. Ing. Robert Černý, DrSc., [1]Ing. Michaela Totová, [2]Prof. Mgr. Ján Toman, DrSc., [2]RNDr. Jaroslava Drchalová, CSc., [3]Doc. RNDr. Pavla Rovnaníková, Csc., [3]Ing. Patrik Bayer
[1]Czech Technical University, Faculty of Civil Engineering, Department of Structural Mechanics, Thákurova 7, 166 29 Praha 6, Czech Republic, E-mail: cernyr@fsv.cvut.cz;
[2]Czech Technical University, Faculty of Civil Engineering, Department of Physics, Thákurova 7, 166 29 Praha 6, Czech Republic
[3]Institute of Chemistry, Faculty of Civil Engineering, Technical University of Brno, Žižkova 17, 662 37 Brno, Czech Republic

what follows). Contrary to the most frequently used methods for κ determination, the PCK method is very fast even for materials with low κ, and, in addition, it exhibits a reasonable precision [2]. Therefore, its application for concrete is very suitable.

3. Material samples

The measurements were conducted on two types of glass fiber cement composites, denoted as SC I, II, in what follows. The samples were plate materials with a Portland cement matrix (CEM I 52.5), which was reinforced by alkali-proof glass fibers (CEMFIL, fiber length of 35 mm), the material SC II contained vermiculite and wollastonite. The basic composition of SC I, II is shown in Table 1 (the percentage is calculated among the dry substances only, water corresponding to the water to cement ratio of 0.3 is to be added to the mixture).

The samples for the determination of thermal conductivity, specific heat and moisture diffusivity were exposed to the thermal load prior to the measurements. The chosen temperatures were 600 and 800 °C. For the sake of comparison, also the measurements with unloaded samples were done. The size of samples was for SC I 60 × 70 × 10 mm, for SC II 60 × 60 × 13 mm. The specimens were water and vapor-proof insulated on four edges by two-component epoxy resin ChS Epoxy 1200.

4. Experimental results

The measurements of room temperature values of thermal conductivity, specific heat and moisture diffusivity after thermal load are summarized in Tables 2-3. Always an average value from the measurements on five samples is given. Both thermal conductivity and specific heat are found to decrease with increasing the loading temperature, and the decrease of thermal conductivity is very remarkable, almost 50 % compared to the room temperature data. The moisture diffusivity exhibits an opposite behavior, a two order of magnitude increase for SC-I and one order of magnitude increase for SC-II are observed comparing the room temperature data with the data for high temperature exposure to 800 °C. It should be noted that the changes of thermal and hygric parameters are more remarkable between 25 °C and 600 °C than between 600 °C and 800 °C.

5. Discussion

In order to explain the observed differences in thermal and hygric parameters after the thermal load, mercury porosimetry, scanning electron microscopy have been done. The curves of DTA have been determined before thermal load of sample SC I and SC II, Fig. 1 and 2.

Pore volumes of samples, which have been heated at different temperatures are given in Figs. 3 and 4. Microstructure of samples at 20, 600 and 800 °C are given in Figs. 5 and 6. Fibers loaded at temperature 600 °C are not damaged, temperature 800 °C caused their collapse.

The fibers react at high temperature with cement paste and lose their round form and distort. The cement paste in sample SC I changes character of pores, see the graph in Fig. 3. The fibers of wollastonite are more stable at high temperature and they keep the

Composition of glass fiber reinforced cement composites in % — Table 1

	Cement	Sand	Plasticizer	Alkali-proof fiber	Wollastonite	Vermiculite
SC I	47.99	47.99	0.62	3.40		
SC II	47.60		0.45	3.84	38.50	9.61

Thermal and hygric parameters of SC I — Table 2

Temperature exposure [°C]	ρ_s [kg m^{-3}]	C [J kg^{-1} K^{-1}]	λ [W m^{-1} K^{-1}]	u_{max} [%]	κ [m^2 s^{-1}]
25	1960	920	1.124	10.6	$1.28.10^{-9}$
600	1865	920	0.706	15.6	$9.57.10^{-8}$
800	1820	900	0.666	16.2	$1.79.10^{-7}$

Thermal and hygric parameters of SC II — Table 3

Temperature exposure [°C]	ρ_s [kg m^{-3}]	C [J kg^{-1} K^{-1}]	λ [W m^{-1} K^{-1}]	u_{max} [%]	κ [m^2 s^{-1}]
25	1090	1090	0.275	47.5	$2.52.10^{-8}$
600	1030	1050	0.198	56.8	$1.27.10^{-7}$
800	990	960	0.160	56.8	$3.18.10^{-7}$

structure of cement paste stronger than glass fibers. It is confirmed also by thermogravimetric analysis, see Figs. 1 and 2.

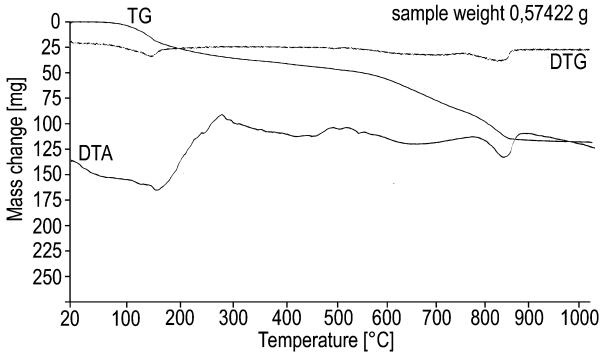

Fig. 1. Thermal analysis of sample SC I

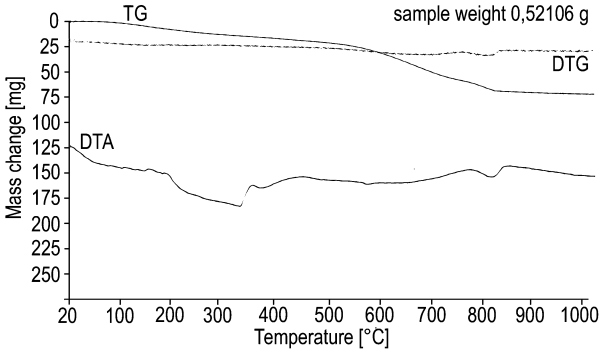

Fig. 2. Thermal analysis of sample SC II

Room temperature properties of the three analyzed types of glass fiber reinforced cement composites (GFRCC) are affected by the type of aggregates in the most significant way. Application of wollastonite and vermiculite instead of usual sand aggregates leads to a remarkable decrease of thermal conductivity. On the other hand, moisture diffusivity of GFRCC with wollastonite and vermiculite is higher compared to the sand aggregates, which is a clear consequence of a decrease of density to about one half. These are the logical consequences particularly of the character of vermiculite which has remarkably lower density compared to the sand.

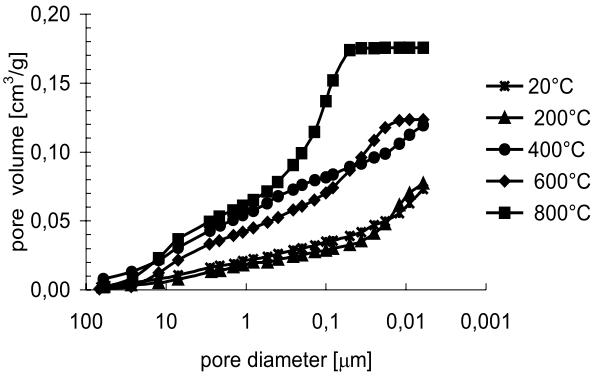

Fig. 3. Porosimetry of sample SC I

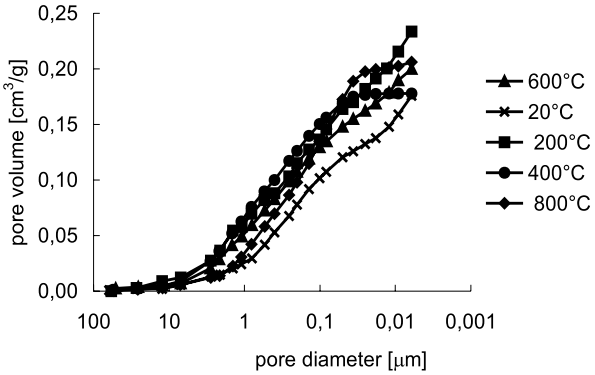

Fig. 4. Porosimetry of sample SC II

On the other hand, the behavior of GFRCC exposed to high temperatures is affected by the properties of the cement binder in the most significant way. The very fast increase of moisture diffusivity and a relatively fast decrease of thermal conductivity of all

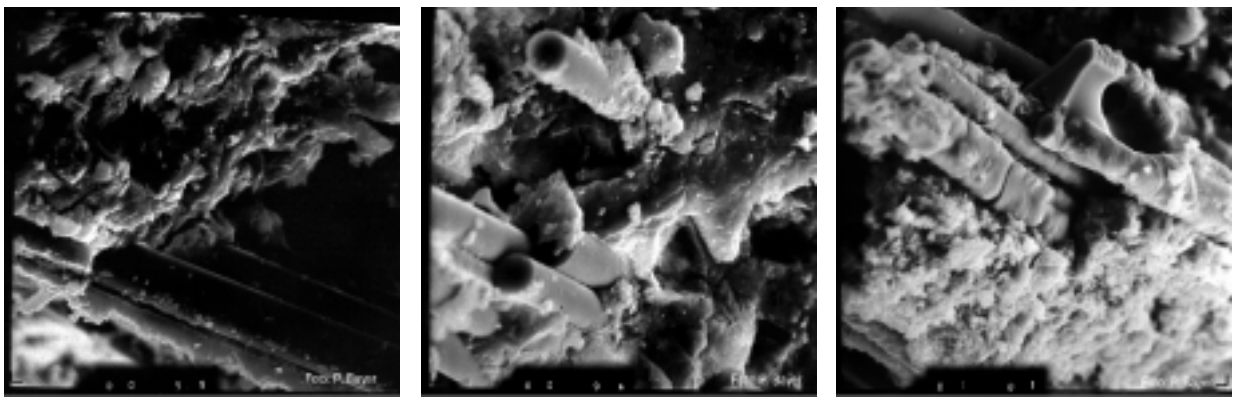

Fig. 5. Scanning micrographs of sample SC I

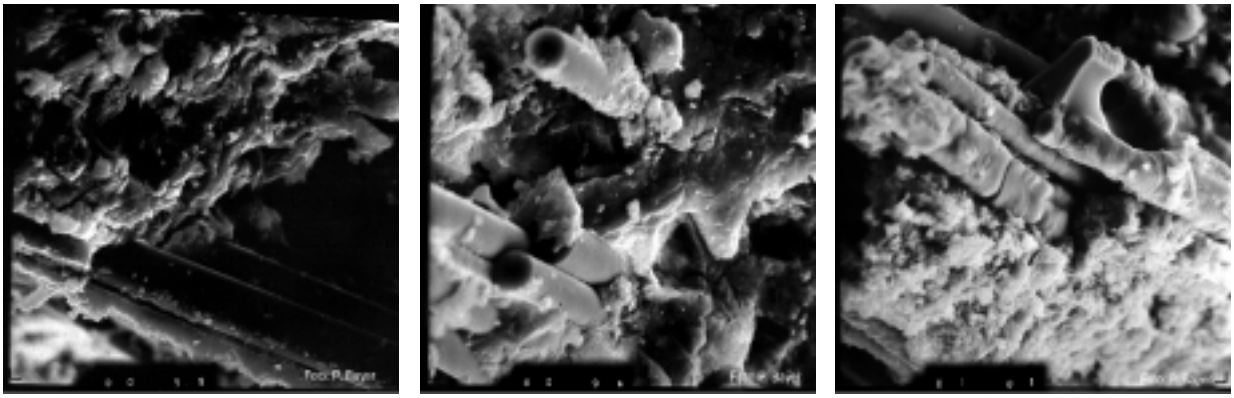

Fig. 6. Scanning micrographs of sample SC II

three materials with the heating temperature correspond well with the characterization experiments performed. From the point of view of structural changes in the cement gel, for the temperature range up to 1000 °C two processes are the most important, namely the decomposition of $Ca(OH)_2$ at about 490 °C and decomposition of calcium silicate hydrates at about 700 °C. During these processes, gaseous substances are released, water vapor in the first case, and carbon dioxide in the second. Therefore, the amount of bigger pores increases, which makes the liquid water transport easier and faster. In addition, due to the fast generation of a substantial amount of the mentioned gaseous substances, the local overpressure in some parts of the porous system may lead to crack appearance, and consequently to the opening of preferential paths for the pore water flow. The increasing amount of larger pores then logically leads to a decrease of thermal conductivity because of the increasing amount of the air in the material.

The much faster increase in moisture diffusivity of SC-I between 25 °C and 600 °C compared to SC-II was most probably a consequence of opening of wider preferential paths after the high temperature exposure because in normal conditions SC-I possesses lower moisture diffusivity than SC-II. A logical reason is the better function of glass fibers in SC-II, i.e. their better adhesion to the cement-aggregates matrix.

6. Conclusions

Two main factors were found to affect the properties of the studied GFRCC in the most significant way. For the room temperature parameters, the type of aggregates was found to be dominant, and an application of wollastonite and vermiculite instead of sand aggregates was identified to have a very positive effect because the thermal conductivity decreased in a significant way. Positive effect on the pore structure and mass loss has been also found. In the case of the high temperature exposure, the decomposition processes in the cement gel can be considered as the most important.

Acknowledgement

This research has been supported by the Grant Agency of the Czech Republic, under grant No. 103/00/0021.

References

[1] MAJUMDAR, A. J., LAWS, V.: 1991. *Glass Fibre Reinforced Cement.* BSP, Oxford.
[2] DRCHALOVÁ, J, ČERNÝ, R, HAVRDA, J.: 2000. *The Effect of Anisotropy of Building Materials on the Moisture Transfer.* Acta Polytechnica, Vol. 40, pp. 32-35.

Milan Moravčík *

DYNAMICKÉ CHOVANIE ŽELEZNIČNEJ TRATE – EXPERIMENTÁLNE MERANIA

DYNAMIC BEHAVIOUR OF RAILWAY TRACK – EXPERIMENTAL MEASUREMENTS

Príspevok je venovaný dynamickým meraniam konštrukcie trate zaťaženej prevádzkovým zaťažením a stručne prezentuje niektoré experimentálne postupy hodnotenia dynamického chovania trate. Vertikálne kmitanie koľajníc, podvalov a povrchu štrkového lôžka vo vzdialenosti 1 m od koľajníc, ako aj meranie dynamickej interakčnej sily koľajnice/podval sú analyzované v časovej aj frekvenčnej oblasti. Získané výsledky dávajú užitočné informácie a údaje o dynamickej reakcii koľajového roštu zaťaženého pri prejazde vlakov.

The objective of the paper is devoted to in situ dynamic measurements on the track structure under traffic and briefly to present some experimental approaches in order to appreciate the dynamic behaviour of the track structure. The vertical vibration of rails, sleepers and free ballast field at a distance of 1m from the track and the direct dynamic interaction force the rail / the sleeper were measured and analysed in the time and frequency domain. Received results can give many useful indications concerning the assessing of the superstructure dynamic behaviour.

1. Úvod

Dynamická reakcia konštrukcie trate je stále študovaná v teoretickej aj experimentálnej oblasti ako prioritný problém mechaniky železničnej trate, najmä s ohľadom na zvyšovanie prevádzkových rýchlostí a zaistenie vysokej spoľahlivosti sústavy pohybujúce sa vozidlo – trať. Navyše pristupujú aj ďalšie požiadavky, ako napríklad podmienky kladené na stabilitu trate, údržbu, presnosť geometrickej polohy trate, resp. prenos vibrácií a hluku do okolia tratí. Jedným z výskumných cieľov Katedry stavebnej mechaniky SvF v tejto oblasti je rozvoj metód hodnotenia dynamických vlastností a dynamického chovania konštrukcie trate, ktoré sú zamerané najmä na klasickú konštrukciu trate uloženú v štrkovom lôžku. V tomto duchu bol spracovaný aj program teoretických a experimentálnych prác zameraných na dynamickú interakciu vozidlo/trať, ktorý zahŕňa:

- Rozvoj teoretických výpočtových modelov interakcie vozidlo – – trať.
- Počítačové simulácie a výpočty sústredené na predpoveď parametrov dynamickej odozvy trate – deformácie a napätosť komponentov koľajového roštu a podložia.
- Experimentálne meranie parametrov odozvy trate.
- Statické a dynamické testovanie komponentov trate – podvalov, systémov pružného upevnenia, pružných podložiek, interakcie podval – štrkové lôžko a pod.

Program experimentálnych meraní je zameraný na:

- Vyšetrovanie dynamického chovania komponentov trate (koľajníc, podvalov, štrkového lôžka) v prevádzkových podmienkach zaťaženia trate.

1. Introduction.

The dynamic behaviour of the railway track structure is still studied both theoretically and experimentally as a primary problem of the track mechanics, in particular because of increasing the train speed and assuring the high reliability of the system vehicle – track. Sometimes operational conditions, e.g. conditions in mainlines, impose special requirements for stability of tracks, for maintenance, for positioning accuracy, for vibration transmission or noise radiation to the surroundings which should be accepted. The dynamic behaviour of railway tracks is directly related to most of these items. One of the research goals of the Department of Structural Mechanics in this field is development of suitable methods for the evaluation of dynamic properties and the dynamic behaviours of the track structure focused on the conventional ballasted track. With this purpose the program of theoretical and experimental works studying the interaction dynamic problems of the vehicle – track, with focuse on the track and the dynamic behaviour of track, has been undertaken in our workplace. Generally, this program comprises:

- Development of theoretical and mathematical models for interaction problems of the vehicle and the track.
- Computer simulation and calculations to predict dynamic response parameters – deformations and stresses in the superstructure and in the substructure.
- In situ measurements of response parameters of the track structure.
- Static and dynamic tests for the track structure components – sleepers, fastening systems, resilient pads, the sleeper – ballast interaction, etc.

* **Prof. Ing. Milan Moravčík, CSc.**
Department of Structural Mechanics, Faculty of Civil Engineering, University of Žilina, Komenského 52, 010 26 Žilina, Slovak Republic

- Porovnanie dynamickej reakcie trate na betónových a drevených podvaloch.
- Hodnotenie zmien v dynamickej reakcii trate ako dôsledku celkového zaťaženia trate, prevádzkovej rýchlosti a pod.
- Testovanie trate na rázového zaťaženie.

Tento príspevok je venovaný dynamickým meraniam trate zaťaženej v prevádzkových podmienkach a stručnej prezentácii prístupov riešenia a hodnotenia dynamickej reakcie trate.

2. Dynamické merania in situ

Dynamická odozva trate je vyšetrovaná pre typické usporiadanie konštrukcií trate, pre charakteristické skladby vlakov a charakteristické sekcie trate:

- priame traťové úseky so zváranými koľajnicovými pásmi mimo zvarov a pri zvaroch koľajníc,
- v oblúkoch,
- na výhybkách.

Experimentálne merania prezentované v tomto príspevku sú venované meraniu v priamych traťových úsekoch na hlavnej trati Žilina – Košice v 331,7 km (úsek Teplička).

Trať

Merania sa uskutočnili na klasickej konštrukcii trate so štrkovým lôžkom. Zvárané koľajnicové pásy UIC 60 s hmotnosťou $m_r = 60$ kg/m a momentom zotrvačnosti $I_r = 0{,}3038.10^4$ m^4 sú upevnené na betónových podvaloch typu SB 8, s dĺžkou 2,42 m, šírkou 0,28 m, výškou $h = 0{,}20$ m a hmotnosťou $m_s = 272$ kg. Koľajnice sú pripevnené k podvalom podkladnicovým systémom zvierkami ŽS 4 a pružnými podložkami hrúbky $t = 0{,}01$ m pod koľajnicou.

Vlaky

Meraný úsek bol zaťažovaný prevádzkovým zaťažením – osobnými a nákladnými vlakmi. Typické zostavy prechádzajúcich vlakov zahrňujúce lokomotívu a osobné, resp. nákladné vagóny sú znázornené na obr. 1. Schémy lokomotív pre osobné a nákladné vlaky sú ukázané na obr. 2. Rýchlosť osobných vlakov v meranom priamom úseku bola 90 km/h ÷ 140 km/h. Rýchlosť nákladných vlakov sa pohybovala od 40 km/h ÷ 70 km/h. Lokomotívy osobných vlakov (typy L350, L162, L163, L150, L363) sú uložené na dvoch podvozkoch. Lokomotívy nákladných vlakov sú typu 2 × L131 (2 × 85 t), L182 (85 t), L183 (85 t), L121 (88 t) a L363 (87 t).

Základné charakteristiky lokomotív a vagónov osobných vlakov – celková dĺžka L_t, vzdialenosť podvozkov L_b, vzdialenosť náprav L_a, celková hmotnosť vozidiel M_t a hmotnosť pripadajúca na 1 nápravu M_{1a} sú sumarizované v tab. 1.

3. Meracia zostava

Experimentálne meranie bolo sústredené na identifikáciu dynamickej odozvy komponentov trate od účinkov dopravy:

The programme of experimental measurements aimed to:

- Investigation the dynamic behaviour of track components (rails, sleepers, ballast bed) for the dynamic track loading in operational conditions.
- Comparison of the dynamic behaviour of the track structure for the track on concrete sleepers and on wooden sleepers.
- Investigation of changes in the dynamic behaviour of the track structure as a function of load tonnage, train speed, etc.
- Impact of loading tests of the track structure.

This paper is devoted to in situ dynamic measurements on the track structure under traffic and briefly presents some experimental approaches in order to appreciate the dynamic behaviour of the track structure.

2. In situ dynamic measurements

The dynamic response of the track is experimentally measured for a typical arrangement of track structures, for some typical configuration of passage trains and for characteristic track sections:

- straight sections out of rail welds and near welds,
- in curve sections,
- in turnouts.

Experimental measurements presented in this paper correspond to in situ measurements at the straight section of the main line Žilina – Košice in 331.7 km (in site Teplička).

The track

Measurements were performed on the conventional ballast track in the section of straight track. Continuously welded UIC 60 rails with a mass per unit length of $m_r = 60$ kg/m and a moment of inertia $I_r = 0.3038.10^{-4}$ m^4 are fixed on the concrete monoblock sleepers of the type SB 8 with a length $l = 2.42$ m, a width $b = 0.28$ m, a high $h = 0.20$ m, and a mass $m_s = 272$ kg. The rails were fastened to the sleepers with steel baseplates and clip bolts ŽS 4. Flexible rail pads with thickness $t = 0.01$ m were placed under the rail.

The trains

The measured line was loaded in operational conditions by passenger trains and freight trains. The typical configuration of passage trains, consisting of a locomotive and carriages or wagons is shown in Fig. 1. Schemes of locomotives for passenger trains and freight trains are shown in Fig. 2. The speed of passenger trains in the measured section varied between 90 km/h ÷ 140 km/h. The speed of the freight trains varied between 40 km/h ÷ 70 km/h. The locomotives of passenger trains (types L350, L162, L163, L150, L363) are supported by 2 bogies. The locomotives of freight trains are of 2 × L131 (2 × 85 t), L182 (85 t) and L183 (85 t) and L121 (88 t), L363 (87 t) types.

The basic characteristics of locomotives and carriages for the coaching traffic - the carriage total length L_t, the distance between bogies L_b, the axle distance L_a, the total masse M_t and axle masses M_{1a} are summarised in Table 1.

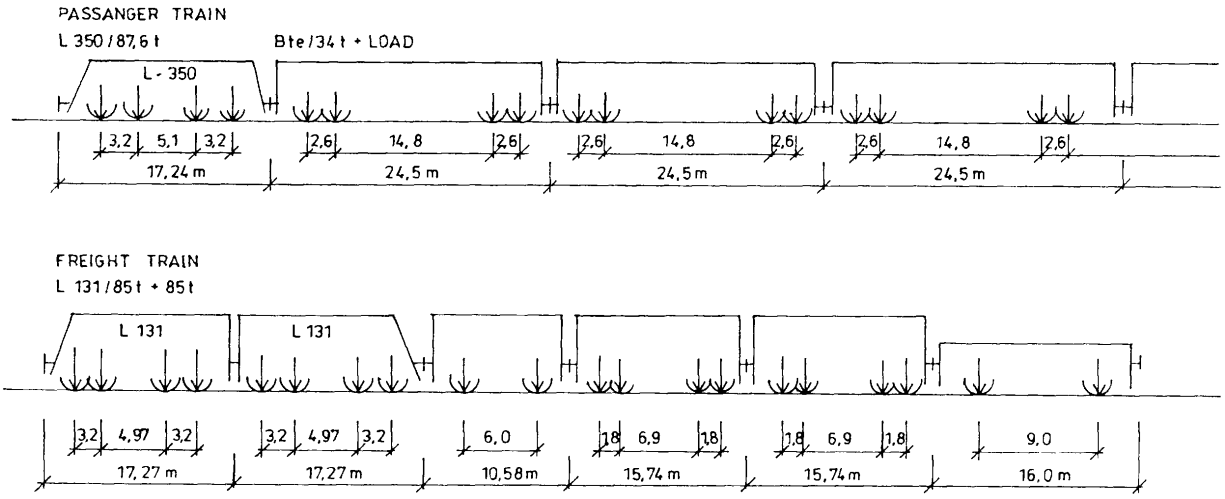

Obr. 1. Typická zostava osobného a nákladného vlaku
Fig. 1. A typical configuration of a passenger train and a freight train

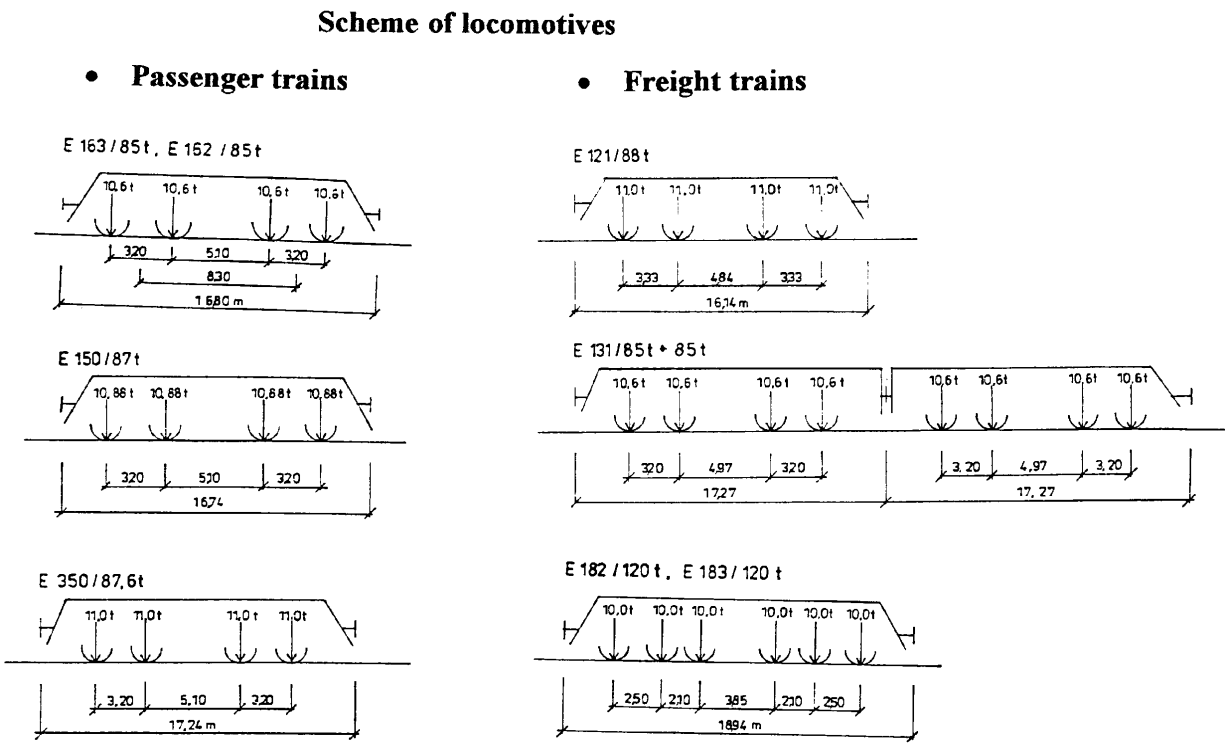

Obr. 2. Schéma lokomotív pre osobné a nákladné vlaky
Fig. 2. Scheme locomotives for passenger trains and freight trains

1. Vertikálne kmitanie koľajníc, podvalov a povrchu štrkového lôžka vo vzdialenosti 1 m od trate. Merali sa vertikálne posuny $w(t)$ a vertikálne zrýchlenia $\ddot{w}(t)$ týchto komponentov. Piezoelektrické akcelerometre B&K typu BK 4500 boli nalepované na koľajnicu a podvaly. Na hodnotenie kmitania štrkového lôžka boli použité akcelerometre typu BK 8306. Vertikálne posuny $w(t)$ koľajníc a podvalov boli merané relatívnymi snímačmi

3. Measurement setup

The measurement focused on the identification of dynamic response of the track components under traffic:

1. *The vertical vibration of rails, sleepers and free ballast field* at a distance of 1 m from the track. They were measured as the vertical displacement $w(t)$ and the acceleration $\ddot{w}(t)$ of these

Geometrické a hmotnostné charakteristiky koľajových vozidiel pre osobnú dopravu na ŽSR. Tab. 1
Geometrical and the mass characteristics of vehicles for coaching traffic in ŽSR Table 1

Locomotives	Axles	Length [m]			Mass [t]	
		L_t	L_b	L_a	M_t	M_{1a}
EL 162,163	4	16.80	5.10	3.20	85.0	10.625
EL350	4	17.24	5.10	3.20	87.6	10.950
EL 362,363	4	16.80	5.10	3.20	87.0	10.875
EL 150	4	16.74	5.10	3.20	87.0	10.875
Carriages	Axles	L_t	L_b	L_a	M_t	M_{1a}
Bte	4	24.5	14.6	2.6	34.0 ÷ 44.0	4.25 ÷ 5.50
Bai	4	24.5	14.8	2.4	38.0 ÷ 46.0	4.75 ÷ 5.75
Ba	4	24.5	14.7	2.5	39.0 ÷ 47.0	4.80 ÷ 5.80

posunutí typu Bosh umiestenými na pevne fixovanej meracej konzole, obr. 3.

2. Dynamické interakčné sily koľajnica – podval $F_{R\text{-}S}(t)$ sa merali piezoelektrickým snímačom sily typu Kistler, ktorý sa vkladal medzi koľajnicou a podval namiesto vybranej podkladnice, pozri obr. 3. Vložený snímač sily môže byť predpínaný na zvolené pritlačenie koľajnice a podvalu.

3. Dynamické pomerné pretvorenie $\varepsilon(t)$ koľajnicových pásov merané pomocou príložného piezoelektického tenzometra typu Kistler osadeného na spodnej strane päty koľajnice medzi podvalmi.

Merané veličiny boli zaznamenané ako elektrické signály pomocou analogovo-digitálneho16-kanálového konvertora DAS 16 alebo 32-kanálového záznamového systému Disys a tiež paralelne na 4-kanálový magnetofón typu BK 7005. Skutočné rýchlosti prechádzajúcich vlakov boli určované zo záznamov meraných signálov. A/D prevodník zaznamenáva merané signály so zvolenou vzorkovacou frekvenciou f_s priamo do pamäte počítača. Vzorkovacia frekvencia v týchto meraniach hrá pritom významnú úlohu najmä vzhľadom na rýchlosť meraných procesov (rázové procesy). Pokiaľ dominantne frekvenčná skladba kolesových síl a priehybov koľajníc a podvalov zodpovedá nízkym frekvenciám, frekvenčná skladba zrýchlení týchto pohybov leží v oveľa širšej oblasti.

Pri meraniach dynamickej odozvy trate sa vzorkovacia frekvencia f_s volí nasledovne:

a) Pre hodnotenie nízkofrekvenčnej odozvy komponentov trate: $f_s = 200$ Hz.
b) Pre hodnotenie stredne frekvenčnej odozvy komponentov trate: $f_s = 500 \div 1000$ Hz.

4. Výsledky meraní

Merané signály odozvy trate zaznamenané do pamäte počítača pomocou meracích systémov Das alebo Disys, resp. Bk meracieho magnetofónu sa spracovali aplikáciou modulov analýzy týchto sys-

components. The B&K piezoelectric accelerometers of the type BK 4500 were glued to the rail and the sleeper. For the ballast response the BK 8306 seismic accelerometers were used. The vertical displacements $w(t)$ of rails and sleepers were measured by the relative displacement transducers of the Bosh type mount- ed on the fixed reference datum, see Fig. 3.

2. *The direct dynamic interaction force the rail – the sleeper* $F_{R\text{-}S}(t)$ were measured by a Kistler piezoelectric load cell inserted between the rail and sleeper placed instead of the removed baseplate, see Fig. 3. The inserted load cell is prestressed to the selected value.
3. *The direct dynamic strain* $\varepsilon(t)$ *of the rail* was measured by a Kistler attached piezoelectric tensiometer mounted on the rail flange.

The measured quantities were recorded as electrical signals by means of an analog-digital convector of a 16-channel DAS 16 type, or the Disys 32 channel system for data acquisitions and they were recorded in a parallel way with a BK 4-channel tape recorder of a BK 7005 type. The actual train speed was derived from continuous records of passage trains. The A/D device records signals with a chosen sampling frequency f_s directly into the computer memory. In track response measurements the sampling frequency plays an important role because of speedy processes (impact processes). While the dominant frequency composition of wheel forces and deflection of rails and sleepers lie in the low frequency range, the frequency content of accelerations of these motions lies in a much wider frequency range.

In our dynamic response measurements the sampling frequency f_s were chosen as follows:

a) For appreciation of the low frequency response of track components: $f_s = 200$ Hz
b) For appreciation of the middle frequency response of track components: $f_s = 500$ Hz $\div$ 1000 Hz.

4. Measurement results

Measured signals of the track response recorded and stored on the disk in Das and Disys systems and the BK recorder were processed using an analyser modulus of these systems. Signals in

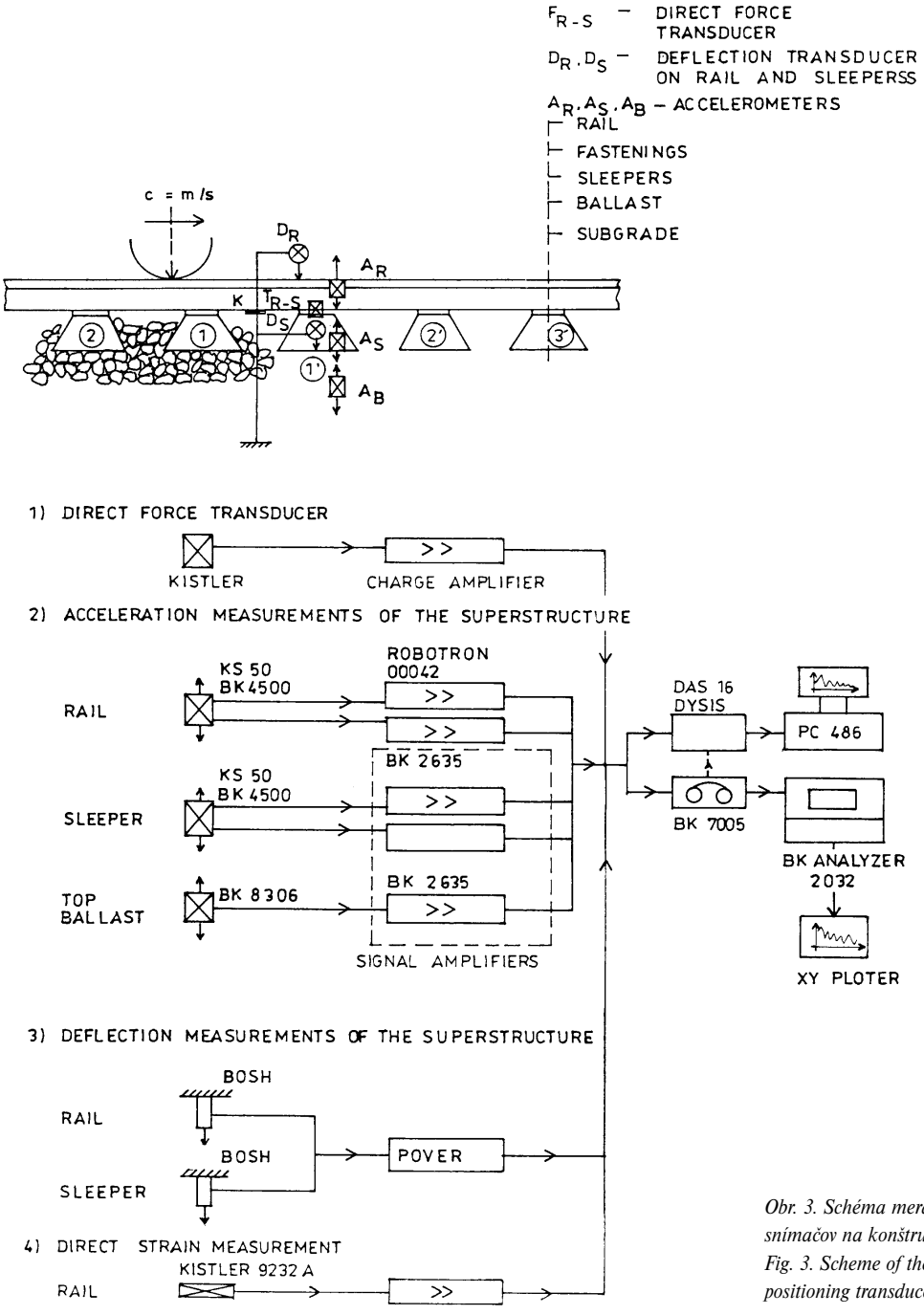

Obr. 3. Schéma meracej zostavy a umiestnenie snímačov na konštrukcií trate.
Fig. 3. Scheme of the measurement setup and positioning transducers in the track

témov, v ktorých merané signály sa vhodne editujú, pracujú a vykresľujú. Signály sa analyzujú v časovej a následne frekvenčnej oblasti. Všeobecne môžeme povedať, že v prevádzkových podmienkach každý prierez koľajnice alebo každý podval je zaťažovaný postupnosťou impulzov alebo rázov vyvodzovaných prechodom náprav vozidiel vyšetrovaným miestom. Toto dynamické zaťaženie vyvoláva dynamickú napätosť a pretvorenie v komponentoch trate a zodpovedajúce dynamické priehyby a zrýchlenia majú charakteristický priebeh, ktorý v časovej oblasti je ukázaný na obr. 4 a obr. 5.

these modulus can be edited, plotted and managed (integration, derivation, filter, FFT frequency analysis). Signals are analysed in the time domain and next in the frequency domain. Generally, we can say that in service conditions each rail cross-section or each sleeper is loaded by a sequence of impacts or shocks from the passage wheels of the train. This dynamic load induces a dynamic stress and strain in rails, sleepers and subgrade and corresponding dynamic deflections and accelerations of these components having a characteristic shape in time domain, see Figs. 4 and 5.

Časový priebeh vertikálnej odozvy trate

Typické príklady časových priebehov vertikálnej odozvy sledovaných komponentov trate sú prezentované na obr. 4 a obr. 5.

- *Časový priebeh vertikálnej odozvy trate pri prejazde osobného vlaku* v sledovanom priamom úseku (mimo zvarov koľajníc), rýchlosť c = 115 km/h. Vzorkovacia frekvencia f_s = 100 Hz. Časové záznamy sa analyzovali systémom Disys, obr.4.
  - Dynamická interakčná sila koľajnica/podvaly $F_{R\text{-}S}(t)$, záznam piezoelektrického snímača sily Kistler zodpovedá nízkemu predpätiu snímača $\Delta F_{R\text{-}S}$ = 1,5 kN, obr. 4a.
  - Vertikálne posunutia koľajnice $w_R(t)$, filtrovaný signál pre $f \in$ (0 – 20 Hz), obr. 4b.
  - Vertikálne zrýchlenie koľajnice $\ddot{w}_R(t)$, nefiltrovaný záznam pre $f \in$ (0 – 500 Hz), obr. 4c.
  - Vertikálne premiestnenie hlavy podvalu $w_S(t)$, filtrovaný záznam pre $f \in$ (0 – 20 Hz), obr. 4d.
  - Vertikálne zrýchlenie podvalu $\ddot{w}_R(t)$, nefiltrovaný záznam pre $f \in$ (0-500 Hz), obr. 4e.
- *Časový priebeh vertikálnej odozvy trate pri prejazde nákladného vlaku* sledovaným priamym úsekom trate, c = 57 km/h. Aplikovaný je modul analýzy systému Disys. Na obr. 5 sú prezentované časové priebehy rovnakých veličín odozvy ako v predchádzajúcom prípade prejazdu osobného vlaku.

Z obr. 4 a obr. 5 vidieť, že časové záznamy umožňujú dobrú identifikáciu prejazdu podvozkov, resp. náprav koľajových vozidiel, aj korešpondujúce amplitúdy meraných veličín. Tieto amplitúdy dávajú dobrý obraz dynamických vplyvov kolies vozidiel na konštrukciu trate.

Frekvenčná skladba vertikálnej odozvy

Transformácia meraných signálov do frekvenčnej oblasti dáva podrobnú informáciu o kmitaní trate a o koncentrácii mechanickej energie na jednotlivé frekvenčné zložky. Aplikovaný systém analýzy zároveň umožňuje spracovať ďalšie informácie o odozve, napr. frekvenčnú odozvu (FRF), vzájomné spektrum, vzájomnú koreláciu a pod. Frekvenčná odozva hrá v procesoch poškodenia rozhodujúcu úlohu a teda dynamika sústavy pohybujúce sa vozidlo/trať musí byť známa. Pritom možno predpokladať, že nízkofrekvenčná odozva vo frekvenčnej oblasti 1 ÷ 100 Hz ale aj stredne frekvenčná odozva v oblasti 100Hz ÷ 500Hz hrá v dynamike tratí dôležitú úlohu. Dynamika komponentov trate – podvaly, podložky, štrkové lôžko a podložie v týchto frekvenčných oblastiach významne ovplyvňuje celkové dynamické reakcie trate.

Pokiaľ spektrálna analýza záznamov kmitania založená na FFT poskytuje dobrý popis stacionárnych a pseudostacionárnych signálov kmitania, nestacionárne signály by mali zohľadňovať ich spektrálne zloženie vzhľadom na čas. Jedna z ciest riešenia je aplikácia funkcie časových okien, ktorými sa v zázname analyzujú charakteristické časové úseky, ktoré majú stacionárny charakter, alebo ktoré popisujú charakteristické javy kmitania.

4.1. Nízkofrekvenčná analýza odozvy trate

Prezentovaná je vertikálna odozva trate od účinku prejazdu vlakov v meranom priamom úseku trate (mimo zvarov koľajníc),

Time history of the vertical track response

Typical examples of the time history of the vertical response of track components are presented in Figs. 4 and 5.

- *The Time history of the vertical track response for the passenger* train passage in a straight track section (out of rail welds), c = = 115 km/h. The sampling frequency f_s = 1000 Hz. The analyser modulus of the Disys system is applied, Fig. 4.
  - The direct dynamic interaction force a rail – a sleeper $F_{R\text{-}S}(t)$, the Kistler piezoelectric load cell was prestressed to a low value $\Delta F_{R\text{-}S}$ = 1,5 kN, Fig. 4a.
  - The vertical displacement of the rail $w_R(t)$, the filtered record for $f \in$ (0 – 20 Hz), Fig. 4b
  - The vertical acceleration of the rail $\ddot{w}_R(t)$, Fig. 4c
  - The vertical displacement of the sleeper $w_S(t)$, the filtered signal for $f \in$ (0 – 20 Hz), Fig. 4d
  - The vertical acceleration of the sleeper $\ddot{w}_S(t)$, Fig. 4e.
- *The Time history of the vertical track response for the freight train passage* in a straight track section (out of rail welds) of the line, c = 57 km/h. The analyser modulus of the Disys system is applied. In Fig. 5. are presented identical measured time histories of the vertical track response as in the foregoing case of the passenger train passage.

As we can see from Figs.4 and 5 time histories allow well detection passages of bogies and axles of vehicles and the corresponding detection peaks of the measured value. Amplitudes of the measured values give a good picture of dynamic effects of the wheel load on the track structure.

Frequency content of the vertical track response

Transformation of measured signals to the frequency domain provides comprehensive information about track vibration and gives a picture of concentration of energy on frequency components. The analyser module of an applied system enables, at the same time, to process additional information of the response, for example, the frequency response function (FRF), the cross spectrum, the cross correlation, etc. The FRF plays a meaningful role in the damage process where the full train – track dynamics has to be taken into account. Moreover, it is expected that the low-frequency response range 1 Hz ÷ 100 Hz and the mid-frequency range between 100 Hz ÷ 500 Hz play an important role in the track dynamics. In these frequency ranges the track components – sleepers, pads, the ballast and subsoil have a strong influence on the track system behaviour.

While traditional spectral analysis techniques based on FFT provide a good description of stationary and pseudostationary signals, non-stationary signals should be analysed with consideration of spectral information in time. One of the techniques applied here uses a window function to window out short sections of the overall signal which are near stationary or which contain isolated events.

4.1. The low-frequency analysis of the track response

The vertical track response for the passenger train passage in a straight track section (out of rail welds), c = 115 km/h is pre-

***Teplička III/2000** / The time history of the vertical track response for **the passenger train passage** in a straight track section (out of rail welds), c=115 km/h,.*

a) The direct dynamic interaction force a rail – a sleeper $F_{R\text{-}S}$(t)

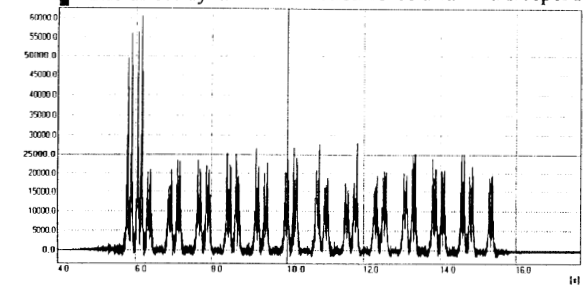

b) The vertical displacement of the rail $w_R(t)$, the filtered signal for $f \in (0-20Hz)$

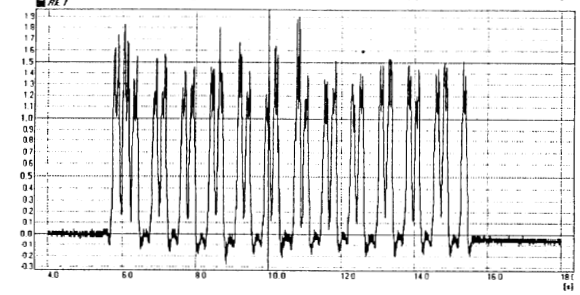

c) The vertical acceleration of the rail $\ddot{w}_R(t)$

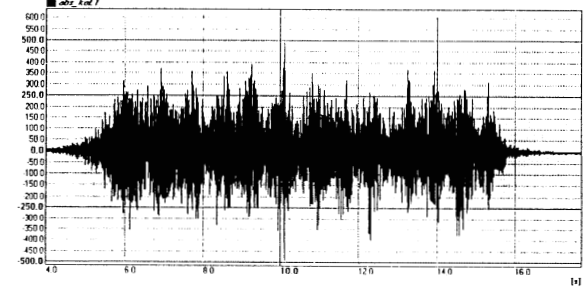

d) The vertical displacement of the sleeper $w_S(t)$, the filtered signal for $f \in (0-20Hz)$

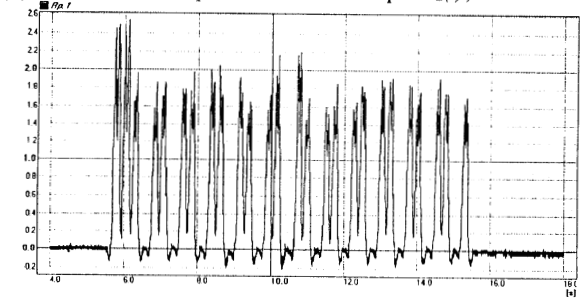

e) The vertical acceleration of the sleeper $\ddot{w}_S(t)$

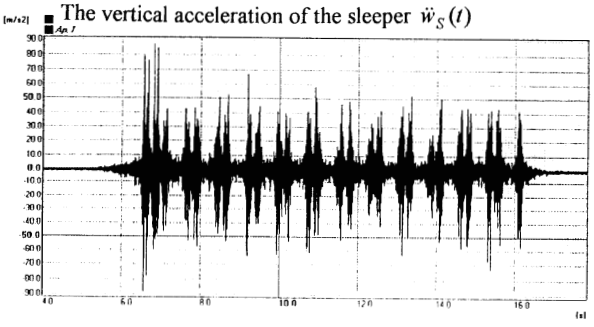

Obr. 4. Časové priebehy meranej vertikálnej odozvy trate pri prejazde osobného vlaku meraným priamym traťovým úsekom, c = 115 km
Fig. 4. Time histories of the measured vertical track response for the passenger train passage in a straight track section (out of rail welds) of the line, c = 115 km/h

***Teplička III/2000** / The time history of the vertical track response for **the freight train passage** in a straight track section (out of rail welds), c=57 km/h,.*

a) The direct dynamic interaction force a rail – a sleeper $F_{R\text{-}S}$(t)

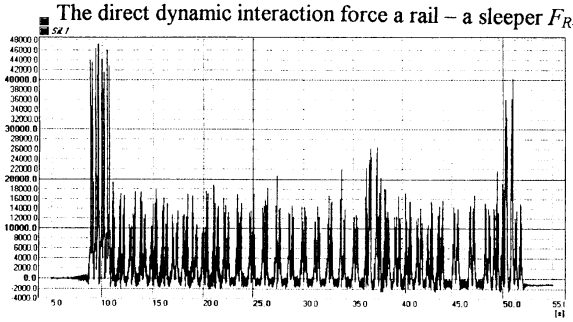

b) The vertical displacement of the rail $w_R(t)$, the filtered signal for $f \in (0-20Hz)$

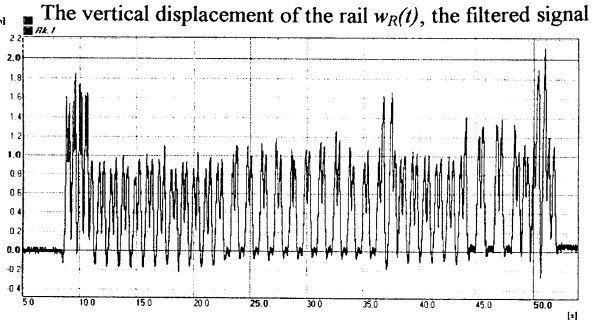

c) The vertical acceleration of the rail $\ddot{w}_R(t)$

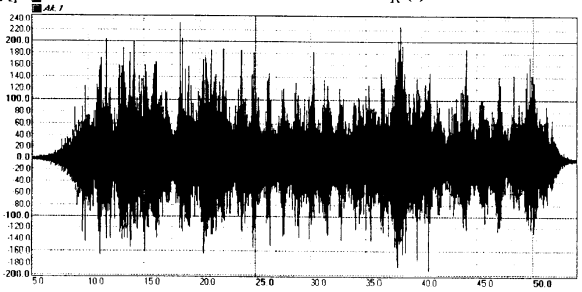

d) The vertical displacement of the sleeper $w_S(t)$, the filtered signal for $f \in (0-20Hz)$

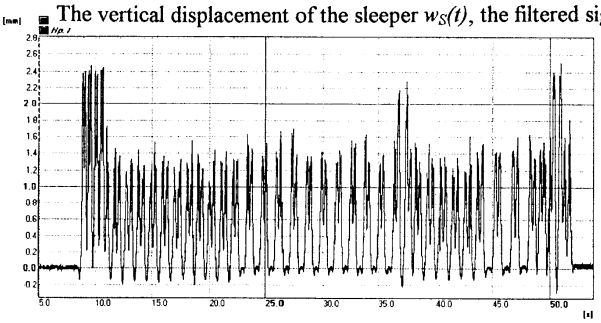

e) The vertical acceleration of the sleeper $\ddot{w}_S(t)$

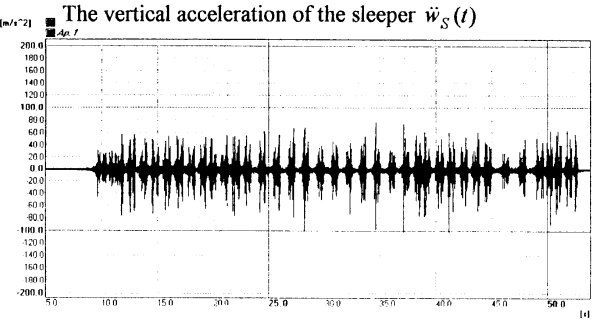

Obr. 5. Časové priebehy meranej vertikálnej odozvy trate pri prejazde nákladného vlaku v meranom priamom úseku trate, c = 57 km/h
Fig. 5. Time histories of the measured vertical track response for the freight train passage in a measured straight track section (out of rail welds) of the line, c = 57 km/h

rýchlosť $c = 115$ km/h. Vzorkovacia frekvencia $f_s = 100$ Hz. Frekvenčná analýza zodpovedá nízkofrekvenčnej odozve trate pre $f \in (0 - 100$ Hz). Na obr. 6 sú prezentované vybrané priemerované spektrá odozvy zodpovedajúce prejazdu celého vlaku. Na obr. 7 a obr. 8 sú ukázané okamžité spektrá vybraných časových okien odpovedajúcich prejazdu lokomotívy a charakteristických podvozkov prejazdu meraného vlaku. Aplikovaná je analýza záznamov využitím modulu analýzy BK systému.

4.2. Stredne frekvenčná analýza odozvy trate

Analyzovaný je prejazd rovnakého osobného vlaku prechádzajúceho priamym úsekom trate ako v kap. 4.1, rýchlosť $c = 115$ km/h. Vzorkovacia frekvencia $f_s = 1600$ Hz. Frekvenčná analýza je aplikovaná na oblasť stredných frekvencií odozvy $f \in (1 - 800$ Hz). Na obr. 9 a obr. 10 sú prezentované okamžité spektrá vybraných časových okien zodpovedajúcich prejazdu podvozku lokomotívy a podvozkov vagónov meraným miestom. Aplikovaný je modul analýzy BK systému.

5. Závery

Cieľom experimentálnych meraní bolo hodnotenie dynamickej reakcie koľajníc, podvalov a interakčných síl koľajnica/podval pri prejazde vlakov v prevádzkových podmienkach. V príspevku sú prezentované niektoré výsledky meraní a ich analýza pre prejazdy osobného vlaku.

- *Časové záznamy vertikálnej odozvy komponentov trate* – koľajníc, podvalov a interakčnej sily koľajnica–podval, ktoré dávajú základnú informáciu o vplyve dynamického zaťaženia na reakciu týchto komponentov. Ukazujú celkový vplyv prejazdu lokomotívy a osobných vagónov na dynamickú odozvu týchto komponentov. Zvolená vzorkovacia frekvencie f_s meraných signálov a rýchlosť prechádzajúcich vlakov sú hlavné faktory ovplyvňujúce amplitúdy meraných zrýchlení. Pre vzorkovaciu frekvenciu $f_s = 100$ Hz a rýchlosť vlakov $c = 100 \div 130$ km/h (osobné vlaky) amplitúdy vertikálnej odozvy dosahujú hodnoty:
  - Vertikálne zrýchlenia koľajnicových pásov $w_r \approx 150 - 350$ m/s^2.
  - Vertikálne zrýchlenia podvalov $w_s = 50 - 90$m/s^2.
  - Vertikálne zrýchlenia povrchu štrkového lôžka $w_b = 0{,}2$ až 2 m/s^2.

  Pre vzorkovaciu frekvenciu $f_s = 100$ Hz a pre rýchlosť pohybu vlakov $c = 100 \div 130$ km/h sa tieto hodnoty redukujú približne 12-krát.
  - Amplitúdy vertikálnej interakčnej sily $F_{R\text{-}S} \approx 40 - 60$ kN.

  Pre vzorkovaciu frekvenciu $f_s = 1000$ Hz a rýchlosť pohybu vlakov $c = 40 \div 60$ km/h (nákladné vlaky) amplitúdy vertikálnych zrýchlení sú tiež redukované.

  Potom pre dobre udržiavanú trať sú vplyv rýchlosti a kvalita koľajových vozidiel najdôležitejšie faktory ovplyvňujúce dynamické chovanie systému vozidlo/trať.

sented. Sampling frequency $f_s = 1000$ Hz. The frequency analysis is made for low frequencies of the response, $f \in \langle 0 - 100$ Hz$\rangle$. In Fig. 6 there are chosen average spectra corresponding to the passage of the whole passenger train. In Figs. 7 and 8 there are instantaneous spectra of the chosen time windows corresponding to the passage of the locomotive and characteristic bogies of the measured passenger train. The analyser modulus of the BK system is applied.

4.2. The mid-frequency analysis of the track response

The same passenger train passage in a straight track section (out of rail welds), as in chapter 4.1, speed $c = 115$ km/h, is analysed. Sampling frequency $f_s = 1600$ Hz. The frequency analysis is made for mid frequencies of the response $f \in \langle 1 - 800$ Hz$\rangle$. In Figs. 9 and 10 there are instantaneous spectra of the chosen time windows corresponding to the passage of the locomotive bogie and the coach bogie through a measurement site. The analyser modulus of the BK system is applied.

5.Conclusion

The purpose of experimental measurements was to assess dynamic behaviour of the rail, sleepers and the interaction force the rail – the sleeper under the passage of trains in operational conditions. In this paper are presented some results of the measurement and their analysis for the typical passenger train passage only.

- *Time histories of the vertical response of track components* – rails, sleepers and the interaction force the rail – the sleeper, that give the basic information about the effect dynamic load on behaviour of these components. They show a total effect of the locomotive and coaches on the dynamic response of these components.
  The chosen sampling frequency fs of the measured signals and the train speed influence absolute values of the measured acceleration considerably. For the sampling frequency $f_s = 1000$ Hz and the train speed $c = 100 \div 130$ km/h (passenger trains) peaks of the vertical response reach value:
  - Peaks of the vertical rail accelerations reach values $\ddot{w}_R \approx 150 - 350$ m/s^2,
  - Peaks of the vertical sleeper accelerations reach values $\ddot{w}_S \approx \approx 50 - 90$m/s^2,
  - Peaks of the vertical ballast accelerations reach values $\ddot{w}_b \approx \approx 0{,}2 - 2$ m/s^2,

  For the sampling frequency $f_s = 100$ Hz and the train speed $c = 100 \div 130$ km/h these peak values are reduced approximately 12 time.
  - The vertical peak interaction forces reach values $F_{R\text{-}S} \approx 40 - 60$ kN.

  For the sampling frequency $f_s = 1000$ Hz and the train speed $c = 40 \div 60$ km/h (freight trains) vertical acceleration peaks of the response are reduced. Then on a well maintained track the train speed and a quality of vehicles are the most important factors affecting the dynamic behaviour of the vehicle/track system.

Teplička III/2000 / *The vertical track response for the passenger train passage in a straight track section (out of rail welds), c=115 km/h,.*

Analysis for the passage of the whole train - *the low-frequency analysis* $f \in \langle 1-100Hz \rangle$

Vertical interaction force the rail – the sleeper $F_{R\text{-}S}$

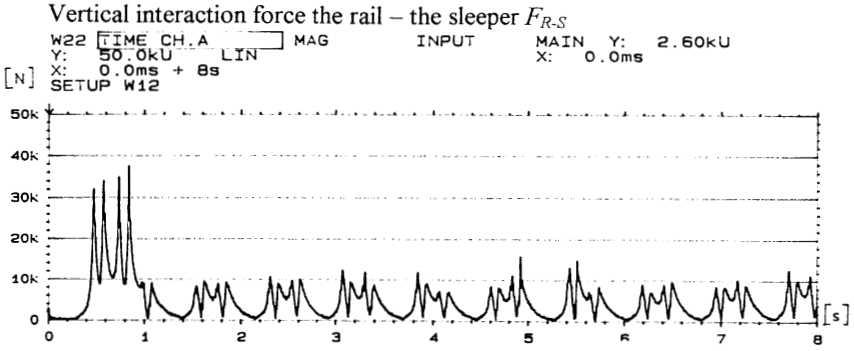

Frequency spectrum of the vertical interaction force the rail – the sleeper $F_{R\text{-}S}$

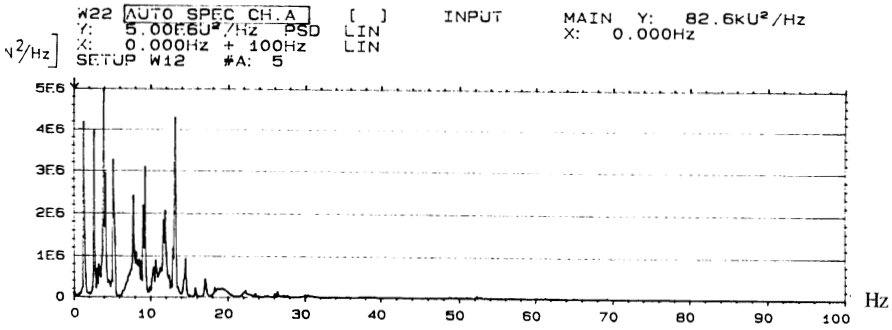

Vertical acceleration of the rail $\ddot{w}_R(t)$

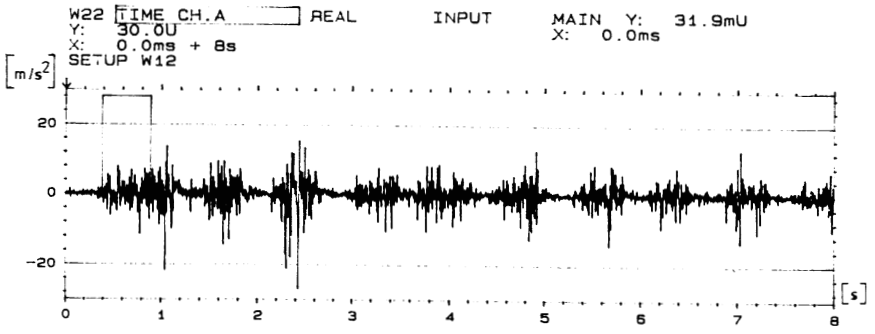

Frequency spectrum of the vertical acceleration of the rail $\ddot{w}_R(t)$

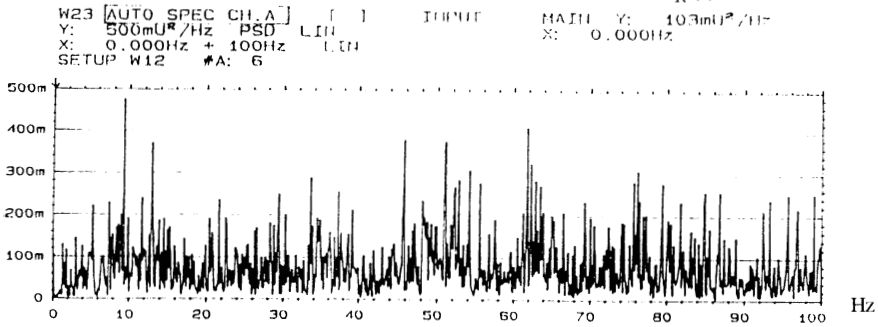

Vertical acceleration of the sleeper head $\ddot{w}_S(t)$

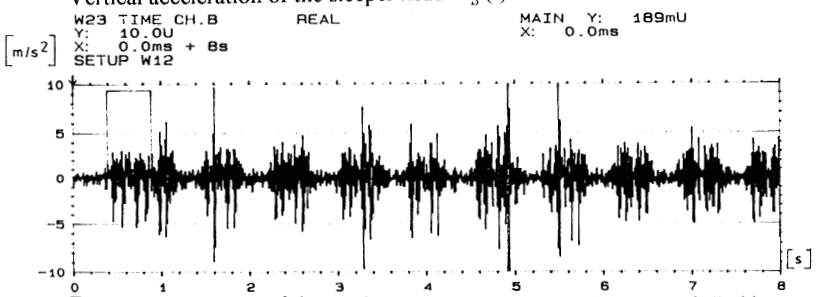

Frequency spectrum of the vertical acceleration of the sleeper head $\ddot{w}_S(t)$

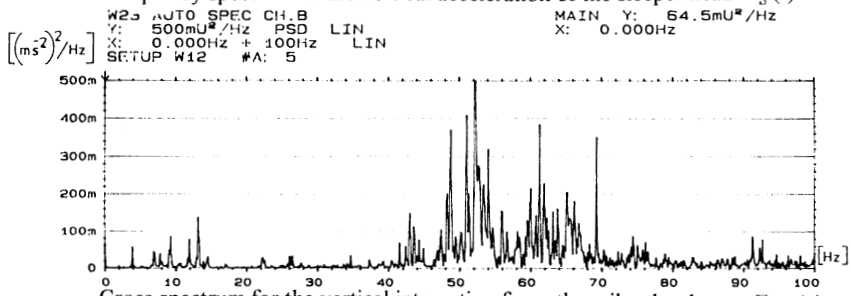

Cross spectrum for the vertical interaction force the rail – the sleeper $F_{R\text{-}S}$ / the vertical acceleration of the sleeper head $\ddot{w}_S(t)$

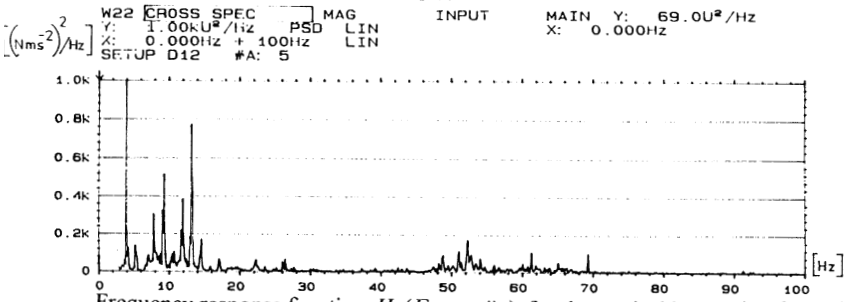

Frequency response function $H_1(F_{R-S} - \ddot{w}_s)$ for the vertical interaction force the rail – the sleeper $F_{R\text{-}S}$ / the vertical acceleration of the sleeper head $\ddot{w}_S(t)$

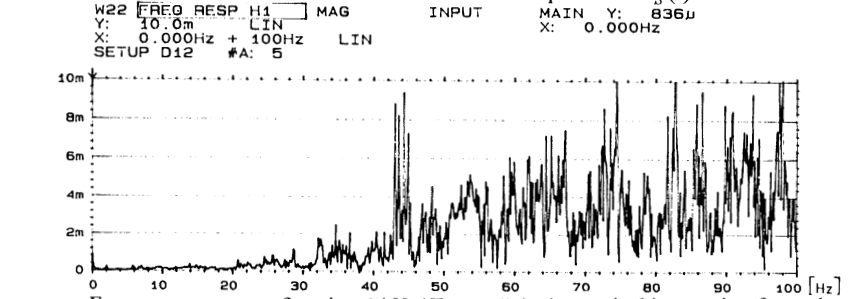

Frequency response function $1/H_1(F_{R-S} - \ddot{w}_s)$ the vertical interaction force the rail – the sleeper $F_{R\text{-}S}$ / the vertical acceleration of the sleeper head $\ddot{w}_S(t)$

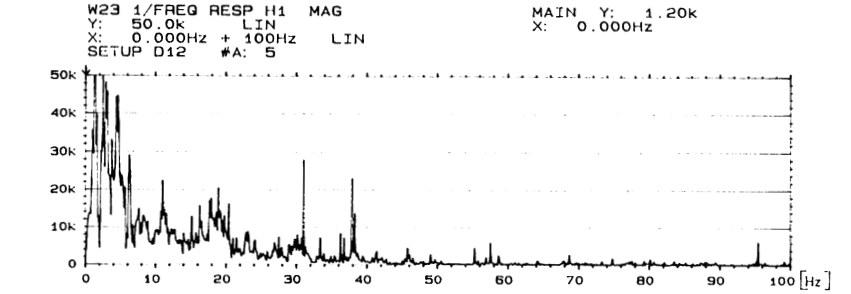

Obr. 6. Priemerované spektrá odozvy zodpovedajúce prejazdu celého vlaku, c = 115 km/h.
Fig. 6. Average spectra corresponding to the whole passenger train passage, c = 115 km/h

Teplička III/2000 */ The vertical track response for the passenger train passage in a straight track section (out of rail welds), c=115 km/h,.*

Analysis for the passage of the locomotive L350/85t *- the low-frequency analysis* $f \in \langle 1-100Hz \rangle$

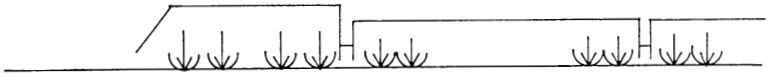

Vertical interaction force the rail – the sleeper $F_{R\text{-}S}$

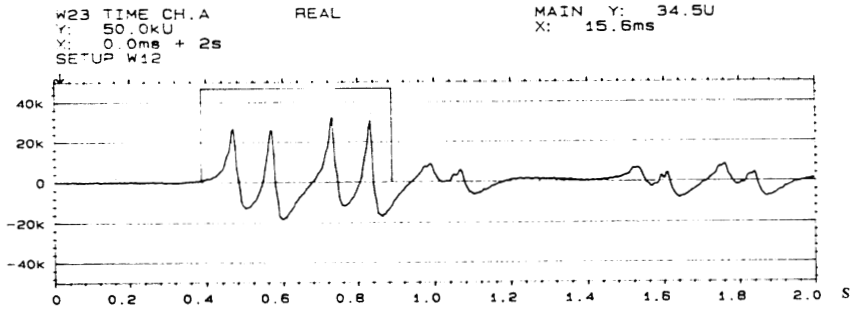

Frequency spectrum of the vertical interaction force the rail – the sleeper $F_{R\text{-}S}$

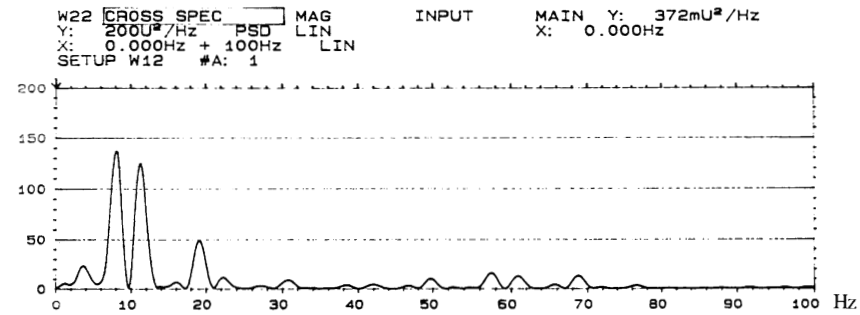

Vertical acceleration of the rail $\ddot{w}_R(t)$

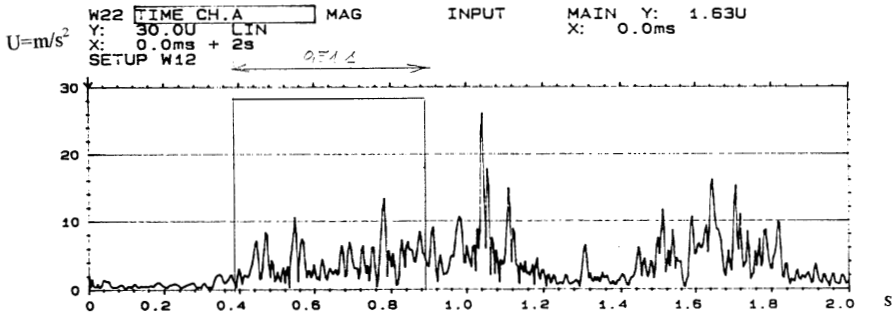

Frequency spectrum of the vertical acceleration of the rail $\ddot{w}_R(t)$

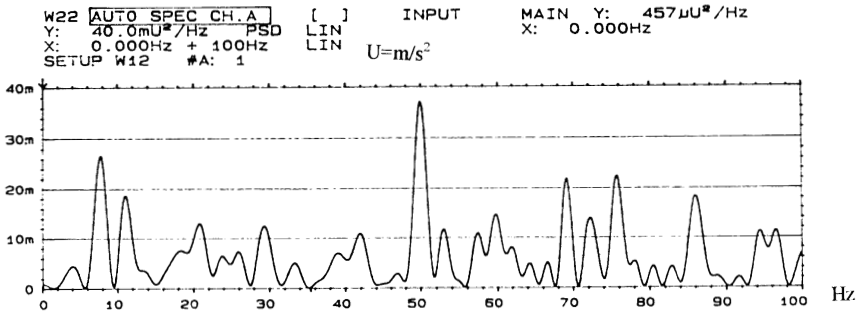

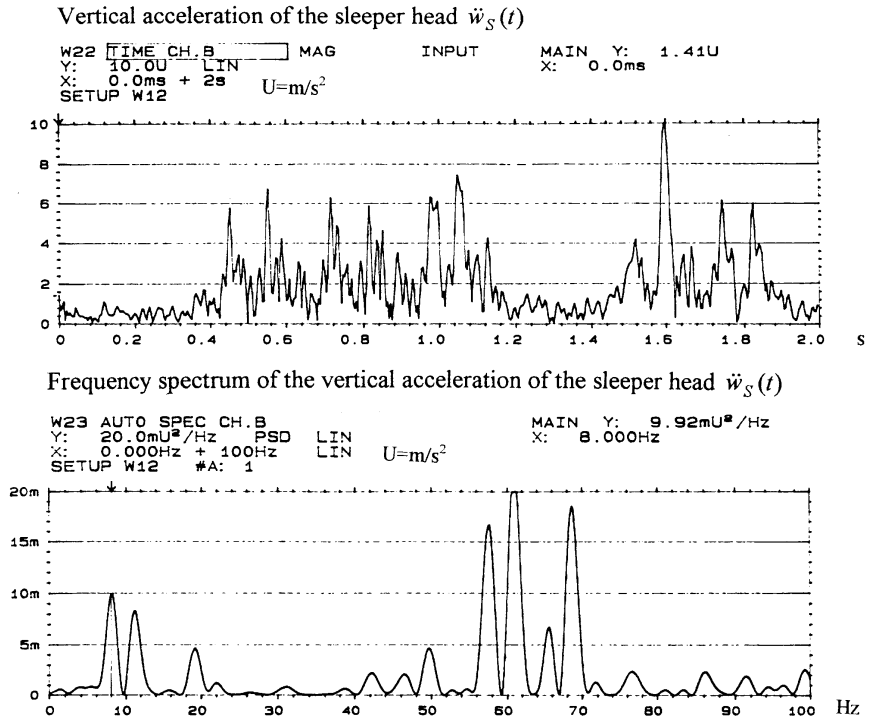

Obr. 7. Okamžité spektrá vybraných časových okien zodpovedajúcich prejazdu lokomotívy.
Fig. 7. Instantaneous spectra of the chosen time windows corresponding to the passage of the locomotive

- Premiestnenia merané na koľajových pásoch a podvaloch potvrdzujú, že nápravy a podvozky prechádzajúcich vozidiel sú jasne identifikovateľné a sú proporcionálne dynamickým zaťažením vozidiel.

- Frekvenčná analýza zaznamenaných signálov dáva podrobné informácie o kmitaní komponentov trate a dáva obraz o koncentrácii energie na frekvenčné zložky. Pokiaľ dominantná frekvenčná skladba dynamických síl a priehybov koľajníc a podvalov zodpovedá nízkym frekvenciám $f \in$ (1 - 20 Hz), frekvenčná skladba zrýchlenia kmitania leží v oveľa širšej oblasti. Pritom stredné frekvencie zrýchlení kmitania v oblasti 100 Hz ÷ 500 Hz hrajú dôležitú úlohu v dynamike tratí.

- Frekvenčná analýza pre nízke frekvencie odozvy, $f \in$ (1 - 100 Hz):
  - Zrýchlenie vertikálneho kmitania koľajnicových pásov $\ddot{w}_R(t)$ má kvázi diskrétne spektrum (spriemerované spektrá) rozdelené takmer rovnomerne, bez výrazných špičiek.
  - Zrýchlenie kmitania podvalov $\ddot{w}_S(t)$ má tiež kvázi diskrétne spektrum ale rozdelené nerovnomerné s vrcholmi v oblasti frekvencií $f_{(1)} \approx 10$ Hz a $f_{(2)} \approx 50 \div 60$ Hz.
  - Okamžité spektrá zodpovedajúce vybraným časovým oknám zrýchlenia koľajníc $\ddot{w}_R(t)$ a zrýchlenia podvalov $\ddot{w}_S(t)$ pre prejazd lokomotívy a podvozkov vagónov potvrdzujú výsledky analýzy prejazdu celého vlaku.

- Frekvenčná analýza pre stredné frekvencie odozvy, $f \in$ (1 - 800 Hz):

- The displacements measured on rails and sleepers showed that individual axles and bogies of passage vehicles are clearly distinguished in displacement records and that they are proportional to the dynamic wheel load of passage vehicles.
- *The frequency analysis* of recorded signals gives comprehensive information about the track component vibration and gives a picture of concentration of the energy on frequency components. While the dominant frequency composition of interaction forces and deflection of rails and sleepers corresponds to a low frequency range, say to $f \in \langle 1 - 20 \text{ Hz} \rangle$, the frequency content of accelerations of these motions lies in a much wider frequency range. At the same time the mid-frequency range between 100 Hz ÷ 500 Hz plays an important role in the track dynamics. In this frequency range the track components – sleepers, pads, ballast and subsoil have a strong influence on the track system behaviour.
- *The frequency analysis for low frequencies of the response,* $f \in \langle 1 - 100 \text{ Hz} \rangle$:
  - The vertical rail acceleration $\ddot{w}_R$ has a quasi discrete spectrum (average spectrum) distributed in a nearly uniform way.
  - The vertical sleeper acceleration $\ddot{w}_S$ has a quasi discrete spectrum distributed in a non-uniform way with peaks at the frequencies $f_{(1)} \approx 10$ Hz and $f_{(2)} \approx 50 - 60$ Hz.
  - Instantaneous spectra of the chosen time windows of the rail acceleration $\ddot{w}_R$ and the sleeper acceleration $\ddot{w}_S$, corresponding to the passage of the locomotive and characteristic bogies of passenger trains, confirm the analysis results for the passage of the whole train.
- *The frequency analysis for mid frequencies of the response,* $f \in \langle 1 - 800 \text{ Hz} \rangle$:

***Teplička III/2000** / The vertical track response for the passenger train passage in a straight track section (out of rail welds), c=115 km/h,.*

***Analysis for the passage of characteristic coach bogies** - the low-frequency analysis* $f \in \langle 1-100Hz \rangle$

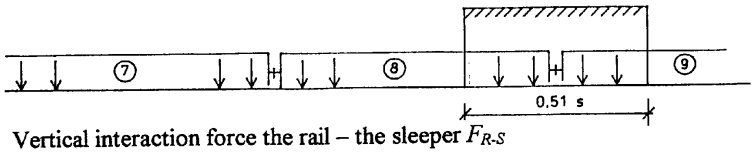

Vertical interaction force the rail – the sleeper $F_{R\text{-}S}$

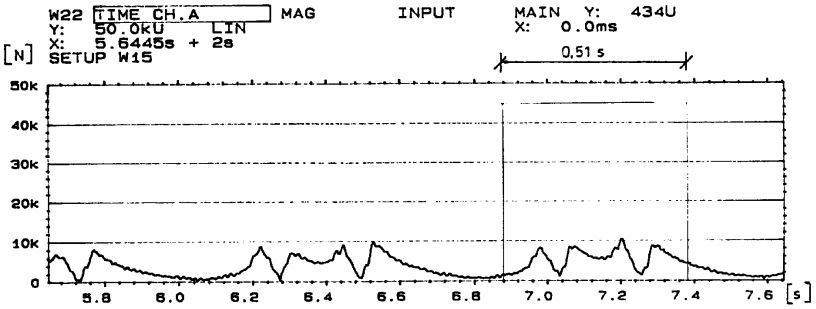

Frequency spectrum of the vertical interaction force the rail – the sleeper $F_{R\text{-}S}$

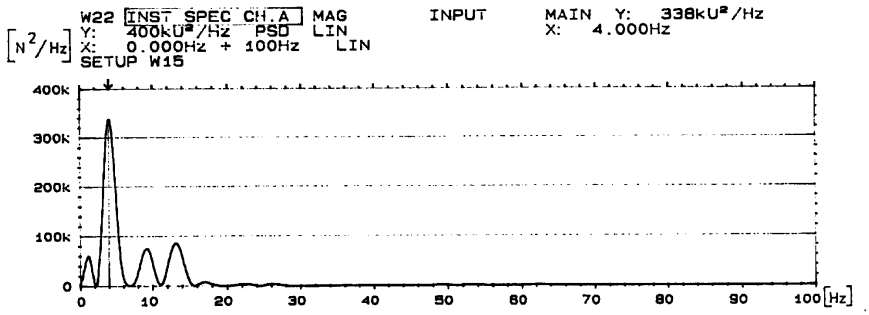

Vertical acceleration of the rail $\ddot{w}_R(t)$

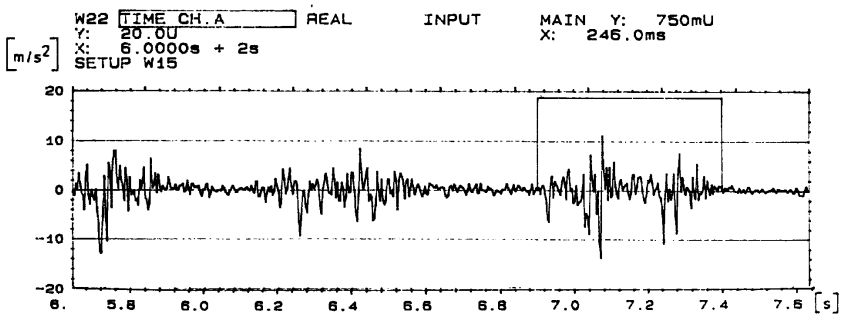

Frequency spectrum of the vertical acceleration of the rail $\ddot{w}_R(t)$

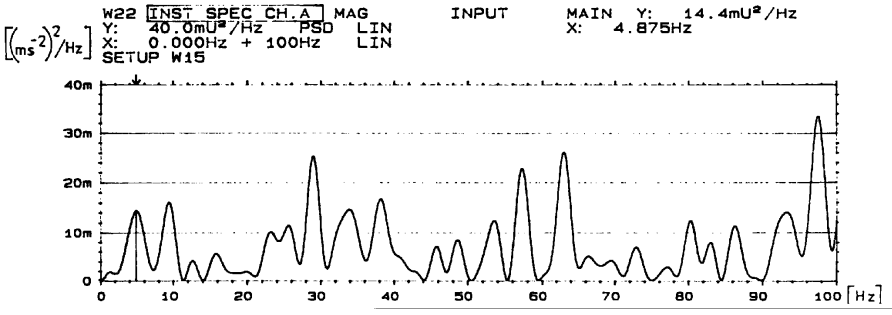

Vertical acceleration of the sleeper head $\ddot{w}_S(t)$

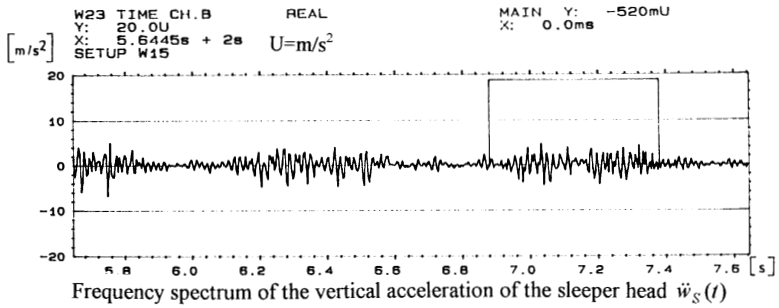

Frequency spectrum of the vertical acceleration of the sleeper head $\ddot{w}_S(t)$

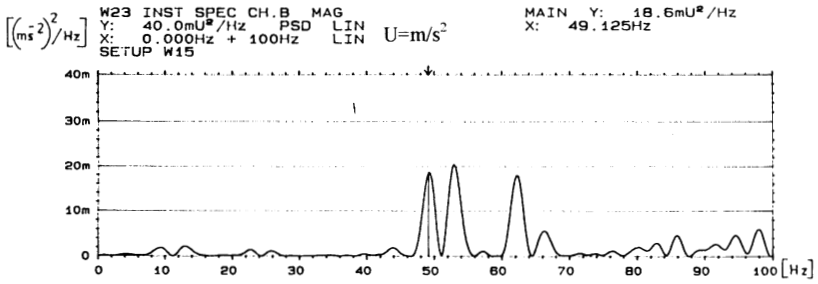

Frequency response function $H_1(F_{R-S} - \ddot{w}_s)$ for the vertical interaction force the rail – the sleeper $F_{R\text{-}S}$ / the vertical acceleration of the sleeper head $\ddot{w}_S(t)$

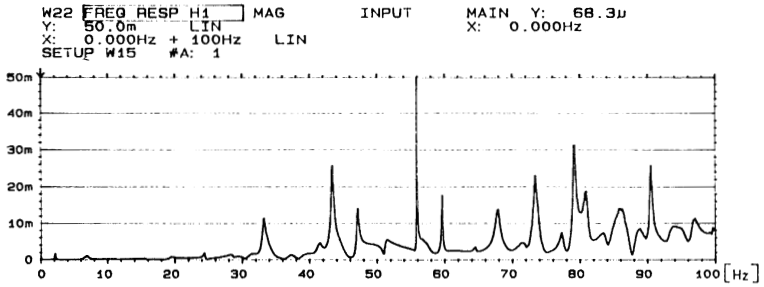

Frequency response function $1/H_1(F_{R-S} - \ddot{w}_s)$ the vertical interaction force the rail – the sleeper $F_{R\text{-}S}$ / the vertical acceleration of the sleeper head $\ddot{w}_S(t)$

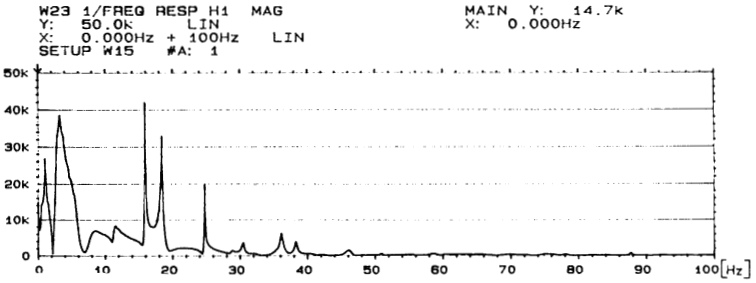

Frequency response function $H_1(F_R - \ddot{w}_s)$ for the vertical acceleration of the rail $\ddot{w}_R(t)$ – the vertical acceleration of the sleeper head $\ddot{w}_S(t)$

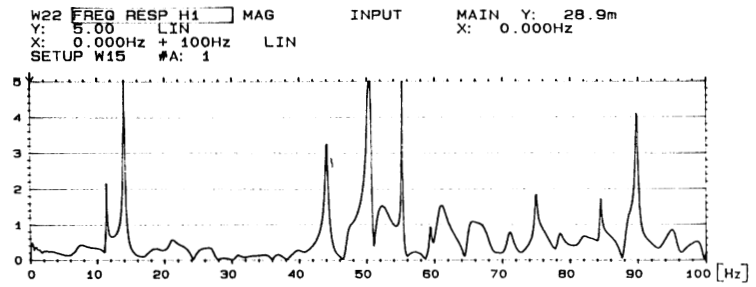

Obr. 8. Okamžité spektrá vybraných časových okien zodpovedajúce prejazdu charakteristických podvozkov vagónov osobného vlaku
Fig. 8. Instantaneous spectra of the chosen time window corresponding to the passage of characteristic coach bogies of the passenger train

***Teplička III/2000** / The vertical track response for the passenger train passage in a straight track section (out of rail welds), c=115 km/h,.*
***Analysis for the passage of characteristic locomotive bogies** - the mid-frequency analysis*
$f \in \langle 1-800Hz \rangle$

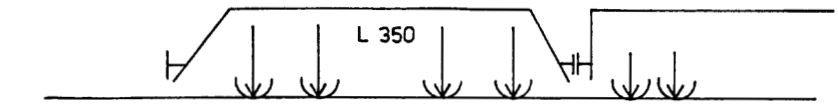

Vertical acceleration of the rail $\ddot{w}_R(t)$

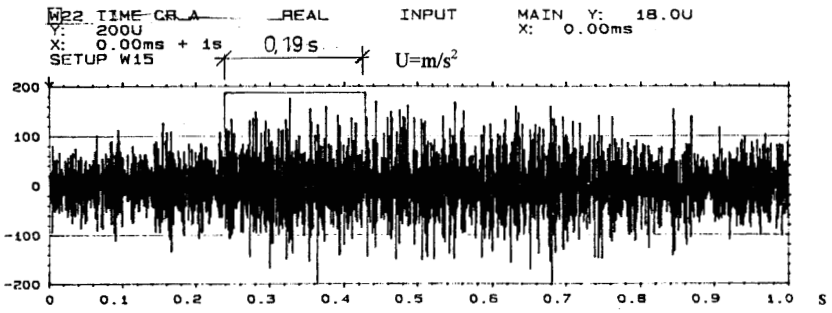

Vertical acceleration of the sleeper head $\ddot{w}_S(t)$

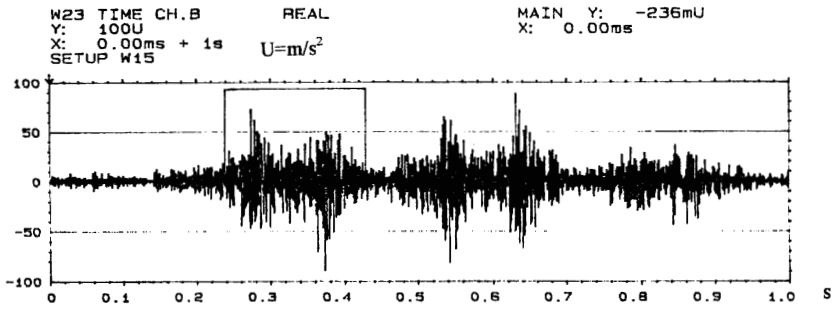

Frequency spectrum of the vertical acceleration of the rail $\ddot{w}_R(t)$

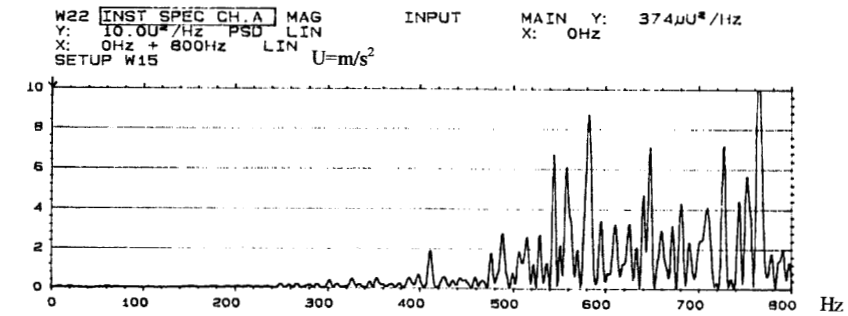

Frequency spectrum of the vertical acceleration of the sleeper head $\ddot{w}_S(t)$

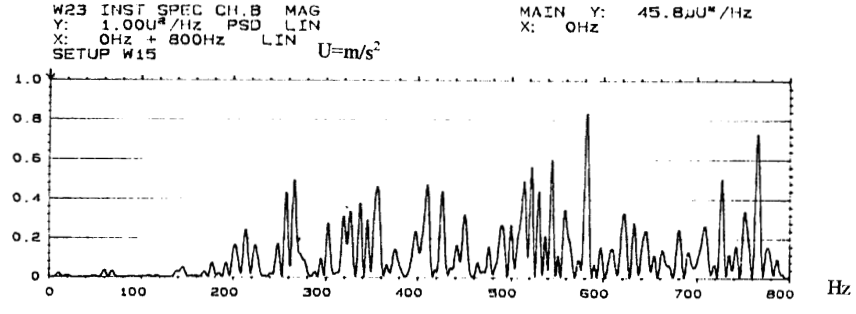

Obr. 9. Okamžité spektrá vybraného časového okna zodpovedajúceho prejazdu podvozku lokomotívy
Fig. 9. Instantaneous spectra of the chosen time window corresponding to the passage of the locomotive bogie

***Teplička III/2000** / The vertical track response for the passenger train passage in a straight track section (out of rail welds), c=115 km/h,.*
***Analysis for the passage of characteristic coach bogies** - the mid-frequency analysis* $f \in \langle 1-800Hz \rangle$

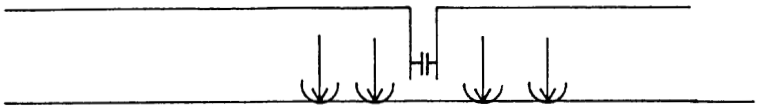

Vertical acceleration of the rail $\ddot{w}_R(t)$

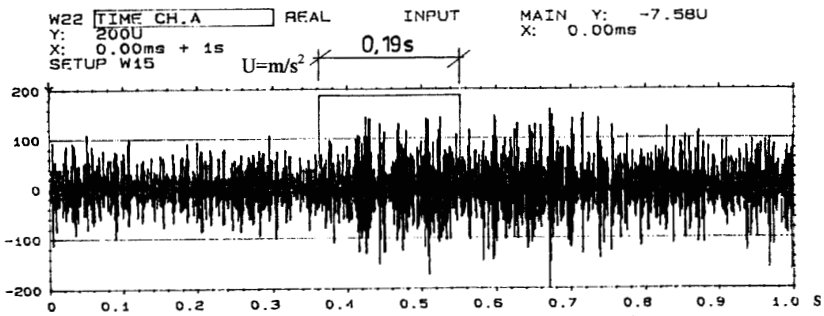

Vertical acceleration of the sleeper head $\ddot{w}_S(t)$

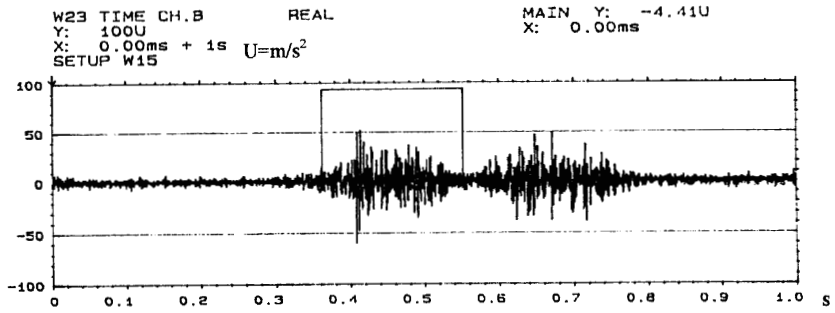

Frequency spectrum of the vertical acceleration of the rail $\ddot{w}_R(t)$

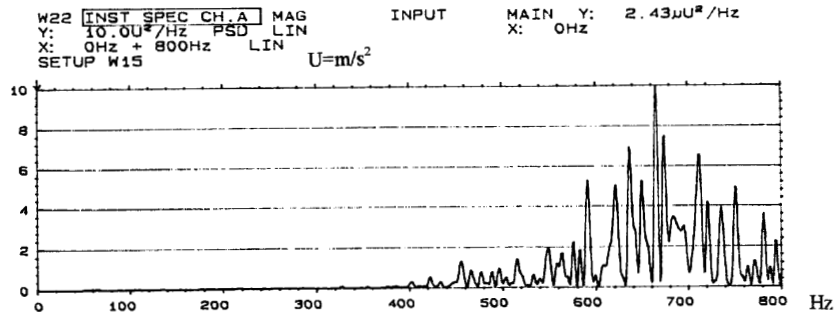

Frequency spectrum of the vertical acceleration of the sleeper head $\ddot{w}_S(t)$

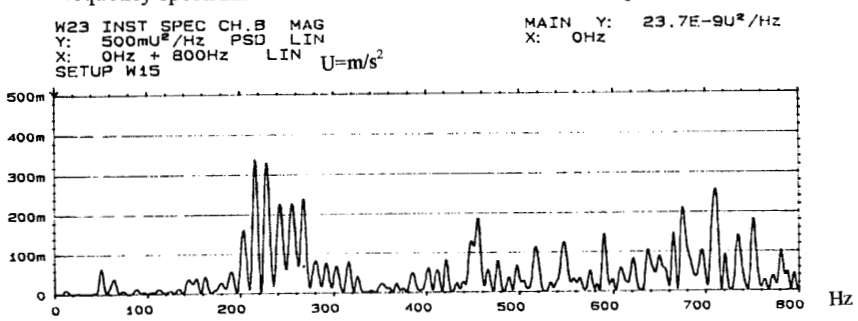

Obr. 10. Okamžité spektrá vybraného časového okna zodpovedajúceho prejazdu charakteristických podvozkov osobných vagónov
Fig. 10. Instantaneous spectra of the chosen time window corresponding to the passage of the characteristic coach bogie of the passenger train

- Okamžité spektrá vybraných časových okien zrýchlenia kmitania koľajníc $\ddot{w}_R(t)$ majú tiež kvázi diskrétne spektrum s dominantnými zložkami na frekvenciách v oblasti $f \approx 600 \div 700$ Hz.
- Okamžité spektrá vybraných časových okien zrýchlenia kmitania podvalov $\ddot{w}_S(t)$ má tiež diskrétne spektrum s dominantnými frekvenciami v pásme $f_{(2)} \approx 400 \div 700$ Hz.

- Instantaneous spectra of the chosen time windows of the vertical rail acceleration $\ddot{w}_R$ have a quasi discrete spectrum (average spectrum) with dominant components on frequencies $f \approx 600$ – 7 00 Hz.
- Instantaneous spectra of the chosen time windows the sleeper acceleration $\ddot{w}_S$ have a quasi discrete reduced spectrum with dominant components on frequencies $f_{(1)} \approx 200$ – 300 Hz and distributed in a nearly uniform way for $f_{(2)} \approx 400$ – 700Hz.

Literatúra – References

[1] *Dual Channel Signal Analyser BK Type 2032*, B&K Denmark 1987.
[2] RANDALL, R. B., TECH, B.: *Frequency analysis,* B&K Manual.
[3] MORAVČÍK, M.: *Experience in railway track testing for validation of theoretical dynamic analysis.* Proc. Communication on the edge of millenniums, EDIS Žilina 1998.
[4] MORAVČÍK, M.: *Vertical Dynamic Vehicle/Track Interaction - Simulation and experimental testing.* Proc. MTU Dnepropetrovsk 2000, Vol.6.

Marek Kopiński – Andrzej Surowiecki *

LABORATÓRNE SKÚŠKY ZLOŽIEK SPEVNENEJ ZEMINY V ICH INTERAKČNEJ OBLASTI

LABORATORY TESTS OF THE INTERACTION ZONE BETWEEN REINFORCED SOIL COMPONENTS

V príspevku sa píše o výsledkoch laboratórneho skúmania zameraného na rozsah oblasti vzájomného pôsobenia v prostredí nesúdržných zemín a zvislo umiestnených výstuží. Skúmanie spočívalo v meraní bočného tlaku sústavy; vykonávalo sa na veľkorozmerných modeloch podložia (piesok, štrk, hrubozrnný pieskovec) s výstužou v tvare kovových alebo plastových sietí. Bolo dokázané, že rozsah oblasti výstuže v zvislom smere závisí od vlastností pôdneho prostredia a parametrov výstuže.

Laboratory investigation results related to the range of the interaction zone between a non-cohesive soil medium and vertically positioned reinforcement inserts are discussed. The investigations consisted of the measurement of the composite's side pressure; they have been carried out on large-scale models of subsoil (sand, gravel, grit) with reinforcements in the form of metal and plastic nets. It has been proved that the vertical range of the reinforcement effect zone depends upon characteristics of the soil medium and reinforcement parameters.

1. Introduction

For about 30 years, reinforced soil has been used in civil engineering throughout the world, for example, as the construction material for retaining walls erected under specific conditions. Modern solutions of reinforced-soil retaining structures vary, depending on types of wall elements and reinforcement inserts employed [1], [2]. As early as at the first stage of experiments with reinforced soil, back in sixties [8], interest awoke to the complex of caňuses and effects that result in the initiation and development of interaction of loose medium with reinforcement inserts. Successive investigations and theoretical analyses [4], [5], [6] led to the mathematical formulation of the so-called anisotropic cohesion, i.e. the local strengthening, which stabilizes a non-cohesive medium due to the effect of reinforcement.

Friction between the medium and reinforcement, due to its fundamental role in the reinforced soil operation, has been the subject of experimental and theoretical investigations for over 20 years [8]. The investigations are continued, and now they not only relate to how friction depends on the type of filling soil, but also to the mechanical aspect of the soil-reinforcement interaction [11].

Investigations on the recognition of factors affecting the reinforcement insert-granular soil interaction [9], [10], [11] have been undertaken at the Wrocław University of Technology. The occurrence of a medium strengthened locally in the vicinity of reinforcement inserts implies the existence of an area of reinforcement-medium interaction. The "interaction zone" is the area of reinforced medium subjected to external load, in which a decrease in deformability occurs with respect to the deformability of the reference medium, i.e. a medium with no reinforcement. If we assume that the interaction zone encompasses the whole range of the reinforced medium sample being discussed, the sample can be regarded as a homogeneous material from the standpoint of its operation (if no slipping occurs at the reinforcement-medium interface). The "interaction zone" is closely connected with the concept of the so-called "optimum separation" of parallel reinforcement layers. The optimum separation of reinforcement layers is defined as the vertical distance between reinforcement planes which ensures the highest effectiveness of reinforcement operation possible, i.e. the greatest attainable reduction in vertical and horizontal deformations of the reinforced medium sample.

No paper has been published over the last 30 years regarding the optimization of reinforcement layer separation and the separation's relation to the range (size) of the "interaction zone". A schematic representation of the concept of the so-called "optimum separation of reinforcement layers" can be found in the manual [3], but this by no means exhausts the issue, being only limited to a diagram and a short comment lacking not only any analytical formulae, but also a specification of factors that influence the value of "optimum separation". This, however, was not the aim of the manual mentioned.

There is a general consent between the authors of national leading publications on the subject that appeared in the last decade (e.g. [3], [7]) that in spite of wide-spread practical application of

* **Dr. hab. inž. Andrzej Surowiecki,** Institute of Civil Engineering, Wrocław University of Technology, Wyb. Wyspiańskiego 27, 50-370 Wrocław, Poland; T. Kosciuszko Military University, Dept. of Military Engineering, Czajkowskiego 101, 51-151 Wroclaw; Agriculture University of Wroclaw, Institute of Building and Landscape Architecture, Pl. Grundwaldzki 24, 50-363 wroclaw, Poland; E-mail: mr@biskupin.wroc.pl
Dr Ing. Marek Kopiński, Institute of Civil Engineering, Wrocław University of Technology, Wyb. Wyspiańskiego 27, 50-370 Wrocław, Poland

reinforced soil worldwide and extensive investigation performed, some mechanisms of reinforced-soil structure operation are still not completely understood. The paper [7] stresses the absence of rational methods of internal dimensioning applicable to reinforced soil structures, as well as the lack of generally recognized design standards – because of insufficient scientific exploration of reinforced soil.

The presented paper constitutes an experimental attempt at the recognition of interaction conditions of the reinforced soil components. There are discussed the results of model research conducted by the author in order to determine the effect of the factors selected (type and arrangement of reinforcement inserts, kind of loose soil medium, i.e. size of grains, degree of medium consolidation) on the vertical range of the spatial zone of reinforcement-loose soil medium interaction.

The size of "interaction" zone and optimum reinforcement layer separation has been determined based on the measurement of horizontal pressure exerted by load-subjected samples of soil. Also experimental strength parameters have been calculated for the reinforced medium samples.

2. Measurement procedure

The investigation was carried out using full-scale laboratory models. A diagram of the experimental stand is shown in Fig. 1. Reinforced medium samples (models) were placed in a rectangular steel container whose planar dimensions were 0.54 × 0.54 m and its height was 0.42 m. The design of the container's walls and bottom allowed for the measurement of soil medium pressure. The values of side and vertical pressures of the medium on the subsoil being modeled were controlled by means of installed mechanical pressure gauges with elastic bands having a known elastic constant as their main sensing parts.

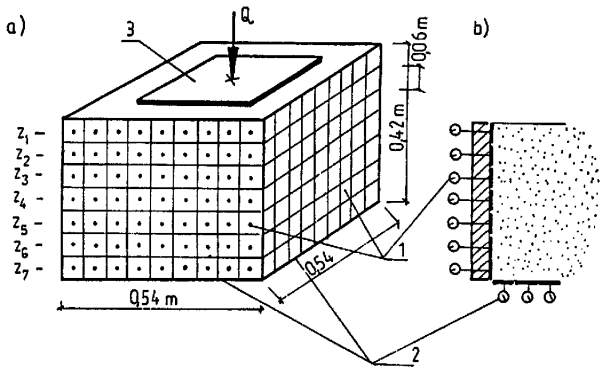

Fig. 1. Diagram and basic parameters of experimental setup: a – general view; b – vertical cross-section through soil container wall; 1 – mechanical sensor of horizontal pressure; 2 – mechanical sensor of vertical pressure; 3 – loading plate 0.31 × 0.31 m; z_1 = 0.03 m; z_2 = 0.09 m; z_3 = 0.15 m; z_4 = 0.21 m; z_5 = 0.27 m; z_6 = 0.33 m; z_7 = 0.39 m (measuring levels)

Belts with the elastic constant C_s = 8 MN.m^{-3} were installed for the sensors located in the container's walls, while those with the elastic constant C_p = 80 MN.m^{-3} for the bottom sensors. Since the elastic bands are exchangeable, modifications of elastic susceptibility of the sensing parts in the container walls and bottom are possible.

The models were subjected to vertical and central load characterized by the unit pressure q within the range from 0 to 0.24 MPa. The reinforcement applied had the form of nets arranged horizontally, that is normally to the load plane, according to the principle of maximum work effectiveness for the inserts. Principally, steel nets with the 12-by-12-mm square mesh (symbol S 12) were used. Partial stiffness of the net's knots resulted from the spatial layout of the nets – the interaction of this type of inserts with soil medium is determined by:

- friction between soil and reinforcement,
- shearing of soil medium (delamination) for the bars directed crosswise in the direction of horizontal forces (in this case, a resistance to the reinforcement's transverse displacement due to the deformation of the load-subjected layer of the composite occurs, depending, among other things, on the degree of spatial shaping of the net).

For comparison purposes, other types of nets were also used, e.g. plastic nets. The models were reinforced with a single, double and triple nets. The following variable parameters were assumed:

- arrangement of the nets,
- consolidation of the soil medium.

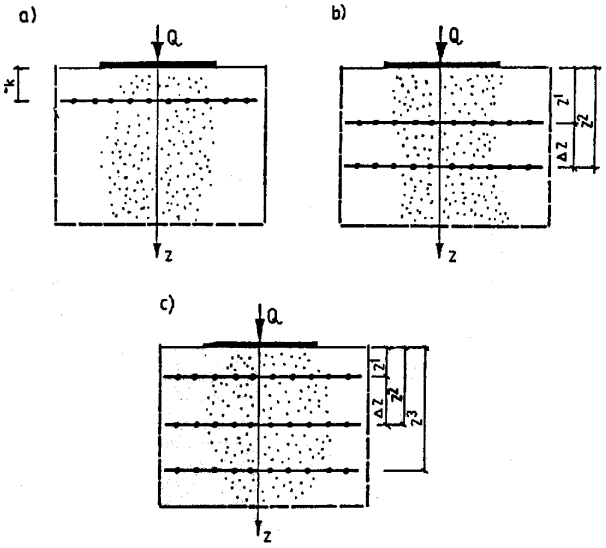

Fig. 2. Diagrams of investigation models: a – model with a single reinforcement insert (net); b – double-insert model; c – triple-insert model; z – insert levels

The reinforcement nets were located on the container's seven measuring levels, spaced by the value of (z = 0.06 m; z_1 = 0.03 m; z_2 = 0.09 m; z_3 = 0.15 m; z_4 = 0.21 m; z_5 = 0.27 m; z_6 = 0.33 m; z_7 = 0.39 m. Coarse-grain dry sand was mainly used for the inves-

tigation, although for comparison purposes river gravel 5/10 and basalt grit 8/16 were also used. Two states of the soil medium were taken into account: (I) loosely spilled, and (II) preliminary compacted using the unit pressure $q = 0.24$ MPa (the medium was subjected to 8 cycles of load applying/removing). The load q was conveyed to the soil sample by means of a square steel plate with its side equal to 0.32 m. The value of the load inducted ensures the stress uniformity at the model's height and therefore the vertical stress was assumed as $p_z = q_{max}$. Fig. 2 shows the diagrams of experimental models.

3. Investigation results for sand reinforced with a single insert

Figure 3 shows the plots of unit side pressure at the medium layer's depth for consecutive stages of applying load. The total zone of side pressure for the no-load medium is almost identical, both for the loosely dumped and reinforced one (see Fig. 3 a, curve 1). However, there appears – relatively small as yet – a difference in the shape of the side pressure curves. As the load increases, the pressure curve for the reinforced medium deviates in its shape from the reference curves. A characteristic influence zone of the reinforcement begins to develop on the reinforced medium's side pressure curves, especially apparent for the load $q > 0.10$ MPa (curves 2, 3, 4 in Fig. 3 a). This is defined as the reinforcement insert's influence zone on the soil.

The greatest reduction in the side pressure ordinate occurs in the reinforcement plane. The influence of reinforcement is transferred to the surrounding medium with a certain distance from it. The range of the reinforcement influence zone for a given soil type depends, among other things, on the following factors:

- the intensity of external load (the reinforcement constitutes a passive element) and the history of the load (e.g. a process of cyclic applying and removing load),
- technical properties of the reinforcement inserts (e.g. mesh size).

Horizontal forces of the soil side pressure are reduced by the reinforcement due to the friction of the medium's grains against the surface of the net rods, as well as due to the resistance to the movement revealed by the rods located crosswise with respect to the horizontal forces. The restriction of horizontal movement of soil grains directly at the surface of reinforcement inserts is propagated by means of inter-grain friction within a certain distance. This is defined as the effect of reinforcement-soil interaction. It can otherwise be termed as local "homogeneity" of a – normally discrete – granular medium which can be regarded as analogous to the so-called "anisotropic cohesiveness of reinforced sand", indicated in French investigations [4]. "Anisotropic" cohesiveness of the composite, which includes loose soil, occurs in the medium's grains found within the zone of the reinforcement "influence".

The cohesiveness is described by the formula:

$$c = 0.5\, R_T\, tg\,(0.25\pi + 0.5\varphi)\,(\Delta z)^{-1} \qquad (1)$$

where: R_T – resistance of reinforcement layers to tension [kN.m^{-1}],
Δz – spacing of horizontal reinforcement layers [m],
φ – internal friction angle of soil medium.

It is generally known that multiple load cycles applied to loose soil result in its being partially compacted. In the investigation, after eight cycles of applying and removing load, the increase in side pressure for the various stages of applying load in the eighth cycle was significantly lower. At the same time, the reinforcement influence effectiveness is smaller than a loosely spilled medium. This is evidenced by partial disappearance of the "interaction" zones (Fig. 3 b), very distinct in a loosely spilled medium (Fig. 3 a). Table 1 shows the reinforcement effectiveness index as a function of medium concentration for the case of a medium reinforced by a single insert S 12 at the level of $z_4 = 0.21$ m. As a measure of the effectiveness e [%], the ratio has been assumed of an average side pressure in a reinforced medium p_y* [MPa] and that in a not-reinforced medium (i.e. reference) taken as $p_y = 100$ %:

$$e = p_y^*/p_y\ 100\ [\%] \qquad (2)$$

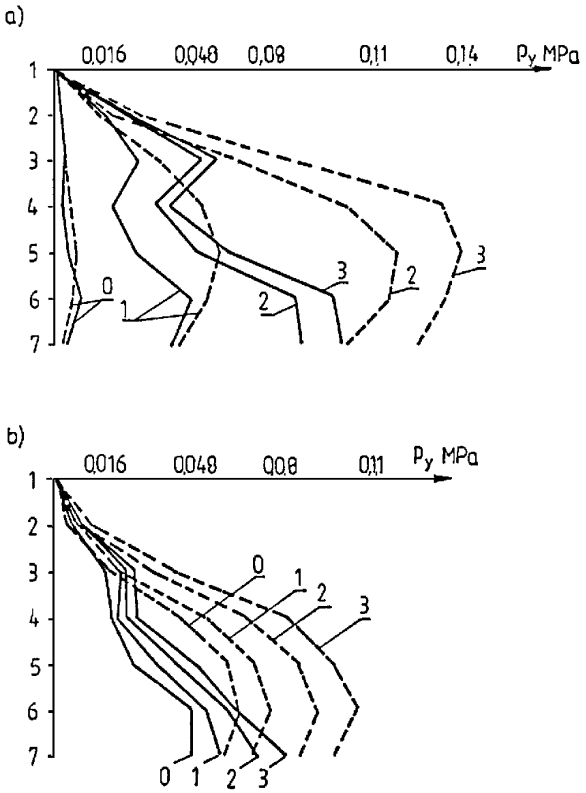

Fig. 3. Plots of unit side pressure at the level of sand layer at various loading stages: a – loosely spilled sand; b – preliminary compacted sand; - - - non-reinforced soil (reference); -- - reinforced soil with a single steel net with 12 × 12 mm mesh (designation S 12) at level z_4; 0 – without load; 1 – $q = 0.09$ MPa; 2 – 0.19 MPa; 3 – 0.24 MPa

Fig. 4 depicts plots of the unit side pressure for a loosely spilled medium reinforced with a single insert at the level $z_4 = 0.21$ m for

various types of reinforcement nets (related to the reference 1, i.e. no-reinforcement medium). The plots provide a comparison of effects obtainable by employing the reinforcement with a "rigid" 12-by-12-millimeter-mesh steel net (S 12), which is the common type of reinforcement, versus flexible nets and steel nets with various mesh sizes.

Table 1

Load q [MPa]		0.0	0.10	0.20	0.25
e [%]	loosely spilled sand	38.2	36.5	33.3	29.8
	preliminary compacted sand	47.2	43.3	40.8	39.3

Fig. 5 shows the side pressure distribution for a loosely spilled medium at the layer level. The figure illustrates the effect of reinforcement layout on the pressure value and pressure curve shape. The plots were taken for the pressure of $q = 0.24$ MPa. An analysis of the plots reveals that the reinforcement-generated reduction of the horizontal soil pressure drops clearly below and above the optimum reinforcement position. For the case of extreme positions of the insert (Fig. 6a, c), the reinforcement influence zone is significant. In contrast, the central location of the reinforcement (Fig. 6b) results in the maximum range of the influence zone $v = v_{max}$ and in the consequent reduction of side pressure. Table 2 presents values of the total side pressure P_y* expressed as percentages of the reference (P_y for the reference was assumed to be 100 %).

To sum up, the influence zone range v depends, among other things, on the type and state of soil and factors related to the reinforcement (e.g. geometric and material parameters of inserts, their arrangement). The granular medium-reinforcement interaction is satisfactory, if the insert does not produce soil delamination, is sufficiently rigid and develops sufficient resistance to being pulled out and has been located in the zone of maximum side pressure ordinates (of a non-reinforced medium). The optimum reinforcement effectiveness with respect to soil pressure reduction is to be expected in those places where maximum values of pressure ordinates p_y occur. Therefore, the most favorable case of reinforcement

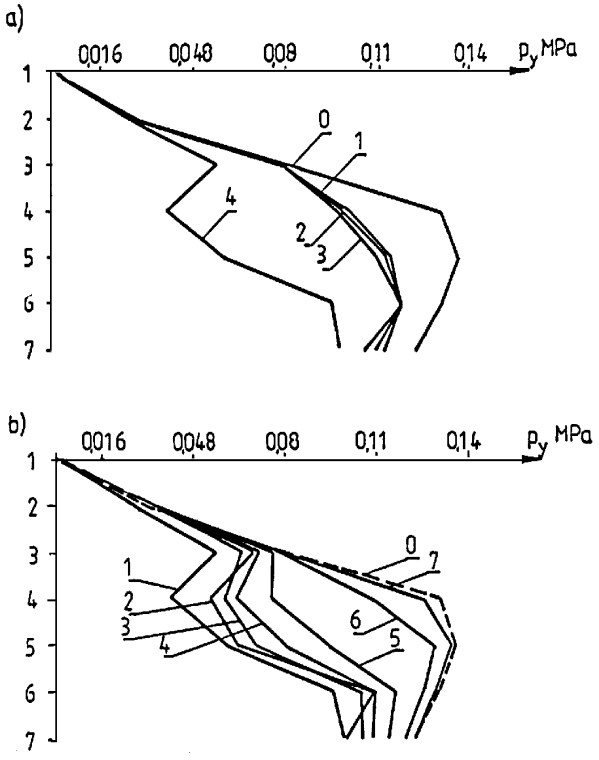

Fig. 4. Plots of side pressure for loosely spilled single -net-reinforced sand at level z_4. Load $q = 0.24$ MPa.
a) Designations: 0 - non-reinforced sand (reference); 1 - reinforcement of 45-by-45 millimeter plasti net; 2 - 14-by-14-millimeter plastic net; 3 - 6-by-6 millimeter plastic net; 4 - steel net S 12. b) Designations: 0 - reference; 1 - steel net S 12; 2 - 16-by-16-millimeter steel net; 3 - 27.5-by-27.5-millimeter steel net; 4 - 35.5-by-35.5-millimeter steel net; 5 - 74.5-by-74.5-millimeter steel net; 6 - 152.5-by-152.5-millimeter net; 7 - 220-by-220-millimeter steel net

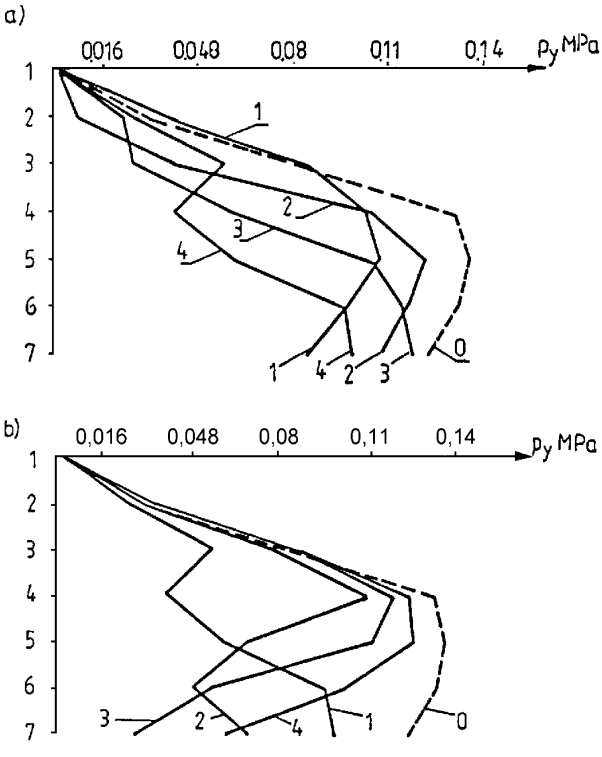

Fig. 5. Distribution of side pressure for loosely spilled sand at variable depth with respect to the location of single reinforcement by steel net S 12. Load $q = 0.24$ MPa. a) Designations: 0 - non-reinforcement sand (reference); 1 - reinforcement at level z_1; 2 - reinforcement at level z_2; 3 - reinforcement at level z_3; 4 - reinforcement at level z_4. b) Designations: 0 - reference; 1 - reinforcement at level z_4; 2 - reinforcement at level z_5; 3 - reinforcement at level z_6; 4 - reinforcement at level z_7

localization is such where the reinforcement-soil "interaction" area covers as much as possible of the area bounded by the curve in the side pressure diagram for a non-reinforced medium.

Table 2

Positions of the nets z_k [m]		z_1 0.03	z_2 0.09	z_3 0.15	z_4 0.21	z_5 0.27	z_6 0.33	z_7 0.39	Non-reinforced
p_y^*/p_y [%]	loosely spilled sand	80.5	75.0	67.3	54.1	62.7	70.9	85.5	100
	preliminary compacted sand	82.3	78.0	70.1	57.0	65.3	73.0	75.4	100

4. Investigation results for sand reinforced with multiple inserts

Fig. 7 depicts diagrams of the side pressure taken at various measurement levels of a model, which employed the reinforcement of two S 12 nets. Fig. 8 shows the horizontal pressure of sand reinforced with three S 12 nets. Characteristic "interaction" zones of the reinforcement become noticeable in these cases, similarly to the single-net-reinforced sand. Even insignificant vertical dislocations of the inserts reflect visibly on the redistribution of side pressure ordinates. If both inserts are situated too close one to the other (in the double-reinforcement-layer arrangement), an effect arises analogous to the side pressure distribution for a medium reinforced with a single net; e.g. the total side pressure of double-reinforced sand at the heights z_5 and z_6 equals P_y = 50.1 % of the reference pressure (i.e. that for the no-reinforcement medium), while the pressure of single-reinforcement sand at the height z_5 equals P_y = 62.3 % for a similar distribution of pressure ordinates py (curves 1 and 2 in Fig. 9). For extremely unfavorable arrangements of two reinforcement planes, results can be even worse than for a single reinforcement, e.g. for double-reinforced sand with reinforcements at the levels z_6 and z_7, the value of P_y = 71.8 % of the reference pressure has been obtained, while for a single reinforcement at the level z_6, the total pressure P_y attains 70.9 % of the reference pressure (curves 3 and 4 in Fig. 9). The distribution of side pressure ordinates is similar and „interaction" zones are not visible. An optimum relative position of both reinforcement nets can be determined (vertical spacing $\Delta z = \Delta z_{limit.}$), in which the maximum reduction in side pressure is attained and thus the effectiveness of reinforcement action is the greatest possible. For that case, the curve of unit side pressure between the levels of consecutive inserts does not reveal any convexity or concavity (case I in Fig. 10) and the inserts' interaction zones presumably overlap.

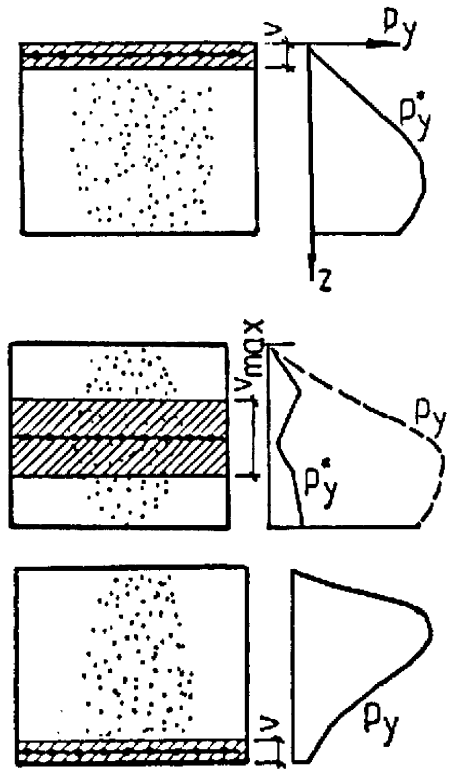

Fig. 6. Zone of local composite homogeneity (as determined by width v) due to reinforcement-soil interaction: a, b – extreme arrangements of insert; c – optimum position of reinforcement; — side pressure of reinforced medium; - - - pressure of non-reinforced medium

An increase in the vertical separation $\Delta z_{limit.}$ of inserts reflects unfavourably on the reduction in the soil side pressure; this is the case II in Fig. 10. The curve representing the soil pressure between the insert levels is convex which implies that the reinforcements do not interact in the medium through their respective influence zones.

A reduction in the vertical separation below $\Delta z_{limit.}$ results in overlapping of the influence zones; this produces an effect similar to the side pressure distribution for single-insert-reinforced soil or,

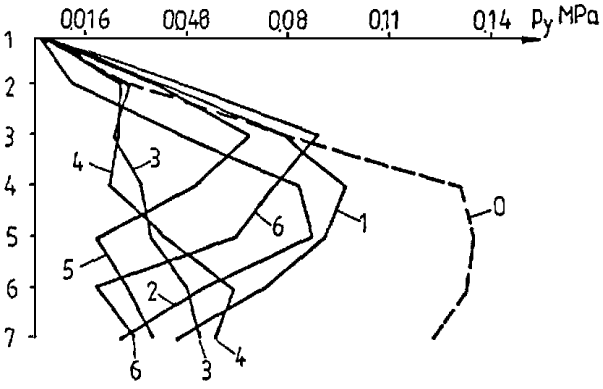

Fig. 7. Plots of side pressure at individual measuring levels of the model with loosely spilled sand reinforced with two S 12 nets, for various positions of the nets. Load q = 0.24 MPa. Designations: 0 – reference; 1 – reinforcement at levels z_1 and z_7; 2 – reinforcement at levels z_2 and z_6; 3 – reinforcement at levels z_3 and z_5; 4 – reinforcement at levels z_3 and z_4; 5 – reinforcement at levels z_4 and z_5; 6 – reinforcement at levels z_5 and z_6

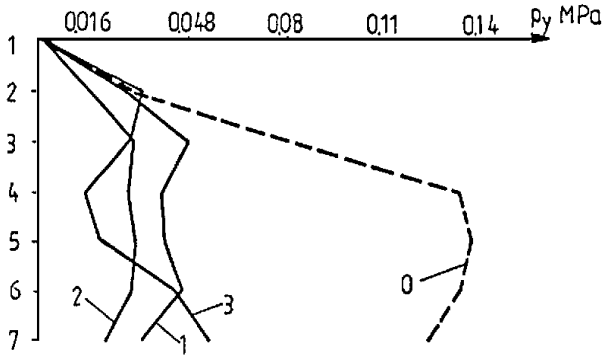

Fig. 8. Horizontal pressure of loosely spilled sand reinforced with three S 12 nets, for various positions of the nets. Designations: 0 - reference; 1 - reinforcement at levels z_1, z_4, z_7; 2 ÷ reinforcement at levels z_2, z_4, z_6; 3 - reinforcement at levels z_3, z_4, z_5

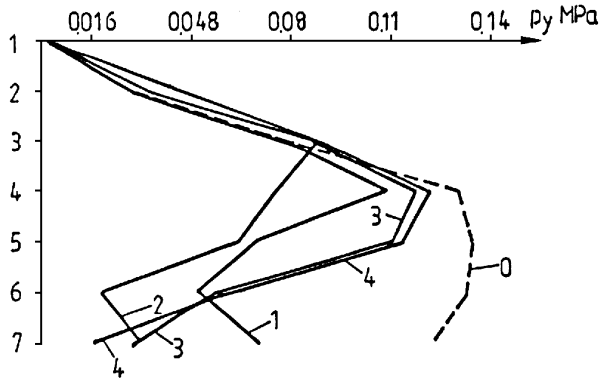

Fig. 9. Plots of side pressure for loosely spilled sand reinforced with S 12 nets. Load q = 0.24 MPa. Designations: 0 - non-reinforced sand; 1 - reinforcement with single net at level z_5; 2 - reinforcement with two nets at levels z_5 and z_6; 3 - reinforcement with single net at level z_6; 4 - reinforcement with two nets at levels z_6 and z_7

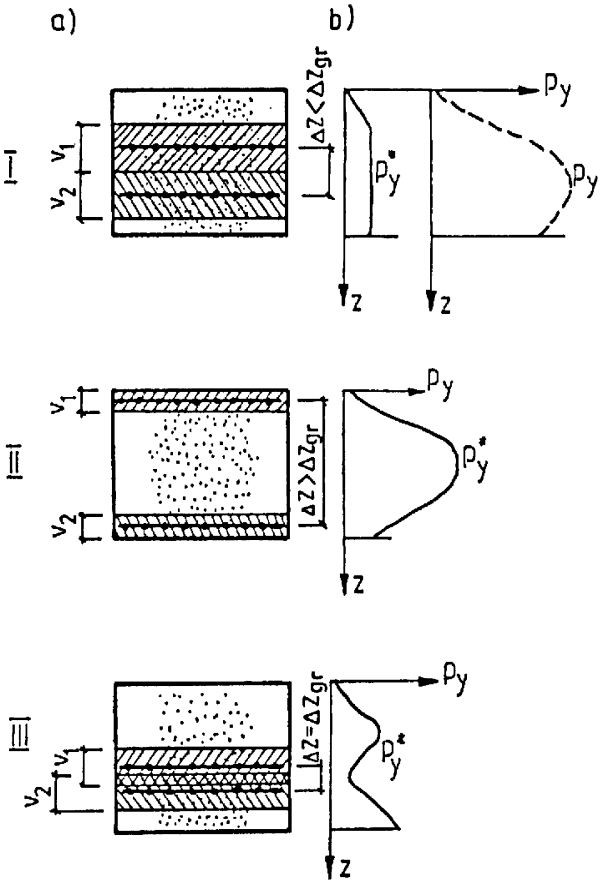

Fig. 10. Zones of local homogeneity for double-reinforced medium: a - cases I, II, III of localization of soil medium-insert interaction zones for two layers of reinforcement; b - plots of soil medium side pressure for cases I, II, III; v_1, v_2 - vertical range of soil-reinforcement interaction zone; - - - plot of side pressure for non-reinforced medium; — side pressure for reinforced medium

otherwise termed, the reinforcement action effectiveness decreases (case III in Fig. 10). For that case, the part of the soil side pressure curve contained between the levels of the inserts assumes a concave form and, as the model investigation shows, the reinforcement effectiveness drops. Tables 3 and 4 present values of the total side pressure of sand reinforced with two and three S 12 nets, respectively.

5. Strength characteristics of reinforced medium

Loose reinforced soil can be regarded as [6], [8]:

a) a medium without cohesiveness, in which the internal friction angle is increased due to the application of reinforcement ($c = 0$, $\Delta\varphi > 0$);
b) a soil, which if in extreme state, behaves as a cohesive anisotropic soil with the internal friction angle identical to that of non-reinforced soil but revealing properties indicative of the cohesiveness directly proportional to the tensile strength ($c > 0$, $\Delta\varphi = 0$).

In the investigation, the active pressure p_y was measured which proved to be dependent on a number of factors. If, for the maximum load q_{max}, the values of p_z and the pressure coefficient K are regarded as their respective extreme values, then after inserting them into the classical extreme state equation, the effect of the angle φ increase in reinforced soil can quantitatively be evaluated. Such an approach has generally been acknowledged as admissible for the purpose of qualitative comparison involving mechanical characteristics of reinforced and not reinforced soil exposed to identical investigation conditions.

When considering the case of non-cohesive soil (a), the extreme state condition for non-reinforced soil samples can be expressed in its general form as:

$$p_y / p_z = tg^2 (45^0 - 0.5\varphi) = K_{min} \qquad (3\text{ a})$$

and, by an analogy, for reinforced soil:

$$p_y^*/p_z = tg^2\,(45° - 0.5\varphi^*) = K_{min}^* \qquad (3\ b)$$

Table 3

Positions of the nets z_k^1, z_k^2, z_k^3 [m]		z_1 z_7	z_2 z_6	z_3 z_5	z_4 z_4	z_5 z_5	z_6 z_6	z_7 z_7	Non-reinforced
p_y^*/p_y [%]	loosely spilled sand	68.2	48.2	33.6	35.0	35.3	50.1	71.8	100
	preliminary compacted sand	70.3	50.6	39.0	38.9	39.2	53.6	74.0	100

Table 4

Positions of the nets z_k^1, z_k^2, z_k^3 [m]		z_1 z_4, z_7	z_2 z_4, z_6	z_3 z_4, z_5	Non-reinforced
p_y^*/p_y [%]	loosely spilled sand	36.4	23.6	28.2	100
	preliminary compacted sand	41.7	34.0	34.2	100

Also the relationships $\varphi^* > \varphi$ and $\Delta\varphi = \varphi^* - \varphi$ hold, where φ represents the internal friction angle of the soil under investigation, and $\Delta\varphi$ is the increase in friction angle.

By substituting appropriate data, the following friction angles are obtained: φ for non-reinforced soil and φ^* for reinforced soil. The shearing strengths τ_f and τ_f^* of non-reinforced and reinforced soils, respectively, have been calculated from the condition:

$$\tau_f = p_z\ tg\varphi \text{ and } \tau_f^* = p_z\ tg\varphi^* \qquad (4)$$

In the formula (4), the value $p_z = q_{max} = 0.24$ MPa has been substituted according to the aforementioned assumption. Calculation results for the parameters φ, $\Delta\varphi$, and τ_f for loosely spilled sand are presented in table 5.

For the second case, that of reinforced soil, the destruction curve in the ordinate system of vertical p_z and horizontal p_y stresses is determined, according to [4], by the equation:

$$p_z = p_y\ tg^2\,(45° + 0.5\varphi) + p^0 \qquad (5)$$

where

$$p_0 = 2\ c\ tg^2\,(45° + 0.5\varphi) \qquad (6)$$

is an initial stress (i.e. when $p_y = 0$) signaling that reinforced soil behaves as if possessed anisotropic cohesiveness. The value of the cohesiveness c is maximal because the extreme stress state prevails. Model investigations provided a value of the term $p_0 = p_z^* - p_z = \Delta p_z$ (the effect of carrying capacity increase). The term p_0 (for various reinforcement types) and the friction angle $\varphi = 26.220$, as determined for non-reinforced medium (table 5), were inserted into eq. (6), from which the cohesiveness effect c for individual types of reinforcement has been calculated. Next, the shearing resistance of reinforced soil has been obtained from the following formula, provided that we assume that the destruction mechanism for a soil sample consists in the slip of granular medium with respect to inserts:

$$\tau_f = p_z\ tg\varphi + c = p_z\ tg\varphi + p_0\ [2\ c\ tg(45° + 0.5\varphi)]^{-1} \qquad (7)$$

Table 5

Model	Positions of the nets	Parameters		
		φ [°]	$\Delta\varphi$ [°]	[MPa]
Non-reinforced	–	26.22	–	0.118
With single net	z_1	32.02	5.80	0.149
	z_2	32.49	6.27	0.152
	z_3	35.26	9.04	0.169
	z_4	39.05	12.83	0.194
	z_5	37.52	11.29	0.183
	z_6	35.79	9.57	0.172
	z_7	30.85	4.63	0.143
With two nets	z_1, z_7	36.69	10.47	0.178
	z_2, z_6	43.68	17.46	0.228
	z_3, z_5	49.79	23.57	0.283
With three nets	z_1, z_4, z_7	48.84	22.62	0.273
	z_2, z_4, z_6	55.91	29.68	0.353
	z_3, z_4, z_5	52.38	26.16	0.310

In the formula, the first term relates to non-reinforced soil and the second one is an addition that results from reinforcement.

Calculated values of cohesiveness c and shearing resistance for loosely spilled sand are presented in table 6.

Table 6

Model	Positions of the nets	Parameters	
		c [MPa]	τ_f [MPa]
Non-reinforced	–	–	0.117
With single net	z_1	0.019	0.137
	z_2	0.021	0.139
	z_3	0.033	0.151
	z_4	0.052	0.170
	z_5	0.044	0.162
	z_6	0.035	0.153
	z_7	0.015	0.133
With two nets	z_1, z_7	0.040	0.157
	z_2, z_6	0.083	0.201
	z_3, z_5	0.140	0.258
With three nets	z_1, z_4, z_7	0.130	0.248
	z_2, z_4, z_6	0.232	0.350
	z_3, z_4, z_5	0.174	0.292

6. Side pressure of various soils-results of comparative investigation

The comparative investigation has been carried out on coarse-grain sand (internal friction angle $\varphi = 29°$), river gravel 5/10 and basalt grit 8/16 ($\varphi = 38°$). It was aimed at an evaluation of the effect the granular medium type has on the formation of the reinforcement influence zone and its size. Following the rule that reinforcement should not lead to the medium delamination, a rigid steel-net reinforcement with square 16-by-16-millimeter mesh (designation S 16) has been employed in the investigation. Fig. 11 a shows the plots of side pressure in the non-reinforced medium. Fig. 11 b depicts the plots of side pressure in sand, gravel and grit, all both single-reinforced as well as double-reinforced.

The lower the internal friction angle of a given soil, the greater the effect of reinforcement on the side pressure reduction. For double-reinforced grit in the model investigated (plot 3 in Fig. 11 b), the optimal separation of S 16 inserts seems to be $\Delta z_{opt} = 0.12$ m (the curve between the levels z_3 and z_5 does not exhibit any convexity), while the respective plots for sand (1) and gravel (2) have a convex form in the zone discussed which suggests the value $\Delta z_{opt} < 0.12$ m (the reinforcement should be more dense). To sum up, the optimal reinforcement separation depends on the medium's internal friction angle.

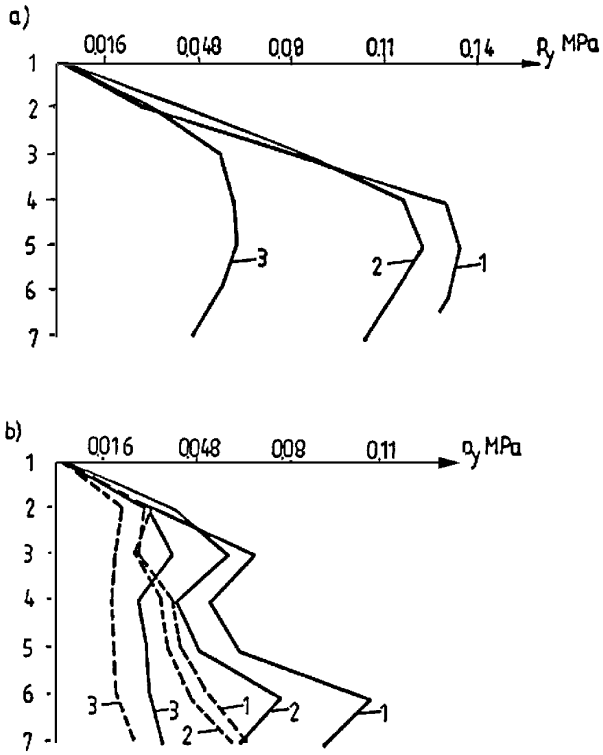

Fig. 11. plots of side pressure for three types of loosely spilled granular medium in the presence of load q = 0.24 MPa: a - non-reinforced medium; 1 - coarse grain sand; 2 - river gravel; 3 - basalt grit; b - reinforced medium: — with a single 16-by-16-millimeter steel net at level z_4; - - - with two 16-by-16-millimeter steel nets at levels z_3 and z_5; 1 - sand; 2 - gravel; 3 - grit

7. Summary

Based on model investigation, an attempt has been made to assess the effect of reinforcement type (i.e. material, net mesh size), arrangement of inserts as well as the type and concentration of granular medium on the vertical range of the reinforcement-soil medium interaction zone.

The effectiveness of the net-like reinforcement with soil medium depends on the spacing of rods, rigidity of the net's material spatial arrangement (i.e. resistance to pulling out), the depth at which the interactions occur and physical properties of the medium.

For two-or multiple-insert reinforcements, such a relative position of the inserts, expressed in terms of vertical separation Δz, can be found which ensures the maximum side pressure reduction and thus the maximum possible effectiveness of the reinforcement action. In this particular case, the curve of unite side pressure between consecutive insert levels exhibits neither convexity nor concavity and, presumably, the influence zones of inserting overlap.

The effect of reinforcement on the level of side pressure reduction is more pronounced if the internal friction angle for a given soil is lower. The optimum separation of inserts in a multilayer reinforcement is smaller in media with a lower internal friction angle. Values of strength parameters for the medium being modeled are closely related to the effectiveness of interaction between reinforced soil components, and thus with the effectiveness of reinforcing action, the latter being determined by the range of the "interaction zone".

References

[1] JAROMINIAK A.; *Light retaining structures*, WKiŁ, Warszawa, 1999 (in Polish)
[2] JAROMINIAK A., GAWOR B.; *Supporting structures made of soil reinforced with polyester resin/fiber glass.* Prace IBDiM nr 2, WKiŁ, Warszawa, 1989, pp. 87-159 (in Polish)
[3] LEŚNIEWSKA D., KULCZYKOWSKI M.; *Design fundamentals for composite-reinforced soil structures.* Procedure IBW PAN, Gdańsk, 1995 (in Polish)
[4] LONG N.T., SCHLOSSER F.; *Principle of operation and behaviour of reinforced soil.* Selected problems of geotechnology, Ossolineum, PAN-IBW, Wrocław, 1978, pp. 157-184 (in Polish)

[5] LONG N.T.; *Investigation of reinforced soil.* Selected problems of geotechnology, Ossolineum, PAN-IBW, Wrocław, 1978, pp. 185-210 (in Polish)
[6] LONG N.T., SCHLOSSER F.; *Dimensioning of reinforced-soil walls.* Selected problems of geotechnology, Ossolineum, PAN-IBW, 1978, pp. 211-237 (in Polish)
[7] SAWICKI A.; *Statics of reinforced-soil structures,* IBW PAN, Gdańsk, 1995 (in Polish)
[8] SCHLOSSER F.; *Reinforced soil in civil engineering,* Archiv. Hydrotechn., 1974, Vol. XXI, No. 2, pp. 299-336 (in Polish)
[9] SUROWIECKI A.; *Experimental analysis of loose reinforced-soil carrying capacity,* Doctor's Thesis, Raport S.: PRE nr 64, Wrocław, 1984 (in Polish)
[10] SUROWIECKI A.; *Laborversuche zum Einfluss ausgew(hlter Parameter auf die Wirkung der Bewehrung in lockeren Boden,* Bauingenieur, 1989, J. 64, Nr 5, pp. 215-217 (in German)
[11] SUROWIECKI A.; *Laboruntersuchungen von mechanischen Eigenschaften bewehrter Bodenschichten,* Bautechnik, 1994, J. 71, H. 11, pp. 707-711 (in German)
[12] WIŁUN Z.; *Fundamentals of geotechnology,* WKiŁ, Warszawa, 1989 (in Polish)

Robert Tenzer *

STRUČNÝ PREHĽAD TEÓRIE VÝŠOK

A BRIEF OVERVIEW TO THEORY OF HEIGHTS

V minulosti bolo v rôznych častiach sveta formulovaných a prakticky použitých mnoho typov výškových systémov. V súčasnosti sú prevažne používané ortometrické a normálne výšky. Ortometrické výšky sú prirodzené výšky nad hladinou mora, teda nad geoidom. Definícia ortometrických výšok vyžaduje aspoň teoretickú znalosť rozloženia hustoty topografických más medzi zemským povrchom a geoidom. Z tohto dôvodu Molodensky v roku 1945 sformuloval teóriu normálnych výšok založenú na princípe, že výšky môžu byť počítané bez hypotézy o rozložení hustoty topografickej hmoty. Tento článok sa zaoberá teoretickými aspektmi definície výšok.

In various parts of the world many kinds of height systems have been formulated and practically used in the past. Nowadays, orthometric heights and normal heights are widely used. The orthometric heights are the natural heights above sea level, that is, above the geoid. The definition of the orthometric heights required the knowledge of the topographical masses density distribution between the Earth's surface and the geoid, at least theoretically. For this reason Molodensky in 1945 formed a theory of normal heights based on the principle that the heights can be evaluated without any hypothesis about the density distribution of topographical masses. Theoretical aspects of the definition of heights are described in this paper.

1. Úvod

V klasickom zmysle, podľa Gaussa a Listinga, je geoid definovaný ako ekvipotenciálna (hladinová) plocha, ktorej geopotenciálna hodnota je W_o.

C. F. Gauss (1828) stanovil ako hraničnú plochu Zeme hladinovú plochu [4]. Neskôr F. W. Bessel (1837) definoval hraničný povrch Zeme ako ekvipotenciálnu plochu aproximujúcu strednú pokojnú hladinu oceánov [2]. Nakoniec J. B. Listing (1873) nazval tento povrch geoidom [7]. Geoid je tak základnou ekvipotenciálnou plochou použitou na definíciu prirodzených ortometrických výšok.

Na definovanie skutočnej hodnoty ortometrickej výšky je ale potrebné poznať rozloženie hustoty topografických más medzi geoidom a zemským povrchom.

F. R. Helmert (1890) definoval ortometrické výšky na základe hypotézy o rozložení hustoty [6] pričom predpokladal konštantnú topografickú hustotu $\rho_o = 2{,}67\ \mathrm{g.cm}^{-3}$.

M. S. Molodensky (1945) sformuloval teóriu normálnych výšok bez hypotézy o rozložení hustoty hmoty topografických más [9].

2. Geopotenciálna kóta

H. Bruns (1878) opísal geometriu tiažového poľa Zeme vzťahom [1]

$$dW(H, \Omega) = -g(H, \Omega)\, dH(\Omega) = const., \qquad (2.1)$$

kde zemepisné súradnice φ, λ sú reprezentované uhlom $\Omega = (\varphi, \lambda)$, H je výška určená niveláciou.

1. Introduction

In a classical sense of Gauss and Listing, the geoid is defined as an equipotential (level) surface whose geopotential value is W_o.

First, C. F. Gauss (1828) stipulated that the Earth's boundary surface should be a level surface [4]. Later, F. W. Bessel (1837) defined the Earth's boundary surface as the equipotential surface approximating the mean calm ocean levels [2]. Finally, J. B. Listing (1873) named this surface "geoid" [7]. The geoid is then basic equipotential surface for the definition of the natural orthometric heights.

To define an actual value of the orthometric height, the distribution of the density of the topographical masses between the geoid and the Earth's surface has to be known.

F. R. Helmert (1890) defined the orthometric height based on a hypo- thesis of density distribution [6]. The constant topographical density $\rho_o = 2.67\ \mathrm{g.cm}^{-3}$ is assumed in this hypothesis.

M. S. Molodensky (1945) formed theory of the normal heights without using any hypothesis about density distribution of topographical masses [9].

2. Geopotential number

H. Bruns (1878) described the geometry of the Earth's gravity field by the equation [1]

$$dW(H, \Omega) = -g(H, \Omega)\, dH(\Omega) = const., \qquad (2.1)$$

where geographic coordinates φ, λ are represented by solid angle $\Omega = (\varphi, \lambda)$, and H is a height obtained from the levelling.

* **Robert Tenzer**
University of New Brunswick, Department of Geodesy and Geomatics Engineering, Fredericton, N.B., Canada

Brunsov vzťah (2.1) hovorí, že konštantný diferenciálny rozdiel $dW(r, \Omega)$ potenciálov dvoch blízkych hladinových plôch je rovný zápornej hodnote súčinu tiažového zrýchlenia $g(H, \Omega)$ a vzdialenosti $dH(\Omega)$ pozdĺž ťažnice medzi oboma hladinovými plochami.

Geopotenciálna kóta $C(H, \Omega)$ je definovaná aplikáciou Brunsovho vzťahu na rozdiel tiažového potenciálu na geoide a tiažového potenciálu $W(H, \Omega)$ na zemskom povrchu (Heiskanen a Moritz, 1967)

$$C(H, \Omega) = W_o - W(H, \Omega) = \int_0^{H(\Omega)} g(h, \Omega)\, dH(\Omega). \quad (2.2)$$

3. Ortometrická výška

Skutočná ortometrická výška $H^O(\Omega)$ je definovaná ako dĺžka ťažnice medzi geoidom a zemským povrchom (obr. 1). Podľa Brunsovho vzťahu je rozdiel dvoch potenciálov konštantný a nezávislý od integračnej cesty.

Vzhľadomna to je integrácia pozdĺž ťažnice medzi geoidom a zemským povrchom rovná integrácii na zemskom povrchu od nulového výškového bodu $O(H = 0, \Omega')$ na geoide (maregraf) do bodu $P(H, \Omega')$,

$$\int_{O(H\,=\,0,\,\Omega')}^{P(H,\,\Omega')} g(H, \Omega')\, dH(\Omega') = \int_0^{H(\Omega)} g(H, \Omega)\, dH(\Omega) = const. \quad (3.1)$$

Podľa teorémy o strednej hodnote integrálu nadobudne integrál na pravej strane rovnice (3.1) tvar

$$\int_0^{H(\Omega)} g(H, \Omega)\, dH(\Omega) = \bar{g}(H, \Omega) \int_0^{H(\Omega)} dH(\Omega). \quad (3.2)$$

kde $\bar{g}(H, \Omega)$ je stredná hodnota tiaže pozdĺž ťažnice medzi geoidom a zemským povrchom.

Integrálny výraz

$$H^O(\Omega) = \int_0^{H(\Omega)} dH(\Omega), \quad (3.3)$$

rovný dĺžke ťažnice medzi geoidom a zemským povrchom, je potom skutočná ortometrická výška $H^O(\Omega)$.

Substitúciou rovníc (3.3) a (2.2) do rovnice (3.2) dostaneme základný vzťah na definíciu skutočnej ortometrickej výšky [5]

$$H^O(\Omega) = \frac{1}{\bar{g}(H, \Omega)} \int_{O(H\,=\,0,\,\Omega')}^{P(H,\,\Omega')} g(H, \Omega')\, dH(\Omega') = \frac{C(H, \Omega')}{\bar{g}(H, \Omega)}. \quad (3.4)$$

Na prevod výsledkov nivelácie $C(H, \Omega') = \int_{O(H\,=\,0,\,\Omega')}^{P(H,\,\Omega')} g(H, \Omega')\, dH(\Omega')$ na ortometrické výšky $H^O(\Omega)$ potrebujeme poznať hodnotu tiaže $\bar{g}(H, \Omega)$ pod zemským povrchom. Keďže hodnoty $\bar{g}(H, \Omega)$ nemôžu byť merané, musia byť počítané z tiažových $g(H, \Omega)$ údajov na zemskom povrchu a redukované podľa hypotézy o rozložení hustoty topografickej hmoty.

Bruns' formula (2.1) states that the constant difference $dW(r, \Omega)$ of potentials of two closed equipotential surfaces is equal to the negative product of the gravity acceleration $g(H, \Omega)$ and the distance $dH(\Omega)$ along the plumb line between these equipotential surfaces.

The geopotential number $C(H, \Omega)$ is defined by applying Bruns' formula to the difference between the gravity potential W_o on the geoid and the gravity potential $W(H, \Omega)$ on the Earth's surface [5]

$$C(H, \Omega) = W_o - W(H, \Omega) = \int_0^{H(\Omega)} g(h, \Omega)\, dH(\Omega). \quad (2.2)$$

3. Orthometric height

The actual orthometric height $H^O(\Omega)$ is defined as a length of the plumb line between the geoid and the Earth's surface (Fig.1). According to Bruns' formula, the difference between two potentials is constant and independent of a path of integration. Consequently, the integration along the plumb line between the geoid and the Earth's surface is equal to the integration over the Earth's surface from the zero-height point $O(H = 0, \Omega')$ on the geoid (gauge station) to the point $P(H, \Omega')$

According to the theorem of a mean integral value, the integral on the right-hand side of the equation (3.1) takes the following form

where $\bar{g}(H, \Omega)$ stands for the mean value of the gravity along the plumb line between the geoid and the Earth's surface.

The integral expression

$$H^O(\Omega) = \int_0^{H(\Omega)} dH(\Omega), \quad (3.3)$$

equal to the length of the plumb line between the geoid and the Earth's surface, is then the actual orthometric height $H^O(\Omega)$. Substituting the equations (3.3) and (2.2) to the equation (3.2), we obtain a basic formula for the definition of the actual orthometric height [5]

To convert the result of levelling $C(H, \Omega') = \int_{O(H\,=\,0,\,\Omega')}^{P(H,\,\Omega')} g(H, \Omega')\, dH(\Omega')$ into the orthometric height $H^O(\Omega)$, we need to know the value $\bar{g}(H, \Omega)$ of the gravity inside the Earth. Since $\bar{g}(H, \Omega)$ can not be measured, it has to be computed from the surface gravity. This is done by reducing the observed value $g(H, \Omega)$ of gravity according to the hypothesis of the topographical density distribution.

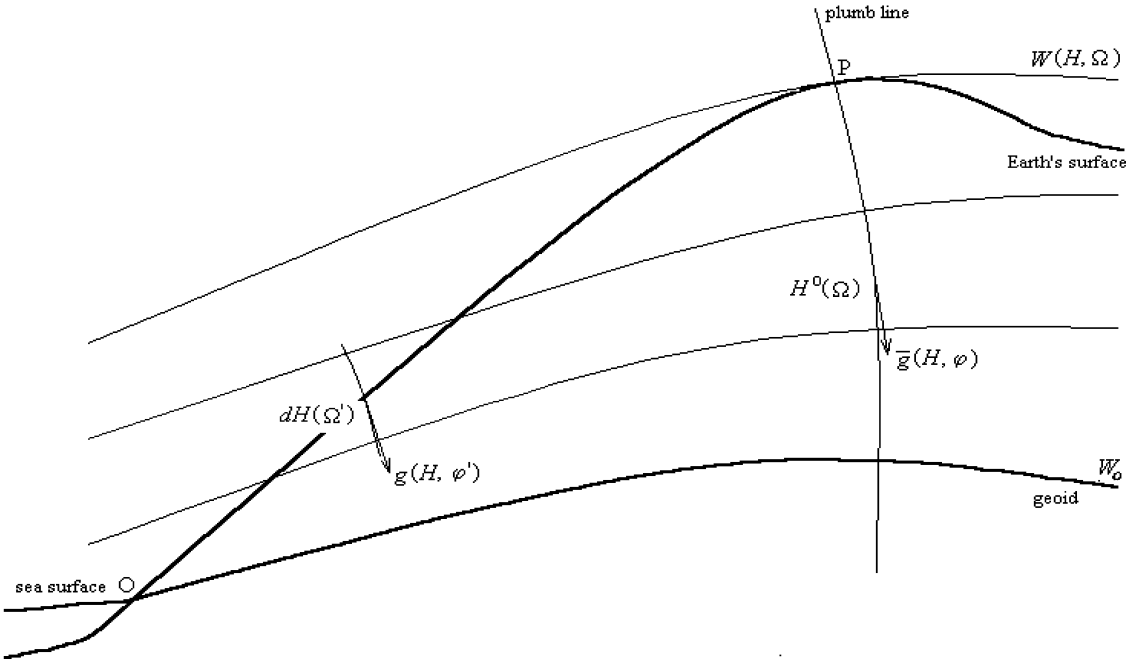

Obr. 1. Ortometrická výška a geopotenciálna kóta
Fig. 1. The orthometric height and the geopotential number

F. R. Helmert (1890) použil na definíciu ortometrických výšok Poincaré-Pray tiažový gradient [6]. Podľa tohto postupu hodnota tiaže potrebná na určenie výšky je získaná z meraného tiažového zrýchlenia na zemskom povrchu redukovaného do stredného bodu medzi geoidom a zemským povrchom.

Tiažová redukcia na stredný bod je počítaná tak, že terén je nahradený nekonečnou Bouguerovou doskou o konštantnej hustote $\rho_o = 2{,}67\ \mathrm{g.cm^{-3}}$.

Helmert (1890) used the Poincaré-Prey's gravity gradient for the definition of the orthometric height [6]. According to this approach, the gravity value needed for the evaluation of the height is obtained from the observed gravity at the Earth's surface reduced to the mid-point between the Earth's surface and the geoid. The reduction of gravity to the mid-point is computed so that the terrain is replaced by an infinite Bouguer plate of constant density $\rho_o = 2.67\ \mathrm{g.cm^{-3}}$.

Helmertova ortometrická výška $H^O(\Omega)$ je definovaná ako [10]

Helmert's orthometric height $H^O(\Omega)$ is defined as [10]

$$H^O(\Omega) = \frac{C(H, \Omega')}{\bar{g}(H/2, \Omega)} = \frac{1}{\bar{g}(H/2, \Omega)} \int_{O(H\,=\,0,\,\Omega')}^{P(H,\,\Omega')} g(H, \Omega')\, dH(\Omega'). \tag{3.5}$$

Stredná hodnota tiaže [5]

Helmert's gravity [5]

$$\bar{g}(H/2, \Omega) = g(H, \Omega') - \frac{1}{2}\frac{\partial\, g(H, \Omega)}{\partial\, H(\Omega)} H^O(\Omega) \cong \frac{1}{2}\left[\frac{\partial\, \gamma\,(H, \varphi)}{\partial\, H(\Omega)} + 4\pi\, G\rho_o\right] H^O(\Omega), \tag{3.6}$$

je definovaná aplikáciou Poincaré-Prey tiažového gradientu vyjadreného v hranatých zátvorkách.

Podľa tejto teórie je vertikálny tiažový gradient uvažovaný ako konštantný pozdĺž ťažnice medzi geoidom a zemským povrchom $\bar{g}(H/2, \Omega)$ takže je počítaný priamo pre stredný bod na ťažnici $H^O(\Omega)/2$.

is defined by using Poincaré-Prey's gravity gradient, which is given by the expression in the square brackets.

According to this theory the vertical gradient of gravity is considered to be constant along the plumb line between the geoid and the Earth's surface. Since the gravity gradient is considered to be constant, $\bar{g}(H/2, \Omega)$ is evaluated directly for the mid-point of the plumb line $H^O(\Omega)$.

Z Poissonovej rovnice [5]

From Poisson's equation [5]

$$\Delta W(x, y, z) = \frac{\partial^2 W(x, y, z)}{\partial\, x^2} + \frac{\partial^2 W(x, y, z)}{\partial\, y^2} + \frac{\partial^2 W(x, y, z)}{\partial\, z^2} = 4\pi\, G\rho_o + 2\omega^2, \tag{3.7}$$

a z výrazu pre stredné zakrivenie hladinovej plochy $J(H, \Omega)$,

and from the expression for the mean curvature $J(H, \Omega)$ of the equipotential surface

$$J(H, \Omega) = \frac{1}{2g(H, \Omega)} \left[\frac{\partial^2 W(x, y, z)}{\partial y^2} + \frac{\partial^2 W(x, y, z)}{\partial z^2} \right], \tag{3.8}$$

môžeme získať Brunsov vzťah pre tiažový gradient

we can obtain Bruns' formula for the gravity gradient

$$\frac{\partial g(H, \Omega)}{\partial H(\Omega)} = -2g(H, \Omega) J(H, \Omega) + 4\pi G\rho_o - 2\omega^2 . \tag{3.9}$$

kde ω je stredná hodnota uhlovej rýchlosti rotácie Zeme, G je Newtonova gravitačná konštanta, ρ_o je stredná hodnota hustoty topografických más medzi geoidom a zemským povrchom, a $\partial^2 W(x, y, z)/\partial x^2$, $\partial^2 W(x, y, z)/\partial y^2$, $\partial^2 W(x, y, z)/\partial z^2$ sú druhé parciálne derivácie tiažového potenciálu v lokálnom astronomickom súradnicovom systéme $x, y, z,$ kde os z je totožná s vonkajšou normálou lokálnej hladinovej plochy.

Vertikálny gradient $\partial \gamma (H, \varphi)/\partial H(\Omega)$ normálneho tiažového zrýchlenia generovaného stredným zemským elipsoidom je

Here ω is the mean value of the angular velocity of the Earth's rotation, G is Newton's gravitational constant, ρ_o is the mean density of the topographical masses between the geoid and the Earth's surface and $\partial^2 W(x, y, z)/\partial x^2$, $\partial^2 W(x, y, z)/\partial y^2$, $\partial^2 W(x, y, z)/\partial z^2$ are second partial derivatives of the gravity potential in the local astronomical co-ordinate system $x, y, z,$ where the z-axis coincides with the outer normal of the local equipotential surface.

The vertical gradient $\partial \gamma (H, \varphi)/\partial H(\Omega)$ of normal gravity generated by the mean ellipsoid of the Earth is

$$\forall H(\Omega) > 0: \quad \frac{\partial \gamma (H, \varphi)}{\partial H(\Omega)} - 2\gamma(H, \varphi) J_o(\varphi) - 2\omega^2 , \tag{3.10}$$

kde $J_o(\varphi)$ je stredné zakrivenie elipsoidu dané vzťahom

with the mean curvature $J_o(\varphi)$ of the ellipsoid given by

$$J_o(\varphi) = \frac{1}{2}\left(\frac{1}{M(\varphi)} + \frac{1}{N(\varphi)} \right). \tag{3.11}$$

V tomto vzťahu sú $M(\varphi)$, $N(\varphi)$ meridiánové polomery krivosti stredného zemského elipsoidu [3]

Here $M(\varphi)$, $N(\varphi)$ are the principal radii of curvature of the mean ellipsoid of the Earth [3]

$$\forall \varphi \in \langle -\pi, \pi \rangle: \quad M(\varphi) = \frac{a(1 - e^2)}{\sqrt{(1 - e^2 \sin^2 \varphi)^3}}, \quad N(\varphi) = \frac{a}{\sqrt{1 - e^2 \sin^2 \varphi}} , \tag{3.12}$$

je φ geodetická šírka, a, b sú poloosi referenčného elipsoidu a $e^2 = (a^2 - b^2)/a^2$ je druhá mocnina prvej numerickej excentricity elipsoidu.

where φ is the geodetic latitude, a, b are the semiaxes of the ellipsoid, and $e^2 = (a^2 - b^2)/a^2$ is the square of the first numerical eccentricity of the ellipsoid.

Poincaré-Preyova teória vertikálneho gradientu predpokladá s do-statočnou presnosťou [10]

The Poincaré-Prey's theory of the vertical gradient of the gravity assumes, with sufficient accuracy, the following [10]

$$g(h, \Omega) J(H, \varphi) \cong \gamma(H, \varphi) J_o(\varphi). \tag{3.13}$$

Poincaré-Preyov vertikálny tiažový gradient môže byť potom prepísaný do nasledovného tvaru

The Poincaré-Prey's vertical gradient of gravity is then

$$\frac{\partial g(H, \varphi)}{\partial H(\Omega)} \cong \frac{\partial \gamma (H, \varphi)}{\partial H(\Omega)} + 4\pi G\rho_o = -2\gamma(H, \varphi) J_o(\varphi) - 2\omega^2 + 4\pi G\rho_o , \tag{3.14}$$

a Helmertova ortometrická výška nadobudne tvar

and the Helmert orthometric height takes the following form

$$H^o(\Omega) = \frac{C(H, \Omega')}{g(H, \Omega) + \gamma(H, \varphi) J_o(\varphi) H^o(\Omega) + \omega^2 H^o(\Omega) - 2\pi G\rho \mathrm{H}^o(\Omega)} . \tag{3.15}$$

4. Normálna ortometrická výška

Číselná hodnota geopotenciálnej kóty $C(H, \Omega')$ je výsledkom nivelácie kombinovanej s tiažovými meraniami.

Integrál v rovnici (2.2) môže byť nahradený konečným počtom výškových rozdielov $\Delta H(\Omega'_i)$ z nivelácie a konečným počtom tiažových údajov $g(H, \Omega'_i)$ z tiažových meraní realizovaných v nivelačnom ťahu,

4. Normal orthometric height

The numerical value of the geopotential number $C(H, \Omega')$ is a result of levelling combined with gravity measurements.

The integral in the equation (2.2) can be replaced by finite elements of the height differences $\Delta H(\Omega'_i)$ from levelling and by finite discrete gravity values $g(H, \Omega'_i)$ from gravity measurements realised in a levelling line,

$$C(H, \Omega') = \int_{O(H=0,\ \Omega')}^{P(H,\ \Omega')} g(H, \Omega')\, dH(\Omega) = \sum_i g(H, \Omega'_i)\, \Delta H(\Omega'_i)\,. \tag{4.1}$$

Do tridsiatych rokov 20. storočia boli tiažové merania náročné a málo presné pretože k dispozícii boli iba kyvadlové gravimetre. Za týchto okolností boli v praxi používané normálne ortometrické výšky.

V definícii normálnej ortometrickej výšky $H^{NO}(\Omega)$ sú skutočné hodnoty tiaže $g(H, \Omega')$ na zemskom povrchu nahradené teoretickými hodnotami $\gamma(H, \varphi')$ normálneho tiažového zrýchlenia, takže platí

Until the 30-ies of the 20th century, the gravity measurements had been difficult and inaccurate because only pendulum gravimeter equipment were available. Under this circumstances the normal orthometric heights were used in practice.

The actual gravity values $g(H, \Omega')$ on the Earth's surface are replaced by theoretic values $\gamma(H, \varphi')$ of the normal gravity in the definition of the normal orthometric height $H^{NO}(\Omega)$, which is then given by the following formula

$$H^{NO}(\Omega) = \frac{1}{\bar{\gamma}(H, \varphi)} \int_{O(H=0,\ \Omega')}^{P(H,\ \Omega')} \gamma(H, \varphi')\, dH(\Omega')\,. \tag{4.2}$$

5. Dynamická výška

Dynamická výška $H^D(\Omega)$ je definovaná vzťahom

$$H^D(\Omega) = \frac{C(H, \Omega')}{\gamma_o(\varphi)}\,, \tag{5.1}$$

kde $\gamma_o(\varphi)$ je normálne tiažové zrýchlenie na rotačnom hladinovom elipsoide pre ľubovoľnú štandardnú zemepisnú šírku, obyčajne $\varphi = \pi/4$.

Dynamická výška sa odlišuje od geopotenciálnej kóty len v rozmere a v jednotkách. Delenie geopotenciálnej kóty konštantnou hodnotou $\gamma_o(\varphi)$ iba prevádza geopotenciálnu kótu na dĺžkovú jednotku.

6. Normálna výška

Určenie výšok z nivelácie a tiažových meraní bez hypotézy o rozložení hustoty topografických más je základným princípom Molodenského teórie normálnych výšok $H^N(\Omega)$, [9].

Nahradením strednej hodnoty $\bar{g}(H, \Omega)$ tiažového zrýchlenia strednou hodnotou normálneho tiažového zrýchlenia $\bar{\gamma}(H, \varphi)$ pozdĺž normály medzi referenčným elipsoidom a teluroidom (obr. 2) získame vzťah na definíciu normálnej výšky $H^N(\Omega)$ ako

$$H^N(\Omega) = \frac{C(H, \Omega')}{\bar{\gamma}(H, \varphi)}\,, \tag{6.1}$$

Stredná hodnota normálneho tiažového zrýchlenia $\bar{\gamma}(H, \varphi)$ pozdĺž ťažnice medzi teluroidom a referenčným elipsoidom môže byť vyjadrená Taylorovým rozvojom

5. Dynamic height

The dynamic height $H^D(\Omega)$ is defined as

$$H^D(\Omega) = \frac{C(H, \Omega')}{\gamma_o(\varphi)}\,, \tag{5.1}$$

where $\gamma_o(\varphi)$ is the normal gravity on the level rotation ellipsoid for an arbitrary standard latitude, usually $\varphi = \pi/4$.

Obviously, the dynamic height differs from the geopotential number only in a scale and in a unit. The division of the geopotential number by the constant value $\gamma_o(\varphi)$ just converts the geopotential number into a length.

6. Normal height

The determination of the heights from levelling and gravity measurements without any hypothesis about a density distribution of topographical masses is fundamental principle of Molodensky's theory of the normal height $H^N(\Omega)$, [9].

Replacing the mean value $\bar{g}(H, \Omega)$ of the gravity by the mean value of the normal gravity $\bar{\gamma}(H, \varphi)$ along the normal between the reference ellipsoid and the telluriod (Fig.2), we obtain the formula for the definition of the normal height $H^N(\Omega)$ as

$$H^N(\Omega) = \frac{C(H, \Omega')}{\bar{\gamma}(H, \varphi)}\,, \tag{6.1}$$

The mean value of the normal gravity $\bar{\gamma}(H, \varphi)$ is referred on the mid-point of the normal between the telluriod and the reference ellipsoid, so it can be expressed by Taylor series in the following form

$$\bar{\gamma}(H, \varphi) = \gamma(H, \varphi) - \frac{1}{2} \frac{\partial\, \gamma(H, \varphi)}{2\, \partial\, H(\Omega)}\, H^N(\Omega) + \ldots =$$

$$= \gamma_o(\varphi) + \frac{1}{2} \frac{\partial\, \gamma(H, \varphi)}{2\, \partial\, H(\Omega)} \Bigg|_{H(\Omega)=0} H^N(\Omega) + \frac{1}{4} \frac{\partial^2\, \gamma(H, \varphi)}{2\, \partial\, H(\Omega)^2} \Bigg|_{H(\Omega)=0} [H^N(\Omega)]^2 + \ldots. \tag{6.2}$$

Prvá derivácia $\partial\, \gamma / \partial\, H$ daná vzťahom (3.10) môže byť vyjadrená v tvare [5]

The first derivative $\partial\, \gamma / \partial\, H$ given by equation (3.10) can be rewritten as [5]

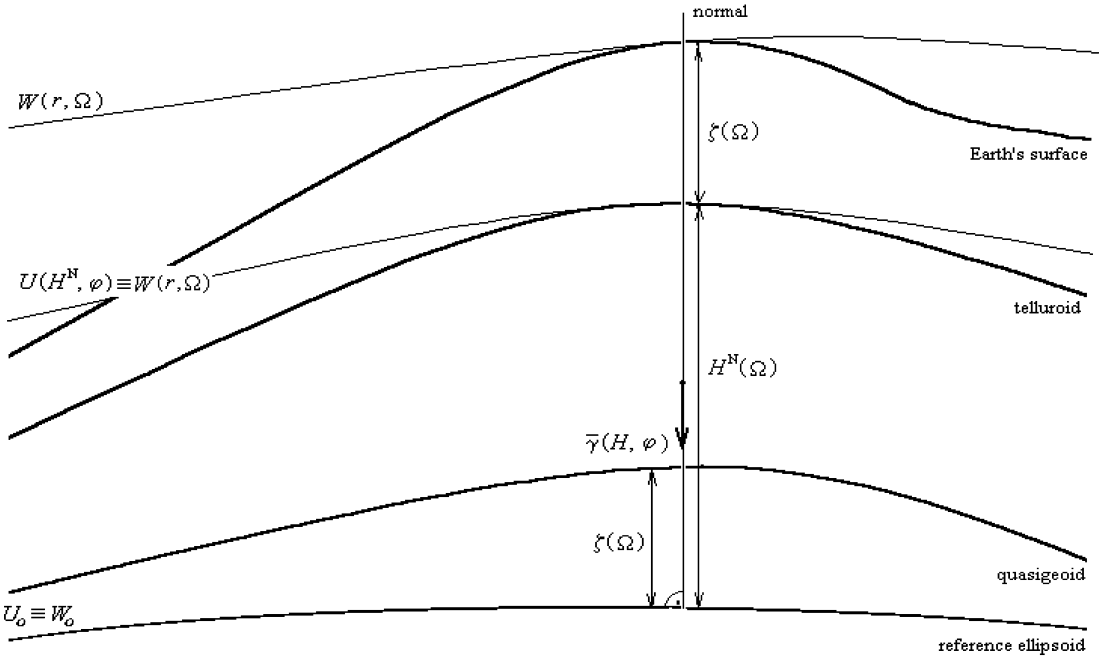

Obr. 2. Molodenského teória normálnych výšok
Fig. 2. Molodensky's theory of the normal height.

$$\left.\frac{\partial\,\gamma(H,\varphi)}{2\,\partial\,H(\Omega)}\right|_{H(\Omega)=0} = -\frac{2\gamma_o(\varphi)}{a}\left(1+f+\frac{\omega^2 a^2 b}{GM}-2f\sin^2\varphi\right). \tag{6.3}$$

Druhá derivácia $\partial\,\gamma^2/\partial\,H^2$ môže byť vyjadrená v sférickej aproximácii

$$\left.\frac{\partial^2\,\gamma(H,\varphi)}{2\,\partial\,H(\Omega)^2}\right|_{H(\Omega)=0} = \frac{6\gamma_o(\varphi)}{a^2}. \tag{6.4}$$

Substitúciou rovníc (6.3) a (6.4) do (6.2) dostaneme vzťah na výpočet normálneho tiažového zrýchlenia $\overline{\gamma}(H, \varphi)$ v nasledovnom tvare

The second derivative $\partial\,\gamma^2/\partial\,H^2$ can be described in the spherical approximation

$$\left.\frac{\partial^2\,\gamma(H,\varphi)}{2\,\partial\,H(\Omega)^2}\right|_{H(\Omega)=0} = \frac{6\gamma_o(\varphi)}{a^2}. \tag{6.4}$$

Substituting the equations (6.3) and (6.4) to the equation (6.2), we obtain the formula for the computation of the normal gravity $\overline{\gamma}(H, \varphi)$ in the following form

$$\overline{\gamma}(H,\varphi) = \gamma_o(\varphi)\left[1-\left(1+f+\frac{\omega^2 a^2 b}{GM}-2f\sin^2\varphi\right)\frac{H^N(\Omega)}{a}+\left(\frac{H^N(\Omega)}{a}\right)^2\right], \tag{6.5}$$

kde GM je geocentrická gravitačná konštanta a f je sploštenie referenčného elipsoidu.

Teluroid je povrch, ktorého normálny tiažový potenciál $U(H^N, \varphi)$ je rovný tiažovému potenciálu na zemskom povrchu. Kvázigeoid (nie je ekvipotenciálnou plochou) je daný výškovými anomáliami $\varsigma(\Omega)$ vztiahnutými k referenčnému elipsoidu.

Poznámka: J. Vignal [12] navrhol podobný výškový systém, kde stredná hodnota normálneho tiažového zrýchlenia je počítaná z normálneho tiažového zrýchlenia $\gamma_o(\varphi)$ na hladinovom rotačnom elipsoide v zmysle aproximácie vertikálneho gradientu normálneho tiažového zrýchlenia, pričom v tejto teórii je použitá iba prvá parciálna derivácia Taylorovho rozvoja (6.2)

where GM is the geocentric gravitational constant, and f is the flattening of the reference ellipsoid.

The surface, whose normal gravity potential $U(H^N, \varphi)$ is equal to the gravity potential on the Earth's surface is the telluroid. The quasigeoid (which is not equipotential surface) is given by heights anomalies $\varsigma(\Omega)$ referred on the reference ellipsoid.

Note: Vignal [12] proposed a similar system of heights, whereby the mean value of the normal gravity is evaluated from the normal gravity $\gamma_o(\varphi)$ on the level rotation ellipsoid by means of approximate vertical gradient of normal gravity. In this theory only the first partial derivative of the Taylor series (6.2) is used in the form

$$\overline{\gamma}(H,\varphi) = \gamma_o(\varphi) + \frac{1}{2}\left.\frac{\partial\,\gamma(H,\varphi)}{\partial\,H(\Omega)}\right|_{H(\Omega)=0} H^N(\Omega) = \gamma_o(\varphi) - \frac{\gamma_o(\varphi)}{a}\left(1+\frac{\omega^2 a^2 b}{GM}-2f\sin^2\varphi\right)H^N(\Omega). \tag{6.6}$$

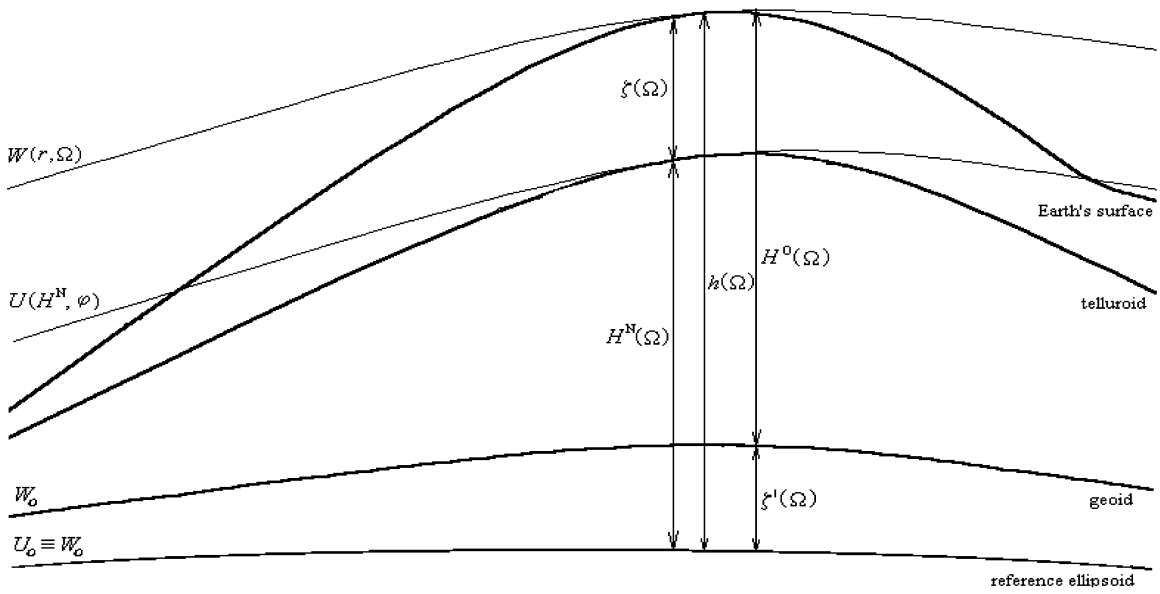

Obr. 3. Elipsoidická výška
Fig. 3. The ellipsoidal height

Na definíciu vzťahu medzi Molodenského normálnou výškou a Helmertovou ortometrickou výškou vyjadríme elipsoidickú výšku $h(\Omega)$ ako sumu normálnej výšky $H^N(\Omega)$ a výškovej anomálie $\varsigma(\Omega)$, podľa Molodenského teórie a ako sumu ortometrickej výšky $H^O(\Omega)$ a geoidickej výšky $\varsigma'(\Omega)$, (obr. 3)

$$h(\Omega) = H^N(\Omega) + \varsigma(\Omega) = H^O(\Omega) + \varsigma'(\Omega). \qquad (6.7)$$

Podľa W. H. Heiskanena a H. Moritza (1967) je rozdiel $\delta H(\Omega)$ medzi normálnou a ortometrickou výškou s dostatočnou presnosťou rovný [5]

To define relation between the Molodensky's normal height and Helmert's orthometric height, we define the ellipsoidal height $h(\Omega)$ as a sum of the normal height $H^N(\Omega)$ and height anomaly $\varsigma(\Omega)$ according to Molodensky's theory, and a sum of the orthometric height $H^O(\Omega)$ and geoidal height $\varsigma'(\Omega)$, respectively (Fig. 3)

$$h(\Omega) = H^N(\Omega) + \varsigma(\Omega) = H^O(\Omega) + \varsigma'(\Omega). \qquad (6.7)$$

According to Heiskanen and Moritz, (1967), the difference between the normal and orthometric height $\delta H(\Omega)$ is, with sufficient accuracy, equal to [5]

$$\delta H(\Omega) = H^N(\Omega) - H^O(\Omega) = \frac{C(H,\Omega)}{\bar{g}(H,\Omega)}\left[\frac{\bar{g}(H,\Omega) - \bar{\gamma}(H,\varphi)}{\bar{\gamma}(H,\varphi)}\right] = H^O(\Omega)\,\frac{\bar{g}(H,\Omega) - \bar{\gamma}(H,\varphi)}{\bar{\gamma}(H,\varphi)}. \qquad (6.8)$$

Výraz $\bar{g}(H,\Omega) - \bar{\gamma}(H,\varphi)$ je približne rovný jednoduchej Bouguerovej tiažovej anomálii $\Delta g^{SB}(H,\Omega)$ [8],

The term $\bar{g}(H,\Omega) - \bar{\gamma}(H,\varphi)$ is approximately equal to the simple Bouguer gravity anomaly $\Delta g^{SB}(H,\Omega)$ [8],

$$\bar{g}(H,\Omega) - \bar{\gamma}(H,\varphi) = g(H,\Omega) - \frac{1}{2}\frac{\partial\,\gamma(H,\varphi)}{\partial\,H(\Omega)}H^O(\Omega) - 2\pi G\rho_o H^O(\Omega) - \gamma(H,\varphi) + \frac{1}{2}\frac{\partial\,\gamma(H,\varphi)}{\partial\,H(\Omega)}H^N(\Omega) \cong$$

$$\cong g(H,\Omega) - \gamma(H,\varphi) - 2\pi G\rho_o H^O(\Omega) = \Delta g^{SB}(H,\Omega). \qquad (6.9)$$

Uvažujúc, že $g(H,\Omega) \approx \gamma(H,\varphi)$, môžeme nakoniec vyjadriť korekciu ortometrickej výšky na normálnu výšku v nasledovnom tvare

Assuming $g(H,\Omega) \approx \gamma(H,\varphi)$, we can finally describe the correction of the orthometric height to normal height in the following form

$$\delta H(\Omega) = H^O(\Omega)\,\frac{\Delta g^{SB}(H,\Omega)}{\bar{\gamma}(H/2,\varphi)} \cong -2\pi G\rho_o H^O(\Omega)\,\frac{H^O(\Omega)}{\bar{\gamma}(H/2,\varphi)} \approx -2\pi G\rho_o\,\frac{[H^O(\Omega)]^2}{\gamma_o(\varphi)}. \qquad (6.10)$$

7. Sumarizácia

Vzhľadom na geopotenciálnu kótu $C(H, \Omega')$ môžeme vyjadriť rozdielne typy výšok v prehľadnej forme:

- ortometrická výška: $$H^O(\Omega) = \frac{C(H, \Omega')}{\bar{g}(H, \Omega)}, \qquad (7.1)$$

- normálna výška: $$H^N(\Omega) = \frac{C(H, \Omega')}{\bar{\gamma}(H, \varphi)}, \qquad (7.2)$$

- dynamická výška: $$H^D(\Omega) = \frac{C(H, \Omega')}{\gamma_o(\varphi)}. \qquad (7.3)$$

Z tejto schémy vyplýva, že uvedené výškové systémy môžu byť získané delením geopotenciálnej kóty príslušnou hodnotou tiaže.

7. Summary

By means of the geopotential number (H, Ω'), we can describe different kinds of heights in a instructive form:

- orthometric height: $$H^O(\Omega) = \frac{C(H, \Omega')}{\bar{g}(H, \Omega)}, \qquad (7.1)$$

- normal height: $$H^N(\Omega) = \frac{C(H, \Omega')}{\bar{\gamma}(H, \varphi)}, \qquad (7.2)$$

- dynamic height: $$H^D(\Omega) = \frac{C(H, \Omega')}{\gamma_o(\varphi)}. \qquad (7.3)$$

From this scheme it is clear that the above mentioned height systems can be obtained by dividing the geopotential number by the relevant value of the gravity.

Literatúra - References

[1] BRUNS, H., 1878: *Die Figur der Erde.* Berlin, Publ. Preuss. Geod. Inst.

[2] BESSEL, F. W., 1837: *Ueber den Einfluss der Undergelmaessigkeiten der Figur der Erde auf geodaetische Arbeiten und ihre Vergleichung mit den Astronomischen Bestimmungen.* Astronomische Nachrichten, T.14., No. 269.

[3] BOMFORD, G., 1971: *Geodesy.* 3rd edition, Clarendon Press.

[4] GAUSS, C.F., 1828: *Bestimmung des Breitenunterschiedes zwischen den Sternwarten von Göttingen und Altona durch Beobachtungen am Ramsdenschen Zenithsector.* Vanderschoeck und Ruprecht, Göttingen.

[5] HEISKANEN, W. H., MORITZ, H., 1967: *Physical geodesy.* W.H. Freeman and Co., San Francisco.

[6] HELMERT, F. R., 1890: *Die Schwerkraft im Hochgebirge, insbesondere in den Tyroler Alpen.* Veröff. Königl. Preuss. Geod. Inst., No.1.

[7] LISTING, J. B., 1873: *Ueber unsere jetzige Kenntniss der Gestalt und Groesse der Erde.* Nachrichten von der Koening. Göttingen VLG der Dietrichschen Buchhandlung.

[8] MARTINEC, Z., 1993: *Effect of lateral density variations of topographical masses in view of improving geoid model accuracy over Canada.* Final report of contract DSS No. 23244-2-4356, Geodetic Survey of Canada, Ottawa.

[9] MOLODENSKY, M. S., 1945: *Fundamental problems of Geodetic Gravimetry,* (in Russian), TRUDY Ts NIIGAIK 42, Geodezizdat, Moscow.

[10] VANICEK, P., KRAKIWSKY, E., 1986: *Geodesy, The concepts* (second edition), Elsevier Science B.V., Amsterdam.

[11] VANICEK, P., KLEUSBERG, A., MARTINEC, Z., SUN, W., ONG, P., NAJAFI, M., VAJDA, P., HARRIE, L., TOMASEK, P., HORST, B., 1995: *Compilation of a precise regional geoid.* Final report on research done for the Geodetic Survey Division. Fredericton.

[12] VIGNAL, J. and KUKKAMÄKI, T. J., 1954: *Comptes rendus des travaux de la section des nivellements de précision.* Bull. Géod., supplement to Vol. 34.

Rastislav Lukáč – Viktor Fischer – Pavol Galajda *

MODELOVANIE ŠUMOVÝCH PROCESOV

MODELLING OF THE NOISE PROCESSES

V tomto článku je popísané modelovanie šumových procesov a ich aplikácia na oblasť spracovania obrazov, pričom pôsobenie šumu je prezentované a analyzované vzhľadom na matematické vyjadrenie, pôvod šumu, spôsobené vizuálne zmeny a možnosť redukcie šumu. V snahe čo najviac priblížiť účinok šumu je každý šumový proces doložený názornými obrázkami.

In this paper, the modelling of noise processes and their application to image processing are described. Thus, the noise effect on useful image information is presented and analysed according to mathematical formulas, the reason of its origin, introduced visual changes and the possibility of their reduction. In order to provide an unbiased view on the noise effect, noise models are supported by a number of object-lesson figures.

1. Úvod

Problém potláčania šumu je jednou z troch hlavných úloh spracovania signálov, ktoré sa zaoberajú odstraňovaním interferencie, analýzou a extrakciou charakteristík signálov a transformáciou signálov na formu vhodnejšiu pre ďalšie spracovanie. Dôvod prečo dochádza k interferencii šumu a užitočnej informácie sú rôzne [3], [4], [10], [17], [18], [24], napr. chyby prenosového kanála, starnutie záznamových médií, tepelné degenerácie, či človekom spôsobené rušenie.

Aby bolo možné odstrániť šum alebo interferenciu a navrhnúť filtračnú metódu [3], [6], [18], [25] so skutočne dobrým účinkom a vysokou presnosťou odhadu, je potrebné rešpektovať faktory ako mechanizmus generovania pôvodného signálu, povahu znehodnotenia a najmä mieru vhodnosti riešenia vzhľadom na pôvodný signál (alebo jeho mechanizmus generovania) a povahu znehodnotenia.

Pretože cieľom tohto článku je ukázať ako často sa vyskytujúce typy šumov znehodnocujú vizuálnu informáciu, neželateľné zmeny spôsobené šumom budú porovnávané s pôvodným obrazom Lena a jeho riadkovou funkciou (180-ty riadok), ktoré sú zobrazené na obr. 1.

Obr. 1. Pôvodný obraz Lena a jeho riadková funkcia (180-ty riadok)
Fig. 1. Original image Lena and corresponding row function (180^{th} row)

1. Introduction

The problem of the noise suppression is one of three main tasks [3] related to the signal processing, namely the removal of the interference, the analysis and the extraction of some signal characteristics, and finally, the transformation of signals into more suitable form for additional processing. The reasons why the interference of the noise occurs there and useful information are various [3], [4], [10], [17], [18], [24] such as the failures of the transmission channel, the ageing of recording media, thermal noise or man-made interference, etc.

In order to remove the noise or interference and design the filtering approach [3], [6], [18], [25] with a really good performance and high estimate precision, it is necessary to respect the following factors such as the mechanism generating the original signal, the nature of the corruption and finally, the measure of the accuracy of the solution with respecting the original noise (or its generating mechanism) and the nature of the corruption.

Since the aim of this paper is to show how the often occurring noise-types corrupt the visual information, the undesired changes caused by the noise will be compared with the original image Lena (2-D image signal) and its corresponding row function (180^{th} row), both shown in the Fig. 1.

* [1]Rastislav Lukáč, [2]Viktor Fischer, [1]Pavol Galajda
[1]Technical University of Košice, Faculty of Electronics and Informatics, Department of Electronics and Multimedia Communications, Park Komenského 13, 041 20 Košice, Slovak Republic, Tel.: ++421-55-6022863, Fax.: ++421-55-6323989, E-mail: lukacr@tuke.sk, Pavol.Galajda@tuke.sk
[2]Traitement du Signal et Instrumentation, 23 rue Paul Michelon, Tel.: ++33 0477481500, Fax: ++33 0477485120, E-mail: fischer@univ-st-etienne.fr

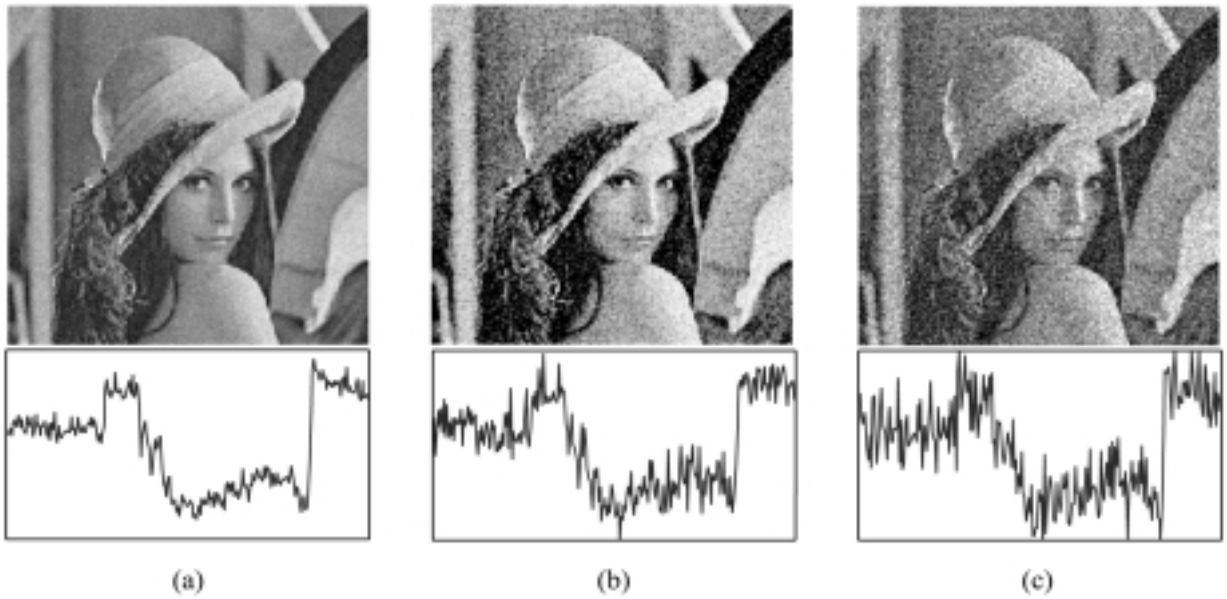

Obr. 2. Aditívny Gaussov šum s nulovou strednou hodnotou (a) $\sigma = 10$ (b) $\sigma = 20$ (c) $\sigma = 30$
Fig. 2. Gaussian noise with zero mean (a) $\sigma = 10$ (b) $\sigma = 20$ (c) $\sigma = 30$

2. Aditívny Gaussov šum

Najjednoduchším, avšak najdôležitejším typom šumu je aditívny Gaussov šum definovaný pomocou [3],[31]

$$\{x_1, x_2, ..., x_N\} = \{o_1, o_2, ..., o_N\} + \{v_1, v_2, ..., v_N\}, \qquad (1)$$

kde $\{x_1, x_2, ..., x_N\}$ reprezentuje znehodnotený signál, $\{o_1, o_2, ..., o_N\}$ je pôvodný signál a $\{v_1, v_2, ..., v_N\}$ je šumová zložka. Poznamenávame, že v_i sú nezávislé od o_i. V prípade, že v_i sú navzájom nezávislé a identicky distribuované náhodné premenné, hovoríme o aditívnom bielom Gaussovom šume.

V prípade znehodnotenia obrazov aditívnym Gaussovym šumom, náhodná premenná s Gaussovym rozložením (s nulovou strednou hodnotou μ a určitou smerodajnou odchýlkou σ (obr. 3)) je pridaná ku každej pôvodnej vzorke (obr. 2). Ľahko môžeme určiť, že interval náhodných hodnôt sa rozširuje s rastom smerodajnej odchýlky a zároveň tak narastá aj stupeň znehodnotenia. Matematicky je Gaussov šum definovaný vzťahom

$$f(a) = \frac{1}{\sigma\sqrt{2\pi}} \exp\left(-\frac{1}{2}\left(\frac{a-\mu}{\sigma}\right)\right). \qquad (2)$$

Je zrejmé, že malé náhodné hodnoty sú pridané s veľkou pravdepodobnosťou. Na druhej strane, veľké náhodné hodnoty nie sú veľmi časté. Na generovanie náhodnej hodnoty sa využíva rovnica

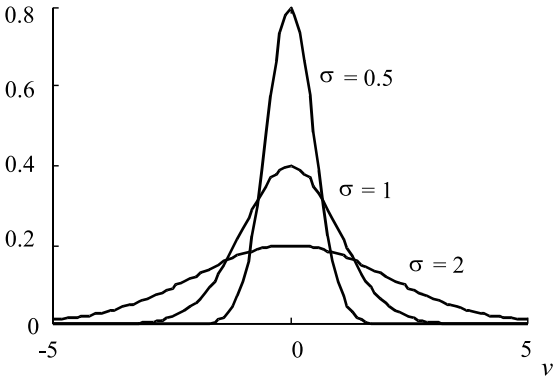

Obr. 3. Aditívny Gaussov šum
Fig. 3. Additive Gaussian noise

2. Additive Gaussian Noise

The simplest, however, the most important noise type is an additive Gaussian noise defined by [3],[31]

$$\{x_1, x_2, ..., x_N\} = \{o_1, o_2, ..., o_N\} + \{v_1, v_2, ..., v_N\}, \qquad (1)$$

where $\{x_1, x_2, ..., x_N\}$ represent the corrupted signal, $\{o_1, o_2, ..., o_N\}$ is an original and $\{v_1, v_2, ..., v_N\}$ is a noisy component. Note that v_i are independent on o_i. In the case that v_i are mutually independent and identically distributed normal random variables, then it is the case of additive white Gaussian noise.

For the additive Gaussian image corruption, a random value with Gaussian distribution (with zero mean μ and some standard deviation σ (Fig. 3)) is added to each original sample (Fig. 2). It can be seen that the interval of random values extends with increasing the standard deviation and thus, the degree of the noise corruption is increased, too. Mathematically, the Gaussian noise is defined by

$$f(a) = \frac{1}{\sigma\sqrt{2\pi}} \exp\left(-\frac{1}{2}\left(\frac{a-\mu}{\sigma}\right)\right). \qquad (2)$$

It is clear that the small random values are added with a high probability and, on the other hand, the large values are not too frequent. For a random value generation, there is utilised the following equation

$$a = \sqrt{-2\ln/(r_1)}\cos(\pi(2r_2 - 1)). \quad (3)$$

kde r_1 a r_2 sú náhodné hodnoty s uniformným rozdelením.

Vzájomný vzťah medzi pôvodnou a šumovou zložkou je vyjadrený ich súčtom. Z tohto dôvodu je možné tieto zložky od seba oddeliť. Na efektívne potlačenie aditívneho Gaussového šumu sú uprednostňované najmä lineárne filtre (napr. Wienerove filtre [29]), ktoré spĺňajú vlastnosť superpozície. Okrem Wienerovych filtrov možno použiť aj Kalmanove filtre [19],[30], rozličné filtre založené na LMS algoritme [8],[28], či hybridné FIR-mediánové filtre [22]. Tieto filtre môžeme úspešne použiť na odstraňovanie tepelného šumu (alebo šumu spôsobeného vplyvom tepelných degenerácií materiálu) [3], ktorý je modelovaný ako biely Gaussov šum.

3. Impulzový šum

Na rozdiel od aditívneho Gaussovho šumu a multiplikatívneho šumu (vzniká v snímacích systémoch), kde vzájomný vzťah medzi pôvodnou a šumovou zložkou je vyjadrený pomocou ich súčtu alebo súčinu, existujú zložitejšie typy šumu. Ak šum postihne len časť z celkového počtu vzoriek, zatiaľ čo ostatné vzorky ostanú nepoškodené, ide o poškodenie s charakterom impulzového šumu [3], [4], [10]. Impulzový šum zvyčajne spôsobuje vysokofrekvenčné zmeny alebo lepšie povedané impulzy, na ktoré je ľudský vizuálny systém veľmi citlivý.

V modernej komunikačnej teórii alebo tiež aj pri A/D konverzii [5], [16], [17], impulzový šum je často modelovaný pomocou modelu bitových chýb [3]

$$^{*}k_{i,j}^{m} = \begin{cases} k_{i,j}^{m} & 1 - p_v \\ 1 - k_{i,j}^{m} & p_v \end{cases}, \quad (4)$$

kde i, j charakterizujú pozíciu vzorky, m je bitová úroveň ohraničená intervalom 1 až B (počet bitov na vzorku), p_v je pravdepodobnosť bitových chýb, $\{k\}$ a $\{^{*}k\}$ označujú pôvodné a zašumené hodnoty bitov. Originálna vzorka je vyjadrená ako

$$o_{i,j} = {}^{*}k_{i,j}^{1}\,2^{B-1} + k_{i,j}^{2}\,2^{B-2} + \ldots + k_{i,j}^{B-1}2 + k_{i,j}^{B}, \quad (5)$$

zatiaľ čo vzorka zo zašumeného obrazu je definovaná podľa

$$x_{i,j} = {}^{*}k_{i,j}^{1}\,2^{B-1} + k_{i,j}^{2}\,2^{B-2} + \ldots + {}^{*}k_{i,j}^{B-1}2 + {}^{*}k_{i,j}^{B}. \quad (6)$$

Pri spracovaní obrazov je impulzový šum zvyčajne modelovaný pomocou modelu s podobným efektom ako (4), avšak trochu zjednodušeným. Matematický model impulzového šumu s premenlivou hodnotou (pozri obr.4) môže byť vyjadrený podľa [11]

$$x_{i,j} = \begin{cases} v & \text{with probability } p \\ o_{i,j} & \text{with probability } p - 1 \end{cases}, \quad (7)$$

kde i, j charakterizujú pozíciu vzorky, $o_{i,j}$ je vzorka z pôvodného obrazu, $x_{i,j}$ reprezentuje vzorku zo zašumeného obrazu, p je pravdepodobnosť zašumenia a v je hodnota šumu, ktorou je nahradená pôvodná vzorka.

$$a = \sqrt{-2\ln/(r_1)}\cos(\pi(2r_2 - 1)). \quad (3)$$

where r_1 and r_2 are random values with the uniform distribution.

Since the relationship between the original and the noise component is expressed through an addition, it is possible to separate both signals. For the effective suppression of additive Gaussian noise are preferred especially linear filters (e.g. Wiener filters [29]) that satisfy the superposition property. Besides Wiener filters it is possible to use Kalman filters [19],[30], various LMS-based filters [8],[28] and hybrid median FIR filters [22]. These filters can be used successfully for removing the thermal noise (or the noise caused by thermal generation of materials) [3] that is modelled as a white Gaussian noise.

3. Impulse Noise

Unlike the additive Gaussian noise and the multiplicative noise (origin in some acquisition systems), where the relationship between the original and the noise component is expressed through an addition and a product, respectively, there exist more complex noise types. If the noise corruption affects a number of samples whereas other samples remain unchanged, it is some kind of an impulse noise [3], [4], [10]. Usually, the impulse noise causes the high frequency changes or in other words impulses on which the human visual system is more sensitive.

In modern communication theory or in A/D conversion [5], [16], [17], the impulse corruption is often modelled through a model of bit errors given by [3]

$$^{*}k_{i,j}^{m} = \begin{cases} k_{i,j}^{m} & 1 - p_v \\ 1 - k_{i,j}^{m} & p_v \end{cases}, \quad (4)$$

where i, j characterise the sample position, m is a bit level forced to be between 1 and B (a number of bits per sample), p_v is a bit error probability $\{k\}$ and $\{^{*}k\}$ finally and characterise original and corrupted bit levels. Note that the original sample is expressed as

$$o_{i,j} = {}^{*}k_{i,j}^{1}\,2^{B-1} + k_{i,j}^{2}\,2^{B-2} + \ldots + k_{i,j}^{B-1}2 + k_{i,j}^{B}, \quad (5)$$

whereas a sample from noisy image is defined by

$$x_{i,j} = {}^{*}k_{i,j}^{1}\,2^{B-1} + k_{i,j}^{2}\,2^{B-2} + \ldots + {}^{*}k_{i,j}^{B-1}2 + {}^{*}k_{i,j}^{B}. \quad (6)$$

Usually, in image processing applications, the impulse noise is modelled through a model with a similar effect as (4), however, a little simplified. To achieve a noise corruption with variable value (see Fig.4), also called random-valued impulse noise, the mathematical model can be expressed as [11]

$$x_{i,j} = \begin{cases} v & \text{with probability } p \\ o_{i,j} & \text{with probability } p - 1 \end{cases}, \quad (7)$$

where i, j characterise the sample position, $o_{i,j}$ is the sample from the original image, $x_{i,j}$ represents the sample from the noisy image, p is a corruption probability and v is a noise intensity replacing the original value.

Poznamenávame, že náhodná hodnota je vzorka z celého rozsahu možných hodnôt. V prípade reprezentácie obrazu 8 bitmi na vzorku, t. j. 256 kvantizačnými úrovňami, hodnota je z intervalu 0 až 255.

Notice that a random value is a sample from the whole range of possible intensities. In the case of 8bit per sample image representation, i.e. 256 quantization levels, the value is from 0 to 255.

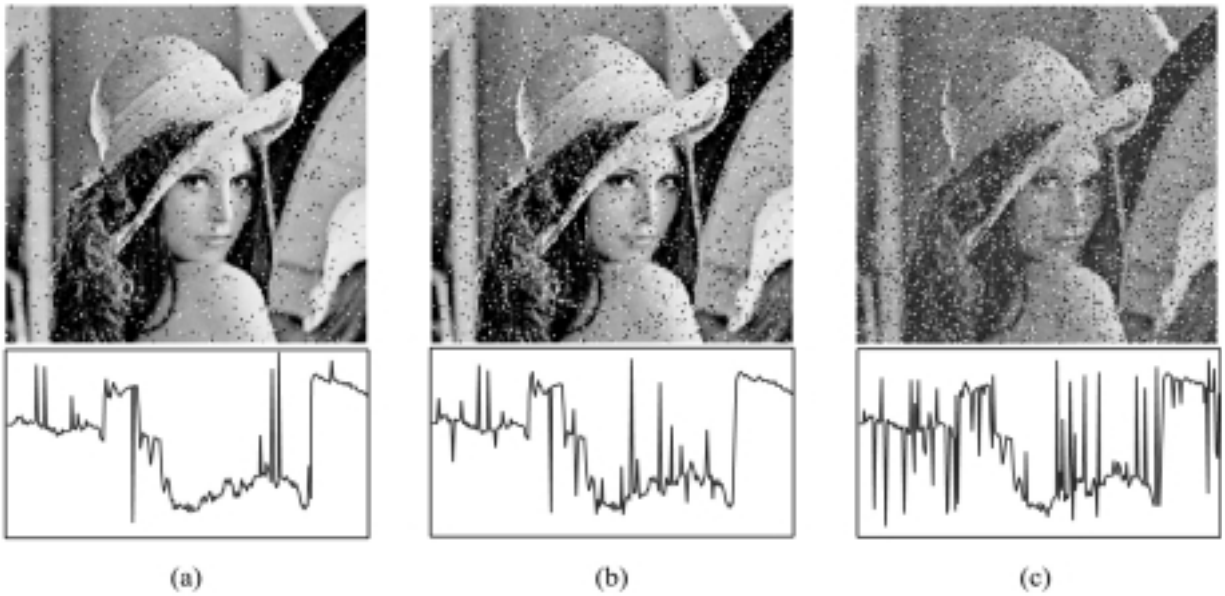

Obr.4 Impulzový šum s premenlivou hodnotou (a) $p = 0{,}05$ (b) $p = 0{,}10$ (c) $p = 0{,}20$
Fig. 4 Random-valued impulse noise (a) $p = 0.05$ (b) $p = 0.10$ (c) $p = 0.20$

Ďalší typ impulzového šumu, nazývaný aj ako čiernobiely šum, je charakterizovaný dvoma náhodnými hodnotami, konkrétne 0 a 255. Uvedené znehodnotenie je možné matematický zapísať vzťahom

The second impulse noise type also called as salt and pepper noise, where the impulses can be equal to 0 and 255, only, is determined by [4]

$$x_{i,j} = \begin{cases} 0 & p_0 \\ 255 & p_{255} \\ o_{i,j} & 1 - (p_0 + p_{255}) \end{cases} \quad (8)$$

kde p_0 a p_{255} sú pravdepodobnosti výskytu minimálnej (0) a maximálnej (255) hodnoty. Je zrejmé, že impulzy sa prejavujú vo forme bielych a čiernych bodiek.

Okrem bitových chýb, impulzového šumu s premenlivou hodnotou a čiernobieleho impulzového šumu existujú rôzne typy impulzového šumu s konštantnou hodnotou, pri ktorých dochádza k nahradeniu pôvodnej hodnoty stále rovnakou hodnotou šumu. Vo všeobecnosti, na potláčanie impulzového šumu sa používa veľká trieda poriadkovo-štatistických filtrov. Trieda nelineárnych filtrov založených na poriadkových štatistikách, využíva zoraďovanie [22] vstupných vzoriek určených oknom filtra. Okrem robastného odhadu mediánom zoradenej množiny, výbornými schopnosťami potlá-

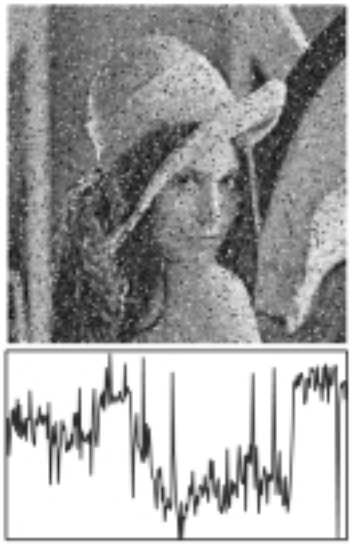

Obr. 5. Zmiešaný šum ($\mu = 0$, $\sigma = 32$, $p = 0{,}1$)
Fig. 5. Mixed noise ($\mu = 0$, $\sigma = 32$, $p = 0.1$)

$$x_{i,j} = \begin{cases} 0 & p_0 \\ 255 & p_{255} \\ o_{i,j} & 1 - (p_0 + p_{255}) \end{cases} \quad (8)$$

where p_0 and p_{255} are probabilities of the occurrence for minimum value (0) and maximum value (255). It is clear that the impulses are represented by black and white spots.

Besides bit errors, random valued impulse noise and salt and pepper noise, there exist some additional constant-valued impulse noises, where the original values are replaced by the constant value. A sufficient tool for the suppression of all impulse noise types was proved by a large family of order-statistic filters. A class of nonlinear filters based on the order-statistic theory utilises the ordering [22] of the input samples spanned by a filter window. Besides the robust estimation given by a median value [11], [32] of ordered set, the

čania impulzového šumu sa môžu vyznačovať vážené mediánové filtre [32], vyhladzovacie LUM filtre [11], [13], kompozičné filtre [7], [13], [23] a široká trieda optimálnych poriadkovo-štatistických filtrov kombinovaná s neurónovými sieťami [6],[20], fuzzy logikou [15], [25] alebo optimalizovaná genetickými algoritmami [18], [25].

4. Zmiešaný šum

Existujú situácie, kedy dochádza k poškodeniu užitočnej informácie šumom pochádzajúcim z viacerých zdrojov. Typickým príkladom je tepelný šum sprevádzaný bitovými chybami (obr. 5). Pre takéto prípady môže byť rozloženie šumu modelované pomocou [26]

$$x_{i,j} = \begin{cases} \upsilon & \text{with probability } p \\ o_{i,j} + n_{i,j} & \text{with probability } p - 1 \end{cases} \quad (9)$$

kde i, j charakterizujú pozíciu vzorky, $n_{i,j}$ je vzorka s aditívnym Gaussovym šumom, p je pravdepodobnosť výskytu impulzu υ a je hodnota impulzu. Podobne ako (9), možno modelovať (obr. 6) zmiešaný šum pomocou aditívneho Gaussovho šumu a čiernobieleho impulzového šumu. Na obr. 6 spojitá charakteristika je asociovaná s Gaussovym rozložením, zatiaľ čo disktrétna charakteristika (impulzy v hodnote 0 a 255) je asociovaná s čiernobielym impulzovým šumom.

Obr. 6. Rozloženie zmiešaného šumu
Fig. 6. Mixed noise distribution

Na efektívne potlačenie zmiešaného šumu modelovaného pomocou (9) sa zvyčajne používajú poriadkovo-štatistické L filtre a Ll filtre [22].

excellent impulse noise attenuation capabilities can be provided by weighted median filters [32], LUM smoothers [11], [13], stack filters [7], [13], [23], etc. and a wide range of optimal order-statistic filters combined with neural networks [6], [20], fuzzy logic [15], [25] or optimised by genetic algorithms [18], [25].

4. Mixed noise

There exist some situations, where useful information is corrupted by the noise coming from different sources. The typical example is thermal noise followed by the bit errors (Fig.5). Then, the noise distribution can be modelled as [26]

$$x_{i,j} = \begin{cases} \upsilon & \text{with probability } p \\ o_{i,j} + n_{i,j} & \text{with probability } p - 1 \end{cases} \quad (9)$$

where i, j characterise the sample position, $n_{i,j}$ is the additive Gaussian noise, p is an impulse probability and υ is an impulse intensity. Similarly to (9), it is possible to model (Fig. 6) the mixed noise consisting of the additive Gaussian noise and salt and pepper noise. Notice that the continuous characteristic is associated with Gaussian distribution, whereas the discrete characteristic (spikes in 0 and 255 intensities) is associated with the salt and pepper noise.

In order to suppress the mixed noise modelled as (9) effectively, a class of order-statistic L filters and Ll filters is usually preferred [22].

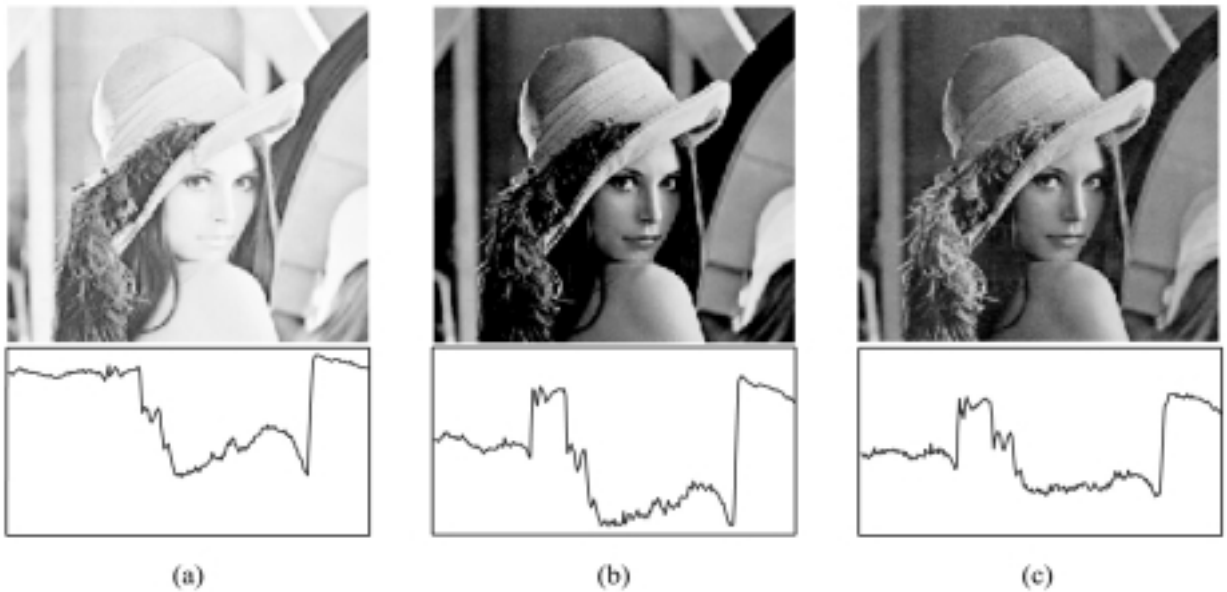

Obr. 7. Pôvodný farebný obraz Lena rozložený na farebné kanály (a) R kanál (b) G kanál (c) B kanál
Fig. 7. Decomposed original color image Lena (a) R channel (b) G channel (c) B channel

5. Impulzový šum pre M-D obrazové signály

Ak šum postihne viacrozmerné (M-D) obrazové signály, napr. farebné obrazy alebo obrazové sekvencie, šumový model by mal zahrnúť aj koreláciu medzi farebnými kanálmi alebo snímkami sekvencie. Vyššie uvedené obmedzenie sa vzťahuje na všetky prezentované šumové modely, avšak, aby sme čo najlepšie zdôraznili rozdiel medzi modelom s rešpektovaním korelácie a modelom bez uvažovania vnútornej korelácie, v ďalšom budeme využívať len model impulzového šumu s premenlivou hodnotou.

5. Impulse Noise for M-D image signals

If the noise affects the multidimensional (M-D) image signals such as color images or image sequences, the noise should be modelled with considering the correlation between the color channels or image frames, respectively. The above-mentioned restriction is related to all proposed noise models, however, in order to provide the best visual comparison between models with and without respecting the inherent correlation, in the rest of this paper the random-valued impulse noise is considered.

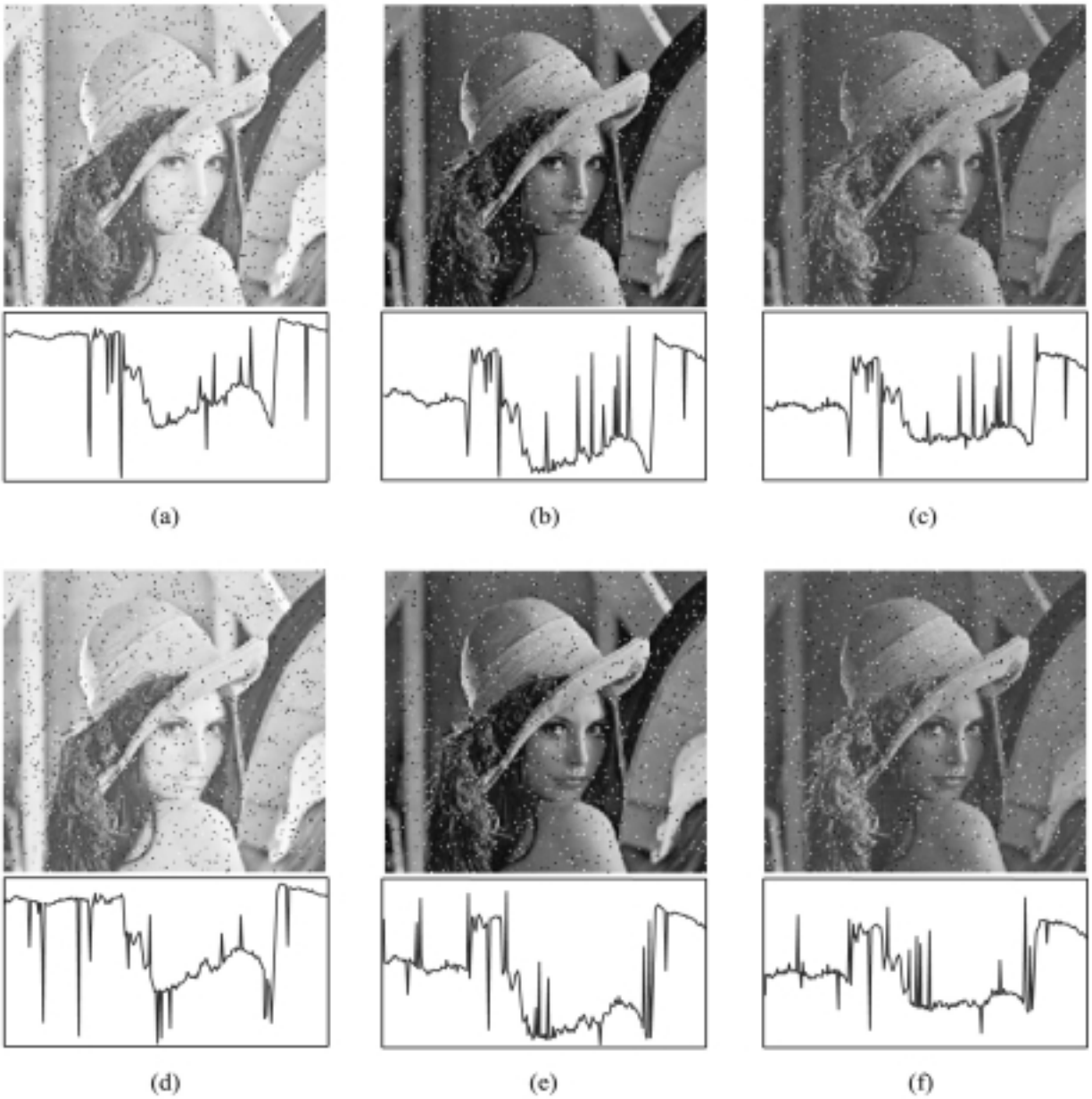

Obr. 8. Impulzový šum s premenlivou hodnotou p = 0,1 (a-c) Plne korelovaný šum (d-e) Nekorelovaný šum
Fig. 8. Random-valued impulse noise p = 0.1 (a-c) Fully-correlated noise (d-e) Non-correlated noise

V tejto chvíli pristúpime k analýze modelu impulzového šumu pre farebné obrazy. Vzhľadom na farebné obrazy, t. j. vektorovo-hodnotové obrazové signály [2], [10], každý obrazový bod (vzorka) môže byť uvažovaný ako vektor troch zložiek. V prípade RGB (červená – zelená – modrá) farebnej sústavy, uvažujeme vektor hodnôt z R, G a B farebných kanálov. Z tohto dôvodu je potrebné uvažovať koreláciu medzi farebnými kanálmi, pretože šum môže postihovať každý farebný kanál inou mierou.

Uvažujme dvojkanálový signál. Nech v je náhodná hodnota impulzu a p je pravdepodobnosť impulzu. Nech je p_1 pravdepodobnosť impulzu asociovaná s prvým kanálom p_2 a pravdepodobnosť impulzu asociovaná s druhým kanálom. Potom, matematický model impulzového šumu [21] môže byť definovaný vzťahom

$$x_{i,j} = \begin{cases} [o^1_{i,j}, o^2_{i,j}] & \text{with probability } 1-p \\ [v, o^2_{i,j}] & \text{with probability } p_1 \cdot p \\ [o^1_{i,j}, v] & \text{with probability } p_2 \cdot p \\ [v, v] & \text{with probability } p \cdot (1-p_1-p_2) \end{cases} \quad (10)$$

kde $o^1_{i,j}$, $o^2_{i,j}$ sú pôvodné hodnoty prvého a druhého kanála. Avšak výraz (10) je relatívne zložitý pre štandardné farebné obrazy, t. j. pre trojkanálový prípad. Z tohto dôvodu je nasledujúca definícia [10], [14] prirodzenejšia

$$x_{i,j} = \begin{cases} v & \text{with probability } p_v \\ o_{i,j} & \text{with probability } 1-p_v \end{cases} \quad (11)$$

kde i, j charakterizujú pozíciu vzorky, $o_{i,j}$ je vzorka (vektor) z pôvodného obrazu, $x_{i,j}$ je vzorka zo zašumeného obrazu, p_v je pravdepodobnosť poškodenia a $v = (v_R, v_G, v_B)$ je šumový vektor náhodných hodnôt. Ak zložky vektora sú generované nezávislo od seba, šedé impulzy, t. j. rovnaké hodnoty vo všetkých farebných kanáloch sa môžu vyskytnúť len v špeciálnom prípade (pozri obr. 8).

Uvažujme obrazové sekvencie. Pretože obrazové sekvencie predstavujú časové sekvencie dvojrozmerných (2-D) obrazov, t. j. priestorovo-časové dáta, šumový model by mal rešpektovať vnútornú koreláciu. Z tohto pohľadu je možné znehodnotiť snímky sekvencie nezávisle od predchádzajúcich a budúcich snímok, alebo môže byť šum v za sebou idúcich snímkach korelovaný vzhľadom na pozíciu impulzu a tiež aj hodnotu impulzu. Vhodný model impuIzového šumu získame nepatrnou modifikáciou výrazu (10).

Úspešnosť odstraňovania impulzového šumu v M-D obrazových signáloch závisí od rešpektovania rozmernosť signálu a od vnútornej korelácie signálu. Teda, farebné obrazy by mali byť filtrované vektorovými prístupmi [2], [10], [12], zatiaľ čo pre obrazové sekvencie sú výborné výsledky dosahované časovo-priestorovými (3-D) filtrami [1], [9], [11], [27].

6. Zhrnutie

Tento článok bol zameraný na modelovanie šumových procesov, najmä pre obrazové aplikácie. Okrem matematických vyjad-

Now, the impulse noise model for color images is analysed. Concerning the color images, i.e. vector-valued image signals [2], [10], each image point can be considered as a vector of three components. In the case of RGB (red-green-blue) color space, it is a vector of intensities from R, G and B color channels (Fig. 7). Thus, there is necessary to consider the correlation between the color channels, since the noise can affect each color channel with a different measure.

Consider the two-channel signal. Let v be a random impulse intensity and p an impulse probability. Let p_1 be an impulse probability associated with the first channel and p_2 with the second channel. Then, the mathematical model of the impulse noise can be defined as [21]

$$x_{i,j} = \begin{cases} [o^1_{i,j}, o^2_{i,j}] & \text{with probability } 1-p \\ [v, o^2_{i,j}] & \text{with probability } p_1 \cdot p \\ [o^1_{i,j}, v] & \text{with probability } p_2 \cdot p \\ [v, v] & \text{with probability } p \cdot (1-p_1-p_2) \end{cases} \quad (10)$$

where $o^1_{i,j}$, $o^2_{i,j}$ are original values of the first channel and the second channel, separately. However, the expression (10) is relatively complex for standard color images, i.e. the three-channel case. For that reason, the following definition [10],[14] for vector-valued signals is more natural

$$x_{i,j} = \begin{cases} v & \text{with probability } p_v \\ o_{i,j} & \text{with probability } 1-p_v \end{cases} \quad (11)$$

where i, j characterise the sample position, $o_{i,j}$ is the sample from the original image, $x_{i,j}$ represents the sample from the noisy image, p_v is a corruption probability and $v = (v_R, v_G, v_B)$ is a noise vector of intensity random values. If single components of the vector are generated independently, the gray impulses, i.e. the same value in all channels, can occur in the special case, only (see Fig. 8).

Let us consider the image sequences. Since, image sequences represent the time sequences of two-dimensional (2-D) images, i.e. spatiotemporal data, the noise model should respect the inherent correlation. Thus, it is possible to model the noise in two ways such as to corrupt each frame independently without knowing the previous and future frames or the noise in the followed frames can be correlated in the sample position and the noise intensities, too. In order to express the impulse noise, it is sufficient to slightly modify definition (10).

Usually, in M-D image signals the successful noise attenuation depends on respecting the signal dimensionality and the inherent correlation of the signal. It means that color images should be filtered by vector approaches [2], [10], [12], whereas the excellent denoising approaches for image sequences are related to spatiotemporal (3-D) filters [1], [9], [11], [27].

6. Conclusion

This paper has focused on the noise modelling, especially for the image applications. Besides mathematical expressions, a number

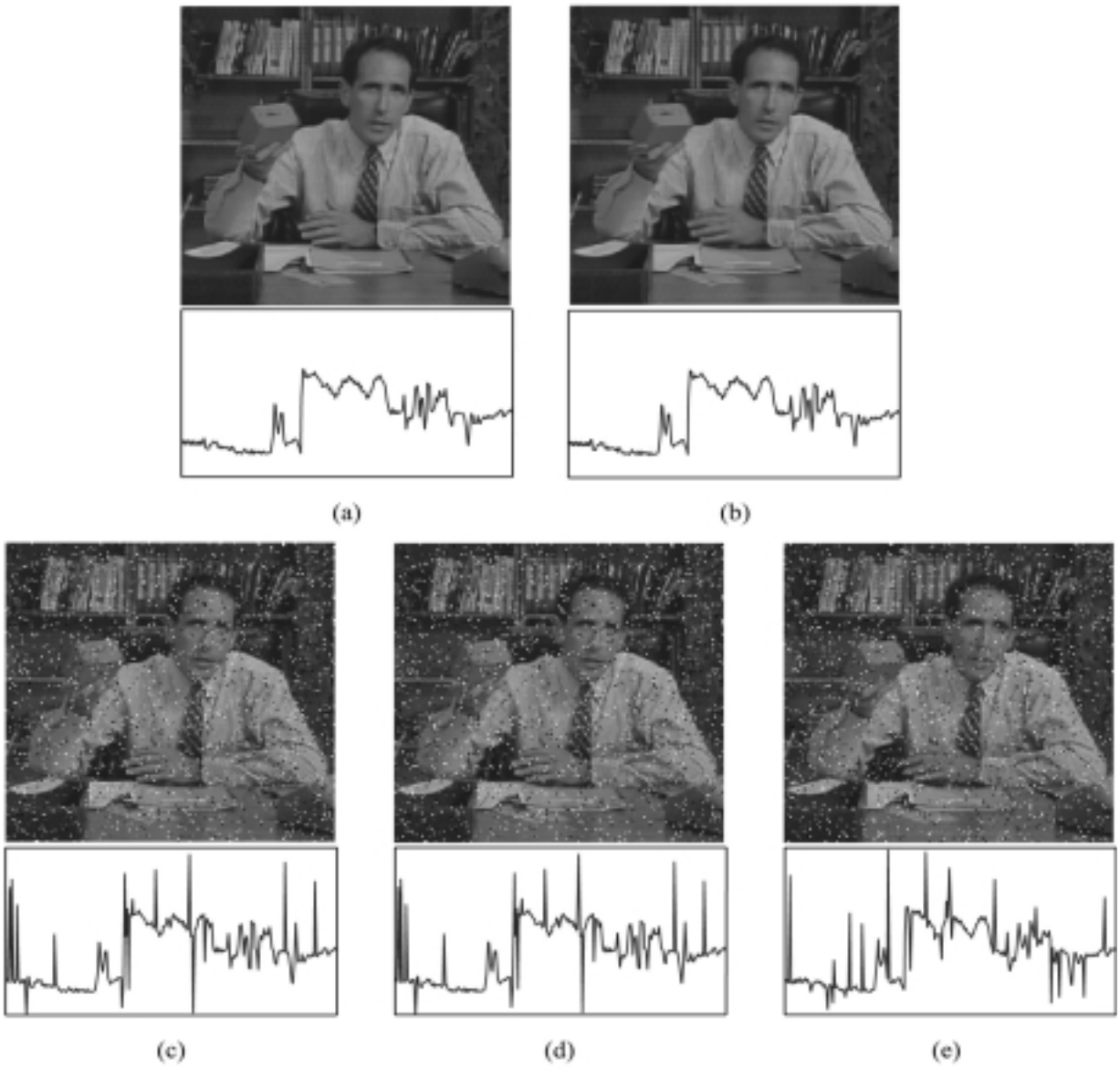

Obr. 9. Sekvencia (a) 5-ta snímka pôvodnej sekvencie (b) 6-ta snímka pôvodnej sekvencie (c) 5-ta snímka zašumenej sekvencie (d) 6-ta snímka zašumenej sekvencie plne korelovaná vzhľadom na 5 snímku čo do pozície a hodnoty šumu (e) 6-ta snímka zašumenej sekvencie zašumenej nezávisle od 5-tej snímky

Fig. 9. Sequence (a) 5th frame of original sequence (b) 6th frame of original sequence (c) 5th frame of noisy sequence (d) 6th frame of noisy sequence with full correlation in the sample position (e) 6th frame of noisy sequence corrupted independently

rení boli v článku prezentované aj názorné príklady, ďalej boli určené príčiny vzniku šumu a diskutované metódy pre potláčanie rôznych typov šumu. Vzhľadom na znalosti o charaktere šumových procesov je možné navrhnúť skutočne dobrú filtračnú metódu.

of typical figures, the determination of the noise origin and tools for the suppression of various noise types have been presented, too. According to knowing the character of the noise process, it is more possible to design a really good filtering approach.

Literatúra – References

[1] ARCE, G. R.: *Multistage Order Statistic Filters for Image Sequence Processing.* IEEE Transactions on Signal Processing, Vol. 39, No. 5, May 1991, pp. 1146-1163.

[2] ASTOLA, J., HAAVISTO, P., NEUVO, Y.: *Vector Median Filters.* Proceedings of the IEEE, Vol. 78, No. 4, April 1990, pp. 678-689.

[3] ASTOLA, J., KUOSMANEN, P.: *Fundamentals of Nonlinear Digital Filtering*, CRC Press LLC, 1997.
[4] BERNSTEIN, R.: *Adaptive Nonlinear Filters for Simultaneous Removal of Different Kinds of Noise in Images,* IEEE Transactions on Circuits and Systems, Vol. Cas-34, No. 11, November 1987, pp. 1275-1291.
[5] DAPONTE, P., HOLCER, R., HORNIAK,L., MICHAELI,L.: *Using the Interpolations Method for Noise Shaping AD Converters,* Proceedings of the 6-th Euro Workshop on ADC Modelling and Testing EWADC '2001 in Lisbon, Portugal, September 13-14, 2001, pp. 134-137
[6] DRUTAROVSKÝ, M.: *Neurónové vážené poriadkové štatistické filtre na báze dekompozičnej architektúry.* Kandidátska dizertačná práca, Košice, Jún 1995.
[7] FITCH, J. P., COYLE, E. J., GALLAGHER, N. C.: *Median Filtering by Threshold Decomposition.* IEEE Transactions on Acoustics Speech and Signal Processing, Vol. ASSP-32, No. 6, December 1984, pp. 1183-1189.
[8] HADHOUD, M. M., THOMAS, D. W.: *The Two-Dimensional Adaptive LMS (TDLMS) Algorithm.* IEEE Transactions on Circuits Systems, Vol. 35, May 1988, pp. 485-494.
[9] KLEIHORST, R. P., LAGENDIJK, R.L., BIEMOND, J.: *Noise Reduction of Image Sequences Using Motion Compensation and Signal Decomposition,* IEEE Trans. on Image Processing, Vol. 4, No. 3, 1995, pp. 274-284
[10] LUKÁČ, R.: *Vector LUM Smoothers as Impulse Detector for Color Images.* Proceedings of European Conference on Circuit Theory and Design ECCTD '01 "Circuit Paradigm in the 21st Century" in Espoo, Finland, August 28-31, 2001, Vol. III, pp. 137 - 140.
[11] LUKÁČ, R. - MARCHEVSKÝ, S.: *LUM Smoother with Smooth Control for Noisy Image Sequences.* EURASIP Journal on Applied Signal Processing, Vol. 2001 (7), No. 2, 2001, pp. 110-120.
[12] LUKÁČ, R. - MARCHEVSKÝ, S.: *Adaptive Vector LUM Smoother.* Proceedings of the 2001 IEEE International Conference on Image Processing ICIP 2001 in Thessaloniki, Greece, October 7-10, 2001, Vol. 1, pp. 878-881.
[13] LUKÁČ, R. - MARCHEVSKÝ, S.: *Boolean Expression of LUM Smoothers.* IEEE Signal Processing Letters, Vol. 8, No. 11, November 2001, pp. 292-294.
[14] LUKÁČ, R.: *Adaptive Impulse Noise Filtering by Using Center-Weighted Directional Information.* Proceedings of the 1st European Conference on Color in Graphics, Image and Vision CGIV '2002 in Poitiers, France, April 2-5, 2002, pp. 86-89.
[15] MENDEL, J. M.: *Fuzzy Logic Systems for Engineering: A Tutorial.* Proceedings of the IEEE, Vol. 83, No. 3, March 1995, pp. 345-378.
[16] MICHAELI, L..: *Microcontrollers for Intelligent Signal Conditioning,* Proceedings of IMEKO TC-13 Conference "Measurement in the Medicine" in Stara Lesna, Slovakia, September 7-8, 1995, pp. 73-77.
[17] MICHAELI, L.: *Modelovanie analógovo číslicových rozhraní.* Mercury-Smékal, Košice, 2001.
[18] MOUCHA, V., MARCHEVSKÝ, S., LUKÁČ, R., STUPÁK, Cs.: *Číslicová filtrácia obrazových signálov.* Edičné stredisko Vojenskej leteckej akadémie gen. M. R. Štefánika v Košiciach, Košice 2000.
[19] OCHODNICKÝ, J., TKÁČ, J.: *Neural Kalman Filter in Radar Target Tracking.* In: Proceedings of 6th International Workshop IWSSIP 99, Bratislava, June 2-4, 1999, pp. 131-134
[20] OCHODNICKÝ, J., TKÁČ, J., ŠPIRKO, Š.: *Radar Target Tracking by Neural Kalman Filter.* In: IWSSIP 2001 Proceedings, 8th International Workshop on Systems, Signals and Image Processing, June 7-9, 2001, Bucharest, Romania, pp. 113-116
[21] PITAS, I., TSAKALIDES, P.: *Multivariate Ordering in Color Image Filtering.* IEEE Transactions on Circuits and Systems for Videotechnology, Vol. 1, No. 3, September 1991, pp. 247-259.
[22] PITAS, I. - VENETSANOPOULOS, A.N.: *Order Statistics in Digital Image Processing.* Proceedings of the IEEE, Vol. 80, No. 12, December 1992, pp. 1892-1919.
[23] PRASAD, M. K., LEE, Y. H.: *Stack Filters and Selection Probabilities,* IEEE Trans. on Signal Processing, 1994, 42(10), 1994, 2628-2643.
[24] SHINDE, M. - GUPTA, S.: A *Model of hf Impulsive Atmospheric Noise.* IEEE Trans. Electromag. Compat., Vol. EMC-16, May 1974, pp. 71-75.
[25] STUPÁK, C.: *Optimalizácia kompozičných filtrov a fuzzy filtrov na báze genetických algoritmov.* Doktorandská dizertačná práca. Košice 2000.
[26] TANG, K., ASTOLA, J., NEUVO, Y.: *Nonlinear Multivariate Image Filtering Techniques.* IEEE Transactions on Image Processing, Vol. 4, No. 6, June 1995, pp. 788-799.
[27] VIERO, T., OISTAMO, K., NEUVO, Y.: *Three-Dimensional Median Related Filters for Color Image Sequence Filtering.* IEEE Trans. on CAS for Video Technology, Vol. 4, No. 2, 1994, pp. 129-142
[28] WIDROW, B. - JOHNSON, C. R.: *Stationary and Nonstationary Learning Characteristic of the LMS Adaptive Filter.* Proc. IEEE, Vol. 64, August 1976, pp. 1151.
[29] WIENER, N.: *Extrapolation, Interpolation and Smoothing of Stationary Time Series.* MIT Press Cambridge, Mass, 1949.
[30] WOODS, J. W., RADEWAN, C. H.: *Kalman Filtering in Two Dimensions,* IEEE Trans. on Information Theory, Vol. IT-23, July 1977, pp. 473-482.
[31] WOODS, J. W., DRAVIDA, S., MEDIAVILLA, R.: *Image Estimation Using Doubly Stochastic Gaussian Random Field Models.* IEEE Trans. on Pattern Analysis and Machine Intelligence, Vol. PAMI-9, No. 2, March 1987, pp. 245-253.
[32] YU, P. T., LIAO, W. H.: *Weighed Order Statistics Filters - their classification, some properties, and conversion algorithm',* IEEE Trans. on Signal Processing, Vol. 42, No. 10, 1994, pp. 2678-2691.

Recenzia knižnej publikácie Transformácia železníc vo svete

Autor: Ondrej Buček a kol. (Anna Tomová, Viera Bartošová, Alžbeta Bieliková, Danka Harmanová, Darina Chlebíková).

Vydala Žilinská univerzita v Žiline v edičnom rade ODBORNÉ KNIŽNÉ PUBLIKÁCIE, Vytlačilo EDIS – vydavateľstvo ŽU v marci 2002 ako svoju 1410. publikáciu, ISBN 80-7100-946-6.

Recenzovaná kniha poskytuje prehľad a skúsenosti z riešenia transformácie železníc v rôznych krajinách sveta. Na základe vykonanej analýzy sú stanovené zásady pre reštrukturalizáciu a transformáciu železníc.

Kniha obsahuje úvod, tri kapitoly, záver a zoznam prameňov a použitej literatúry. Jednotlivé kapitoly sa zaoberajú nasledovnými problematikami.

Kap. 1.

Súčasné problémy privatizácie železníc

Táto kapitola je zameraná na privatizáciu ako nástroj riešenia krízy sieťových systémov, koncepčné problémy privatizácie a problémy transformácie železníc.

Kap. 2.

Analýza transformácie a privatizácie železníc vo svete

Analýza foriem transformácie v Európe je rozdelená na skúsenosti z reštrukturalizácie a transformácie francúzskych železníc, Britských železníc, Švédskych železníc, Holandských železníc, belgických železníc, Poľských štátnych železníc, dánskych železníc, Nórskych štátnych železníc a železníc v Nemecku.

Ďalej obsahuje skúsenosti z reštrukturalizácie a transformácie Japonských národných železníc, Mexických železníc, železníc v Kanade, železníc Nového Zélandu a železníc v Ázii.

Kap. 3.

Základné zásady pre reštrukturalizáciu a transformáciu zovšeobecnené zo skúseností vo svete

Syntézou poznatkov zo sveta dospeli autori k nasledovným zásadám pre transformáciu a reštrukturalizáciu železníc, ktoré musia riešiť nasledovné problémy:

- *oddelenie prevádzkovej činnosti železníc od infraštruktúry,*
- *otvorenie prístupu na železničnú dopravnú cestu pre iných dopravcov,*
- *reorganizácia štruktúry riadenia,*
- *rozvoj výskumnej a vývojovej činnosti,*
- *využitie železničnej dopravy v kombinovanej doprave,*
- *privatizácia ako jeden z krokov realizácie cieľov reštrukturalizácie a transformácie.*

Túto publikáciu odporúčame nielen poslucháčom Žilinskej univerzity, ale i záujemcom zo stredných odborných škôl a učilíšť a širokej železničiarskej odbornej verejnosti.

Prof. Ing. Karel Voleský, PhD.

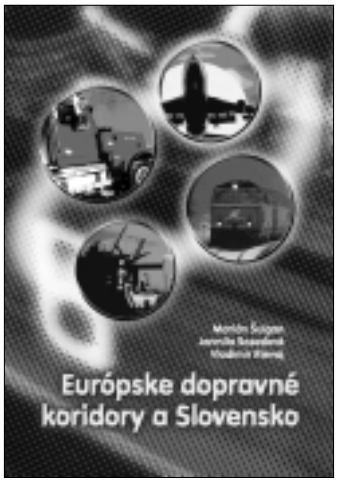

Európske dopravné koridory a Slovensko

Publikáciu autorov Mariána Šulgana, Jarmily Sosedovej a Vladimíra Rievaja (161 strán) vydala Žilinská univerzita r. 2001, ISBN 80-7100-903-2.

Monografia je určená predovšetkým študentom ŽU, no iste vzbudí pozornosť aj odborníkov z praxe. Kladie si za cieľ zhrnúť informácie o európskych dopravných koridoroch a úlohe Slovenska v ich budovaní a prevádzkovaní. Dôraz kladie na aktuálne možnosti uplatňovania multimodality v doprave na našom území v kontexte celoeurópskeho vývoja.

Publikácia má 8 kapitol.

Prvá kapitola (Multimodálne dopravné plánovanie) predstavuje čitateľovi teoretickú bázu problematiky. Obsahuje definície základných pojmov, zaoberá sa všeobecnými problémami dopravného plánovania a projektovania, ako aj jednotlivými fázami plánovacieho procesu.

Druhá kapitola sa venuje európskym dopravným koridorom, s dôrazom na projekt TINA. Táto časť publikácie obsahuje prehľadný zoznam všetkých koridorov projektu, usporiadaný podľa jednotlivých štátov.

Kapitoly 3-6 sa postupne zaoberajú cestnou, železničnou, vodnou a leteckou dopravou na území SR s dôrazom na infraštruktúru. Mapujú súčasný stav, plány a možnosti ďalšieho rozvoja jednotlivých koridorov s ohľadom na medzinárodnú aj vnútroštátnu prepravu. Pri železničnej doprave je osobitná pozornosť venovaná vysokorýchlostným tratiam.

Siedma kapitola sa podrobne venuje problematike kombinovanej dopravy. Popisuje jednotlivé vo svete používané systémy a technické riešenia s dôrazom na možnosti ich využitia v SR. Je doplnená názornými schémami a obrázkami, čo umožňuje aj laickému čitateľovi získať základnú predstavu o uvedenej problematike. Autori tiež poukazujú na problémy a obmedzenia kombinovanej dopravy, čo umožňuje reálne zhodnotiť úlohu a využitie tohto perspektívneho systému v blízkej budúcnosti.

8. kapitolou je záver.

Publikácia podáva komplexný pohľad na problematiku multimodálnej dopravy a dopravných koridorov, s dôrazom na súčasný stav a ďalší rozvoj v SR. Pozitívom práce je aj jej aktuálnosť. Okrem toho, vďaka jednoduchému štýlu a prehľadnému členeniu jednotlivých tematických okruhov, dovoľuje rýchlo získať požadované informácie aj ľuďom mimo akademickej obce a pracovníkom zaoberajúcim sa súvisiacou problematikou.

Prof. Ing. Pavel Surovec, CSc.

Názov doktorandskej dizertačnej práce: **Metalurgická štúdia zliatiny AlSi7Mg0,3**
Autor: **Ing. Dana BOLIBRUCHOVÁ**
Vedný odbor: **23-07-9 Strojárske technológie a materiály**
Školiace pracovisko: **Strojnícka fakulta Žilinskej univerzity**
Školiteľ: **prof. Ing. Lubomír Bechný,CSc.**

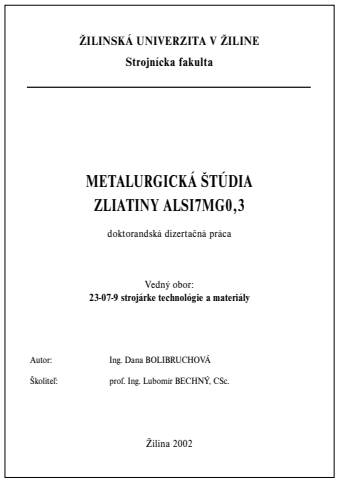
ŽILINSKÁ UNIVERZITA V ŽILINE
Strojnícka fakulta

METALURGICKÁ ŠTÚDIA
ZLIATINY ALSI7MG0,3

doktorandská dizertačná práca

Vedný obor:
23-07-9 strojárke technológie a materiály

Autor: Ing. Dana BOLIBRUCHOVÁ
Školiteľ: prof. Ing. Lubomír BECHNÝ, CSc.

Žilina 2002

Resumé:

Doktorandská dizertačná práca sa zaoberá metalurgickou štúdiou zliatiny AlSi7Mg0,3 z hľadiska ovplyvnenia kryštalizácie očkovaním, modifikovaním a legovaním. Bol zisťovaný vplyv troch typov materiálov formy na výsledný efekt očkovania, modifikovania a legovania v nadväznosti na materiálové charakteristiky skúmanej zliatiny.

Ďalšia časť dizertácie bola venovaná analýze vplyvu filtrácie a dvoch druhov keramických filtrov (penový a lisovaný) na mechanické vlastnosti a pórovitosť zliatiny AlSI7Mg0,3.

Posledná časť experimentálnej práce sa venuje skráteniu štandardného režimu tepelného spracovania zliatiny AlSi7Mg0,3 a získané výsledky sú aplikované na odliatok hlavy valcov.

Názov doktorandskej dizertačnej práce: **Tvorba siete a liniek leteckých dopravcov v Slovenskej republike**
Autor: **Ing. Peter Hanák**
Vedný odbor: **37-01-9 Dopravná a spojová technológia**
Školiace pracovisko: **Žilinská univerzita, Fakulta prevádzky a ekonomiky dopravy a spojov**
Školiteľ: **prof. Ing. Bohuslav SEDLÁČEK, CSc.**

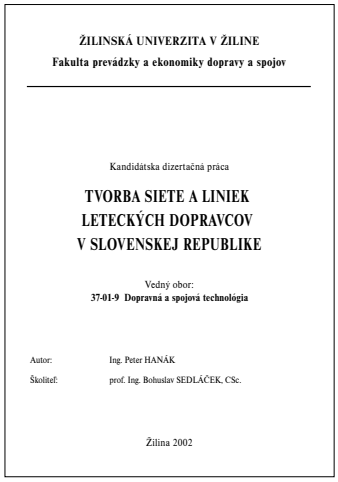
ŽILINSKÁ UNIVERZITA V ŽILINE
Fakulta prevádzky a ekonomiky dopravy a spojov

Kandidátska dizertačná práca

TVORBA SIETE A LINIEK
LETECKÝCH DOPRAVCOV
V SLOVENSKEJ REPUBLIKE

Vedný obor:
37-01-9 Dopravná a spojová technológia

Autor: Ing. Peter HANÁK
Školiteľ: prof. Ing. Bohuslav SEDLÁČEK, CSc.

Žilina 2002

Resumé:

Zmena trhového prostredia po roku 1989 priniesla mnohé problémy, na ktoré slovenskí dopravcovia neboli zvyknutí a pripravení. Za obdobie dvanástich rokov bolo na slovenskom trhu veľké množstvo leteckých dopravcov, ktorí pre nedostatok poznatkov pri tvorbe liniek a výberu vhodného typu letúna museli svoju činnosť ukončiť. Dizertačná práca Tvorba siete a liniek leteckých dopravcov v Slovenskej republike sa preto zaoberá komplexným riešením tejto problematiky. Teoretická časť práce popisuje spôsob vytvorenia projektu na zavedenie novej destinácie (linky) do prevádzky leteckého dopravcu. Pre jeho úspešné vytvorenie je potrebné zaoberať sa:

- *zberom informácií a ich vyhodnotením,*
- *výberom lietadlovej techniky pozostávajúci z nasledovných analýz:*
- *analýza letúna,*
- *analýza plánovania,*
- *ekonomická analýza,*
- *finančná analýza,*
- *kalkuláciou hospodárskeho výsledku,*
- *vytvorením samotného odporúčania vedeniu dopravcu.*

Po vytvorení projektu prichádza na rad plnenie činností samotnej realizácie novej linky do prevádzky. Činnosti sú navrhnuté a popísané v harmonograme plnenia úloh pri zavádzaní novej destinácie. Harmonogram je časovo optimalizovaný a jednotlivé okruhy činností sú:

- *koncepcia, letový poriadok,*
- *zmluvné zabezpečenie,*
- *distribúcia,*
- *cenotvorba,*
- *prevádzkovo-technické zabezpečenie,*
- *marketingové zabezpečenie.*

POKYNY PRE AUTOROV PRÍSPEVKOV DO ČASOPISU KOMUNIKÁCIE - vedecké listy Žilinskej univerzity

1. Redakcia prijíma iba príspevky doteraz nepublikované alebo inde nezaslané na uverejnenie.
2. Rukopis musí byť v jazyku slovenskom a anglickom (týka sa autorov zo Slovenska). Príspevok by nemal prekročiť 7 strán v každej jazykovej mutácii (formát A4, písmo Times Roman 12 bodové). K článku dodá autor **resumé** v rozsahu maximálne 10 riadkov v slovenskom a anglickom jazyku).
3. Príspevok prosíme poslať: **e-mailom**, ako prílohu spracovanú vo Worde, na adresu *holesa@nic.utc.sk* alebo *polednak@fsi.utc.sk* príp. *vrablova@nic.utc.sk* **alebo doručiť na diskete 3,5** vo Worde a **jeden výtlačok** článku na adresu Žilinská univerzita, OVaV, Moyzesova 20, 010 26 Žilina.
4. Skratky, ktoré nie sú bežné, je nutné pri ich prvom použití rozpísať v plnom znení.
5. Obrázky, grafy a schémy, pokiaľ nie sú spracované v Microsoft WORD, je potrebné doručiť buď v digitálnej forme (ako GIF, JPG, CDR, BMP súbory), prípadne nakresliť kontrastne na bielom papieri a predložiť v jednom exemplári. Pri požiadavke na uverejnenie fotografie priložiť ako podklad kontrastnú fotografiu alebo diapozitív. **Pre obidve mutácie** spracovať **jeden obrázok** s popisom v slovenskom a anglickom, **resp. len v anglickom jazyku** (text pod obrázkom v oboch mutáciách).
6. Odvolania na literatúru sa označujú v texte alebo v poznámkach pod čiarou príslušným poradovým číslom v hranatej zátvorke. **Zoznam použitej literatúry** je uvedený za príspevkom. Citovanie literatúry musí byť **podľa záväznej STN 01 0197 (ISO 690)** „Bibliografické odkazy".
7. K rukopisu treba pripojiť **plné meno a priezvisko autora a adresu inštitúcie v ktorej pracuje, e-mail adresu** a číslo telefónu alebo faxu.
8. Príspevok posúdi redakčná rada na svojom najbližšom zasadnutí a v prípade jeho zaradenia do niektorého z budúcich čísiel podrobí rukopis recenziám a jazykovej korektúre. Posledný obťah pred tlačou bude poslaný autorovi na definitívnu kontrolu.
9. Termíny na dodanie príspevkov do čísiel v roku sú: 28. február, 31. máj, 31. august a 30. november.
10. V ďalšom čísle bude téma: Riešenie krízových situácií.

COMMUNICATIONS - Scientific Letters of the University of Žilina Writer's Guidelines

1. Submissions for publication must be unpublished and not be a multiple submission.
2. Manuscripts written in English language must include abstract also written in English. The submission should not exceed 7 pages (format A4, Times Roman size 12). The abstract should not exceed 10 lines.
3. Submissions should be sent: **by e-mail** (as attachment in system Microsoft WORD) to one of the following addresses: *holesa@nic.utc.sk* or *vrablova@nic.utc.sk* or *polednak@fsi.utc.sk* **with a hard copy** (to be assessed by the editorial board) or **on a 3.5" diskette** in (Microsoft WORD) **with a hard copy** to the following address: Zilinska univerzita, OVaV, Moyzesova 20, SK-10 26 Zilina, Slovakia.
4. Abbreviations, which are not common, must be used in full when mentioned for the first time.
5. Figures, graphs and diagrams, if not processed by Microsoft WORD, must be sent in electronic form (as GIF, JPG, CDR, BMP files) or drawn in contrast on white paper, one copy enclosed. Photographs for publication must be either contrastive or on a slide.
6. References are to be marked either in the text or as footnotes numbered respectively. Numbers must be in square brackets. The list of references should follow the paper (according to **ISO 690**).
7. The author's exact mailing address, **full names, e-mail address, telephone or fax number, and the address of the organisation where the author works** and contact information must be enclosed.
8. The editorial board will assess the submission in its following session. In the case that the article will be accepted for future volumes, the board submits the manuscript to the editors for review and language correction. After reviewing and incorporating the editor's remarks, the final draft (before printing) will be sent to authors for final review and adjustment.
9. The deadlines for submissions are as follows: February 28, May 31, August 31 and November 30.
10. Next issue will be dedicated to the following topic: Crises Situation Solution.

kamUNIkácie
COMMUNICATIONS

VEDECKÉ LISTY ŽILINSKEJ UNIVERZITY
SCIENTIFIC LETTERS OF THE UNIVERSITY OF ŽILINA

Adresa redakcie:
Address of the editorial office:
Žilinská univerzita
Oddelenie pre vedu a výskum
Office for Science and Research
Moyzesova 20, Slovakia
SK 010 26 Žilina
Tel.: +421/41/5620 392
Fax: +421/41/7247 702
E-mail: polednak@fsi.utc.sk, holesa@nic.utc.sk

Každý článok bol oponovaný dvoma oponentmi.
Each paper was reviewed by two reviewers.

Časopis je excerpovaný v Compendexe
Journal is excerpted in Compendex

Vydáva Žilinská univerzita
v EDIS - vydavateľstve ŽU
J. M. Hurbana 15, 010 26 Žilina
pod registračným číslom 1989/98
ISSN 1335-4205

It is published by the University of Žilina in
EDIS - Publishing Institution of Žilina University
Registered No: 1989/98
ISSN 1335-4205

Objednávky na predplatné prijíma redakcia
Vychádza štvrťročne
Ročné predplatné na rok 2002 je 500,- Sk

Order forms should be returned to the editorial office
Published quarterly
The subscription rate for year 2002 is 500 SKK.

http://www.utc.sk/komunikacie